CARBON-DOPED TiO_2: SYNTHESIS, CHARACTERIZATION AND VISIBLE LIGHT PHOTOCATALYTIC ACTIVITIES FOR ENVIRONMENTAL REMEDIATION

ZHANG LI

SCHOOL OF ELECTRICAL & ELECTRONIC ENGINEERING

A thesis submitted to the Nanyang Technological University
in fulfillment of the requirement for the degree of
Doctor of Philosophy

2013

Acknowledgements

First and foremost, I would like to extend my deepest gratitude to my supervisor, Professor Tan Ooi Kiang, for introducing me into the interesting field of photocatalysis ever since my Year 2 undergraduate studies. His passion and vision for research have helped me to appreciate the rigors of scientific research and inspired me to pursue my graduate studies. He has given me a very rewarding and lasting experience throughout the entire course of my thesis work. I truly appreciate his guidance and continuous encouragement as well as the liberty he gave me to explore my own research interests, which has helped to cultivate my problem solving skills and boost my confidence and ability in performing independent research work.

Secondly, I would like to express my sincere appreciation to my co-supervisor, Associate Professor Tse Man Siu, who was more than willing to guide me in the experimental system design and setup and impart his broad knowledge and invaluable experiences to me. The countless discussions have been both stimulating and enlightening, and inspired me to strive further for continuous improvement in my thesis work.

Many thanks also go to Dr Chen Xiaofeng and Dr Fang Xiaoqin for their useful suggestions and helps in experimental setup and results analysis at different stages of this work.

My appreciations go to my fellow teammates, also my good friends, Ms Tan Pei Yun, Mr Chow Chee Lap, Mr Lim Chiew Keat, Mr Chua Chin Sheng, Ms Han Mandi, Ms Leiw Ming Yian, and Ms Luo Qiong, who have always supported me and shared their knowledge, experience, and happiness all these years.

I would like to also acknowledge the lab technicians in Sensors and Actuators Lab, Characterization Lab, Photonic Lab I & II, Nanoelectronics Lab I, Nanyang NanoFabrication Centre Clean Room 1 and Clean Room 2 for their help in equipment training and maintenance of the equipment in good working conditions. Special appreciations go to Assistant Professor Sze Chun Chau from School of Biological Sciences for sharing her laboratory to carry out bactericidal tests.

Lastly, I wish to express my deepest gratefulness to my husband, Mr Sun Zhuochao, my parents and parents-in-law, for their endless love, understanding and moral support throughout all these years, without which I would not have accomplished my thesis.

Table of Contents

List of Figures

List of Tables

Summary

Since the discovery of photocatalytic water splitting on TiO_2 electrodes in 1972, titanium dioxide (TiO_2) has been studied extensively as a promising photocatalyst in air and water purification for environmental remediation. Despite its various advantages such as high reactivity, chemical stability, robustness against photocorrosion, low toxicity and low cost, two major drawbacks have hindered its usage in practical applications: the requirement for UV light excitation due to the large bandgap of TiO_2 has limited its effective use of solar energy or indoor light; the recombination of photogenerated electron and hole pairs has reduced the overall quantum efficiency of TiO_2 significantly. Therefore, it is desirable to improve the photocatalytic efficiency of TiO_2 by extending its activities into visible light range and enhancing the charge carrier separation for more useful applications.

The first part of this thesis has been devoted to the development of a simple and cost-effective process for mass-production of visible light-active carbon-doped titanium dioxide (C-TiO_2) photocatalyst. C-TiO_2 nanoparticles with mixed anatase/rutile phases were successfully synthesized by conventional mild oxidation of TiC precursor at 350 ºC for 2-50 hours and more aggressive oxidation at higher temperature of 400-600 ºC for 2 hours in air. With prolonged oxidation time or increase in oxidation temperature, initial decrease in crystallite size was unveiled due to cracking of TiC grains, renucleation of TiO_2 and diffusion of carbon atoms. The doped carbon in the TiO_2 matrix was found to exist as graphite-like carbon, interstitial carbon in the form of carbonate species and substitutional carbon in the

oxygen sites. The former two carbon states serve as photosensitizers while the substitutional carbon introduces additional electronic states just above the valence band of TiO_2, that collectively contribute to the visible light photocatalytic activities. The band structure and three possible pathways were thus proposed for enhanced photocatalytic oxidation processes in C-TiO_2 nanoparticles.

The potential of utilizing the synthesized C-TiO_2 nanoparticles for photocatalytic environmental remediation was demonstrated by the removal of volatile organic compound (VOC) and disinfection of microorganisms. The C-TiO_2 nanoparticles in coated form were first evaluated for the destruction of gaseous toluene as a probe VOC in the custom-built test system under both static and dynamic flow conditions with tunable light sources/intensity, feed pollutant concentration, humidity level, balancing gas and flow rates. The photocatalytic disinfection of Gram-negative *Escherichia coli* (*E. coli*) and Gram-positive *Enterococcus faecalis* (*E. faecalis*) with different cell wall structures in aqueous suspension were then investigated under different light irradiation conditions. It was found that C-TiO_2 synthesized at higher oxidation temperature with shorter duration of 2 hours demonstrated better photocatalytic performance than those prepared by the conventional time-consuming mild oxidation process. The performance was comparable to the commercially available C-TiO_2 Kronos vlp 7000 and superior to N-TiO_2 produced by a similar recipe. Thus, the synthesis process for visible light-active C-TiO_2 can be drastically simplified with a much shortened processing time, suitable for large-scale production.

Further improvement of the synthesized C-TiO_2 was achieved by co-modification with novel metals to enhance the charge carrier separation in the second part of this

thesis. Pt/C-TiO_2 and Ag/C-TiO_2 were successfully prepared by a novel synthesis approach through thermal oxidation of $H_2PtCl_6 \cdot 6H_2O$ or $AgNO_3$-impregnated TiC precursor at 500 ºC for 2 hours in air for simultaneous TiO_2 formation, C doping and Pt/Ag modification, all in a single step. The synthesized nanoparticles consisted of 70% anatase and 30% rutile, resembling the phase structure of P25 TiO_2 with high photoactivities. With increasing Pt or Ag content, the anatase/rutile grain growth was retarded. The loaded Pt or Ag nanoparticles in their metallic states further enhanced the visible light absorption and charge carrier separation by serving as electron scavengers. The visible light photocatalytic oxidation mechanism with four pathways was proposed and the enhanced photocatalytic performance in comparison to C-TiO_2 was successfully demonstrated with the destruction of gaseous toluene in air and decomposition of Rhodamine B in aqueous suspension. These could be attributed to the synergistic effect of C doping and Pt/Ag modification, increasing its potential of being utilized in both air and water purification with higher photocatalytic efficiency.

CHAPTER 1 : INTRODUCTION

1.1 Motivation

Energy issue and environmental issue are widely recognized as two major challenges mankind will have to face and solve for the sustainable development in 21st century. Since the discovery of photo-induced decomposition of water on TiO_2 electrodes by Fujishima and Honda in 1970s [1], photocatalytic technology centered on the chemical conversion and storage of the abundant, clean and safe solar energy appears promising to tackle these challenges: 1. Hydrogen generation based on photoelectrochemical splitting of water can help to meet the human energy demands as the fossil fuels are gradually exhausted and at the same time ease the crisis brought by "greenhouse effect" due to combustion of fossil fuels [2]; 2. Photocatalytic degradation of toxic organic pollutants from air, soil and water and the associated self-cleaning technology can help to provide a green living environment.

Consequently, enormous efforts have been devoted to the research of photocatalysis in different areas including removal of organic and inorganic pollutants, dye sensitized solar cells, hydrogen production, organic synthesis and disinfection of pathogenic organisms [3]. Some of the products including self-cleaning surfaces and air purifiers have already been commercialized. According to BCC research

(formerly known as Business Communications Company), "the total global market for photocatalyst products is forecast to grow at a compound annual growth rate (CAGR) of 14.3% during the next 5 years, increasing from $848 million in 2009 to nearly $1.7 billion in total revenues by 2014" [4].

Table 1-1. Comparison of common techniques for environmental remediation in different application fields [3, 5-8]

Application field	Techniques	Pros	Cons
Air cleaning	Filtering	– Highly efficient in removing particles down to 0.01μm	– High energy costs for high efficiency filters – Frequent maintenance and replacement
	Ionizing	– Effective on small particles	– Ineffective on gases, odors, large particles – Particle re-suspension upon atmospheric condition change
	Adsorption	– Effective in removing gaseous pollutants and odors	– Ineffective on large particles – Pollutants can be regenerated when aggravated or disturbed
	Ozonation	– Effective for a broad range of contaminants	– Harmful to human beings – Only safely used in unoccupied rooms
	Cyclone	– Effective for removing large particles>15μm	– Large space requirement
	Scrubbing	– Effective for removing small particles and VOC	– High power consumption – High maintenance costs due to corrosion and abrasion
Water purification	Activated sludge process	– Effective biological wastewater treatment	– Slow reaction rates – Inefficiency at low pollutant level (sub-ppm) – Disposal of sludge – Control of pH and temperature – Bacteria endangered by toxic substances
	Adsorption	– Effective extraction of organic materials	– Expensive regeneration – Fast decrease of the capacity to accumulate toxic organics due to non-selective absorption

	Air stripping	– Effective for removal of volatile organic contaminants	– Convert water pollutants into air pollutants
	Chemical oxidation	– Efficient at high pollutant concentration	– Unable to mineralize all organic substances – Not cost effective for removal of pollutants at low concentrations – Secondary pollution possible
	UV/O_3,UV/H_2O_2, photo-Fenton	– Better adaptation to specific treatment requirements by various combinations	– High cost – Only applicable to small COD contents (≤5.0 g/l)
Microorganism disinfection	Chlorination	– Low cost – No energy required to operate – Easy maintenance	– Periodic chemical addition required – System malfunction caused by solid jam – Elevated pH reduces germicidal effect
	Ozonation	– Most potent disinfect, especially for resistant organisms	– High operation and maintenance cost – Harmful to human beings
	UV irradiation	– Easy installation, operation and maintenance	– Low turbidity, low concentrations of iron, calcium or phenols and high dosage of protozoa required for water disinfection – Harmful to human beings

Some conventional techniques for environmental remediation in air/water purification/disinfection have been listed in Table 1-1 with their pros and cons summarized [3, 5-8]. In general, most of these techniques are only efficient for removal of specific types of pollutants and require frequent maintenance and replacement which incurs high cost. Only ozonation appears versatile for a wide range of pollutants in different applications. Yet, the commercial ozone generators produce over 3000 mg/h ozone for shock treatment, which is very harmful to human being. It is advisable to be used only in unoccupied space. As compared to these techniques, the appeal of photocatalysis for environmental remediation lies in the

prospect of selective redox transformations and decomposition of a broad range of pollutants by utilization of the free and abundant solar energy or even poor indoor lighting at near ambient temperature [3]. For a complete reaction with organic pollutants, the harmful pollutants will be mineralized into innocuous final products such as CO_2 and H_2O.

A promising photocatalyst suitable for sensitizing the photo-mineralization of a wide range of organic pollutants should be (a) photoactive, (b) biologically and chemically inert, (c) photo-stable and (d) cheap [7]. The commonly used photocatalysts are primarily metal oxides or sulfides, i.e. TiO_2, ZnO, ZrO_2, SnO_2, WO_3, CeO_2, Fe_2O_3, and CdS [8]. Among all, TiO_2 has been most extensively studied and become almost a synonym for the word "photocatalyst" due to its superior performance in all the above mentioned aspects.

Despite its various advantages, two major drawbacks have hindered the usage of pristine TiO_2 in practical applications: the requirement for UV light excitation due to the large bandgap of TiO_2 has limited its effective use of solar energy or indoor light with abundant visible light portion; the recombination of photogenerated electron and hole pairs has reduced the overall quantum efficiency of TiO_2 significantly. Therefore, in order to establish an economical, clean and safe reaction system, it is desirable to harness the visible light portion with high efficiency for more useful photocatalytic applications.

To address the first drawback, second generation visible light-active TiO_2 was studied by surface modification of TiO_2 via organic materials [9-13] or semiconductor [14-17] coupling, bandgap modification by creation of oxygen

vacancies [18, 19], and doping of transition metals [20-23] or non-metals [19, 24-27], with the last two being the most extensively studied. As metal doping often suffers from thermal instability or is more prone to serve as recombination centers due to the dopants' localized d-states deep in the band gap of TiO_2 [17], non-metal doping has received a lot of attention ever since the report of N-TiO_2 as a visible light active photocatalyst by Asahi in 2001 [13]. In particular, carbon was suggested to be the most promising among the three anion dopants including nitrogen, sulfur, and carbon due to a significant overlap between the O 2p state and the C 2p state and thus the production of the largest red shift of the valence band edge [28].

Besides the modification of TiO_2, small bandgap photocatalysts including $ZnIn_2S_4$ [29], WO_3 [30], CdS [31], Fe_2O_3 [32], $BiVO_4$ [33] were also reported with visible light photoresponses. However, these photocatalysts either used rare metals (e.g. In, Cd and Bi) to increase the cost significantly, or had stability issues (e.g. prone to photocorrosion), or may be hazardous to the environment (e.g. Cd^{+2}) [2], limiting their practical usage in environmental remediation. Thus, TiO_2-based photocatalyst remained as the leading candidate in the field of photocatalysis.

To address the second drawback, strategies such as morphological modifications using highly dispersed TiO_2 and TiO_2 nanotubes or chemical modifications involving incorporation of additional components in the TiO_2 structure have been adopted to enhance the charge carriers separation so as to improve the overall quantum efficiency of TiO_2 [34]. In particular, loading noble metals into TiO_2 matrix can form a Schottky barrier with the TiO_2 to conduct away the photogenerated electrons irreversibly [35, 36], achieving spatial charge separation.

In this thesis, a simple and cost-effective process was developed for synthesis of efficient visible light-active carbon-doped titanium dioxide (C-TiO_2) photocatalyst, specifically, by conventional mild oxidation of precursor titanium carbide (TiC) at 350 ºC for 2 to 50 hours or more aggressive oxidation at higher temperature of 400 to 600 ºC for 2 hours in air. Potentially, this facile fabrication process can be applied to the mass-production of C-TiO_2 with better utilization of solar energy and poor indoor lighting for more practical photocatalytic usage. After the optimization of oxidation temperature and time for this process, co-doping of carbon with novel metals including platinum and silver was studied for enhanced charge carrier separation to further improve the photocatalytic efficiency of C-TiO_2 in the later part of the thesis.

1.2 Objective

The main objective of this project is to develop a simple and cost-effective process for mass-production of highly efficient visible light-active carbon-doped titanium dioxide (C-TiO_2) photocatalyst with enhanced charge carrier separation for environmental remediation.

The detailed scope of work to achieve this objective can be categorized into the following areas:

1. Facile fabrication of visible light-active C-TiO_2 photocatalyst;
2. Characterization of the physicochemical properties of the synthesized C-TiO_2;
3. Evaluation of the synthesized C-TiO_2 for photocatalytic environmental remediation under visible light irradiation;

4. Further improvement of the photocatalytic performance of C-TiO_2 by co-doping with noble metals for enhanced charge carrier separation.

1.3 Major Contributions of the Thesis

Under the scope of work mentioned in the last section, the major contributions of this thesis can be summarized as follows:

1. The C-TiO_2 nanoparticles were obtained through a single-step thermal oxidation of precursor TiC. For the first time, the formation of C-TiO_2 by oxidation of TiC with a more aggressive process at 400-600 °C for 2 hours was studied systematically in parallel with the conventional mild oxidation process at 350 °C for 2-50 hours. The aggressive oxidation process with much shortened oxidation time has demonstrated more pronounced visible light photocatalytic performance on mineralization of gaseous toluene and disinfection of microorganisms in aqueous suspension, providing a facile method suitable for large-scale production of C-TiO_2 photocatalyst. The performance of the synthesized C-TiO_2 nanoparticles was also found comparable to the commercially available C-TiO_2 Kronos vlp 7000 and superior to N-TiO_2 produced by a similar recipe.

2. For the first time, the states of carbon in the TiO_2 lattice upon thermal oxidation of TiC were explicitly elucidated in a meticulous manner via various characterization techniques. The presence of graphite-like carbon and the coexistence of substitutional and interstitial carbon in the TiO_2 lattice have collectively contributed to the enhanced absorption in visible light range as compared to pristine TiO_2. The presumed band structure of the C-TiO_2 and thus

three possible pathways for enhanced visible light photocatalytic performance were proposed accordingly.

3. A major contribution of this thesis is the design, setup and fine-tuning of the test system for evaluation of planar photocatalytic test pieces for gaseous pollutants removal. The system encompasses pollutant gas supply balanced with zero air by constant infusion and vaporization of pollutants originally in liquid form, two batch reactors and three dynamic reactors, housing for reactors with LED/fluorescent light sources, and a custom-modified gas chromatography for simultaneous analysis of gaseous pollutants and CO_2/CO byproducts. The system allows for systematic evaluation of photocatalytic coating under both static and dynamic flow conditions with tunable light sources/intensity, feed pollutant concentration, humidity level, balancing gas and flow rates and it can be generalized to the evaluation on a broad range of volatile organic compounds and gaseous pollutants.

4. To further improve the photocatalytic performance of C-TiO_2 with enhanced charge carrier separation, a facile fabrication approach was introduced to synthesize Pt/C-TiO_2 and Ag/C-TiO_2 by thermal oxidation of $H_2PtCl_6 \cdot 6H_2O$ or $AgNO_3$-impregnated TiC precursor. Simultaneous TiO_2 formation, C doping and Pt/Ag modification were achieved in one single step, which was reported for the first time [37]. With various physicochemical characterizations, the states of C and Pt/Ag in the TiO_2 lattice were elucidated, and the band structure and tentative visible light photocatalytic mechanism with four pathways were proposed for the first time. The enhancement of visible light phototocatalytic performance in

comparison to C-TiO_2 was demonstrated by the degradation of gaseous toluene in batch reactors and decomposition of Rhodamine B in aqueous suspension.

1.4 Organization of the Thesis

Chapter 1 presents the background and motivation for the current research work, objective with scope of work, major contributions and the organization of this thesis.

Chapter 2 contains the literature review of topics related to this research project. From the fundamentals and principles of photocatalysis, TiO_2-based photocatalyst as the most researched photocatalyst is reviewed, including its limitations and various ways to improve its visible light activities and charge carrier separation for more useful applications. Lastly, the application of TiO_2 photocatalysis in environmental remediation is covered, focusing on the major category of pollutants in air cleaning, water purification, and microorganism disinfection together with their reaction mechanisms or pathways.

Chapter 3 describes the synthesis of C-TiO_2 by thermal oxidation of TiC and its various characterization results, including XRD, Raman, and SEM/TEM for examination of structures and morphology; FTIR and XPS for investigation of surface bonding, chemical states and density of states above valence band edge introduced by carbon doping; and UV-Vis diffuse reflectance and photoluminescence for study of optical properties. Finally, the presumed band structure and photocatalytic mechanism of the synthesized C-TiO_2 is presented based on all the characterization results.

Chapter 4 presents the photocatalytic performance evaluation of the synthesized C-TiO_2 for volatile organic compounds (VOC) removal and microorganism disinfection. The custom-built test system for evaluating photocatalytic coating on degradation of gaseous pollutants is first described in details. The photocatalytic destruction of gaseous toluene as a probe pollutant is systematically studied in both batch reactors with fixed reaction volume and dynamic reactors with continuous flow of contaminants under different conditions. The microorganism disinfection on gram-negative *E. coli* and more robust gram-positive *E. Faecalis* is then investigated under different light irradiation conditions

Chapters 5 details the investigation on one-step facile fabrication of Pt/C-TiO_2 and Ag/C-TiO_2 to further improve the performance of C-TiO_2 by enhancing the charge carrier separation as well as the visible light absorption. Followed by the synthesis, their physicochemical properties are studied via various characterization tools. The band structure and possible visible light photocatalytic mechanism are proposed with these characterization results. The enhancement of phototocatalytic performance in comparison to C-TiO_2 is finally evaluated for the degradation of gaseous toluene in batch reactors and decomposition of Rhodamine B in aqueous suspension under visible light irradiation.

Chapter 6 concludes the thesis report and presents recommendations for the future direction of this research project.

CHAPTER 2 : LITERATURE REVIEW

2.1 Fundamentals and Principles of Photocatalysis

The discovery of photo-induced decomposition of water on TiO_2 electrodes by Fujishima and Honda in 1970s has started a new era for semiconductor-sensitized heterogeneous photocatalysis [1]. Subsequently, following the work on photodegradation of polychlorobiphenyls with TiO_2 by Carey et. al in 1976 [38] and photoreduction of cyanide and sulphite with different semiconductor materials including TiO_2, ZnO, CdS, and Fe_2O_3 by Frank and Bard in 1977 [39, 40], the application of photocatalysis has been extended to the environmental frontiers for water treatment and air purification [38-44].

According to the International Union of Pure and Applied Chemistry (IUPAC), photocatalysis is defined as "change in the rate of a chemical reaction or its initiation under action of ultraviolet, visible, or infrared radiation in the presence of a substance - the photocatalyst - that absorbs light and is involved in the chemical transformation of the reaction partners" [45]. This definition highlights the essential elements of a photocatalytic process: a light source, a photocatalyst, and the chemical transformation of the reactants.

Depending on whether the initial photoexcitation occurs on the adsorbed reactants which subsequently interact with the ground state of the catalyst substrate or on the other hand happens on the catalyst substrate which then reacts with the ground state reactants, the photocatalytic process can be categorized into "catalyzed photoreaction" and "sensitized photoreaction" respectively. In general, the heterogeneous photocatalysis commonly employed in environmental remediation refers to the semiconductor-sensitized photoreaction [46] with semiconductor as the photocatalyst.

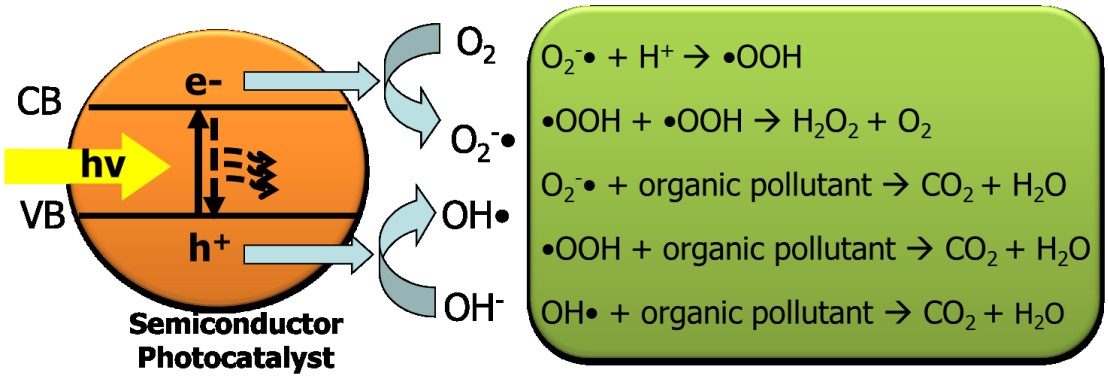

Figure 2-1. Schematic illustration of the photocatalytic process.

The photocatalytic process can be illustrated schematically as shown in Figure 2-1. Under illumination by photons of greater than bandgap energies, highly reactive electron-hole pairs can be generated in the photocatalyst. These charge carriers can be trapped at the defect sites or can recombine to dissipate the energy as light or heat. Alternatively, if they manage to migrate to the solid surface, the negative electron will react with the adsorbed oxygen molecule to form super oxide radical anion (O_2^- ·), which may further react with H^+ to produce hydroperoxyl radical (·OOH) and subsequently hydrogen peroxide (H_2O_2) [34, 47]. Similarly, the positive hole will

break apart the adsorbed water molecule (OH^-) to produce hydroxyl radicals ($OH\cdot$), which are extremely powerful oxidants. These generated reactive oxygen species (ROS) including $O_2^-\cdot$, $\cdot OOH$, H_2O_2, and $OH\cdot$ will undergo a host of electron-transfer processes with the adsorbed pollutants of suitable reduction-oxidation potentials. These processes must compete with the electron-hole recombination process which often hinders the overall quantum efficiency in order to effectively mineralize the harmful pollutants into less nocuous substances [48]. For a complete reaction with organic pollutants, CO_2 and H_2O are generated as the final products.

2.2 TiO_2-Based Photocatalyst

The commonly used photocatalysts are primarily metal oxides- or sulfides-based semiconductors in either pure or modified form, i.e. TiO_2, ZnO, ZrO_2, SnO_2, WO_3, CeO_2, Fe_2O_3, and CdS [8]. Among all, TiO_2-based photocatalyst has been most extensively studied due to its various advantages such as high reactivity, chemical stability, robustness against photocorrosion, low toxicity and low cost [7]. It has vast applications in heterogeneous photocatalysis as a photocatalyst, in solar cells for the production of hydrogen and electric energy, in paints, paper and food as a colorant, in coating as a corrosion protective material and in electronic devices as variable resistors [49].

2.2.1 Properties of Pristine TiO_2

Titanium dioxide (TiO_2) normally exists in three different polymorphs: anatase, brookite and rutile [50]. However, only anatase and rutile are widely studied for their applications in photocatalysis. Their crystal structures are illustrated as shown in Figure 2-2. Both of these two basic building blocks consist of one Ti atom (Ti^{4+}) surrounded by six O atoms (O^{2-}), forming TiO_6 octahedra [49]. In anatase, the corner-sharing octahedra forms (001) planes (Figure 2-2 (a)) while in rutile, the octahedra shares edges along 〈110〉 directions (Figure 2-2 (b)), both giving rise to tetragonal structures [49].

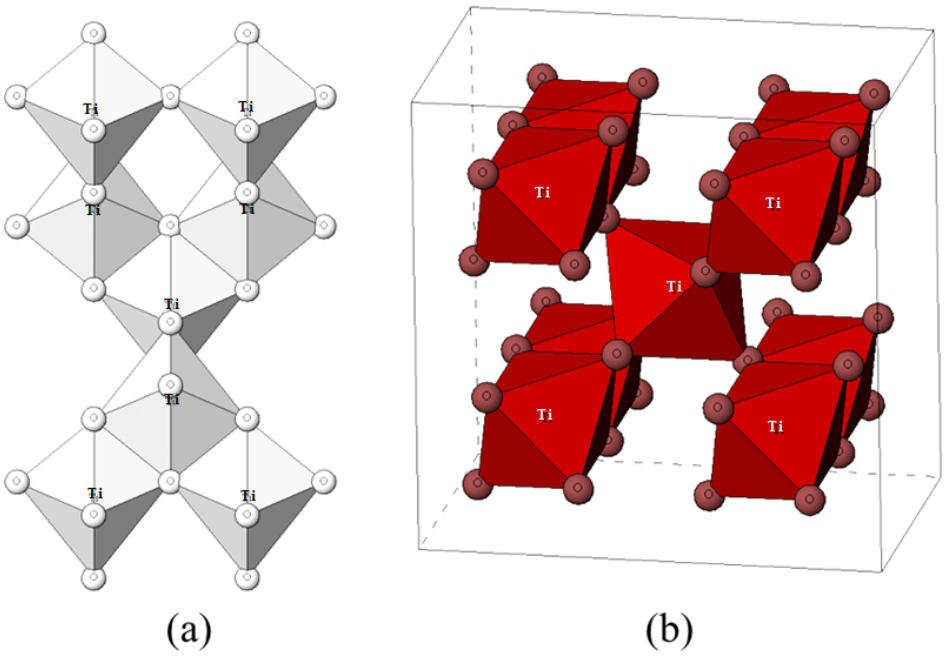

Figure 2-2. Crystalline structures of TiO_2 anatase (a) and rutile (b): reprinted with permission from Dr Katsuhiro Nomura (nomura-k@aist.go.jp; http://staff.aist.go.jp/nomura-k/english/itscgallary-e.htm).

Anatase is reported as the most photoactive phase of TiO_2 with a band gap of 3.2 eV, corresponding to an optical wavelength of 387 nm. Rutile on the other hand exhibits lower photo-catalytic activity yet is the most thermodynamically stable phase and abundant in TiO_2 in its bulk material. It has a band gap of 3.0 eV, which corresponds to an optical wavelength of 410 nm. Depending on the grain size of the TiO_2 particles, mixed phases can coexist. And phase transition can take place due to various factors. For instance, the commercially available Degussa P25 powder with 80% anatase phase and 20% rutile phase is known for its strong photocatalytic capabilities and is normally chosen as a reference for photocatalytic performance comparisons [49].

TiO_2 as the most extensively studied photocatalyst has exhibited relatively high reactivity and chemical stability in various photocatalytic degradation processes. However, there are two major drawbacks of pristine TiO_2, limiting its usage in practical applications. Firstly, the requirement for UV light excitation ($\lambda < 387$ nm for anatase TiO_2) due to the large bandgap of TiO_2 has limited its practical efficiency for solar applications and indoor applications with abundant visible light portion. Secondly, the recombination of photogenerated electron and hole pairs has reduced the overall quantum efficiency of TiO_2 significantly. Effective approaches to tackle these two challenges will be reviewed in details in Section 2.2.2 and 2.2.3, respectively.

2.2.2 Visible Light-Active TiO_2

Numerous contributions have been devoted in the late 1980s to develop second generation visible light-active TiO_2 in order to harness the abundant visible light

portion in natural light as well as the relative weak indoor light for more useful applications [51]. Some of the main research directions include surface modification of TiO_2 via organic materials [9-13] or semiconductor [14-17] coupling, bandgap modification by creation of oxygen vacancies [18, 19], and doping of transition metals [20-23] or non-metals [19, 24-27], with the last two being the most extensively studied.

2.2.2.1 Surface Modification

Various surface modification techniques such as dye sensitization [9-11], polymer sensitization [12, 52] and semiconductor coupling [14-17] have been used to induce visible light photocatalysis on TiO_2 surfaces. These techniques share the similar mechanism as shown in Figure 2-3.

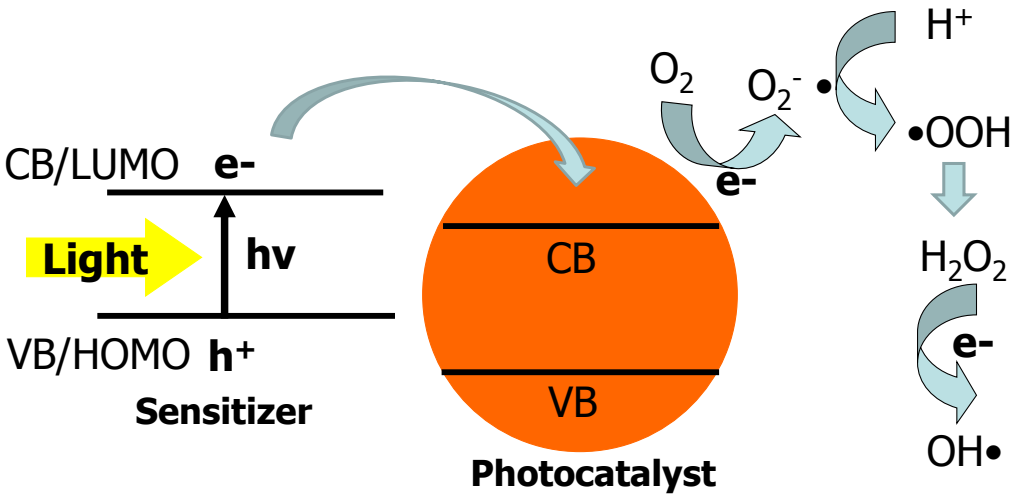

Figure 2-3. Mechanism of visible light activation of a wide bandgap semiconductor by semiconductor/organic materials coupling.

A visible light photoactive material such as dye or polymer or a narrow bandgap semiconductor is used as a sensitizer to generate electron hole pair upon illumination by visible light. The excited electron will be favorably injected into the conduction band of the host semiconductor (e.g. TiO_2) with a less negative redox potential as compared to the conduction band (CB)/lowest unoccupied molecular orbital (LUMO) of the sensitizer. The injected electrons will then hop over to the surface of the host semiconductor where they are scavenged by oxygen molecule to form super oxide radical ($O_2^- \cdot$) and hydrogen peroxide radical ($\cdot OOH$). These active radicals can attack organic pollutants and mineralize them to CO_2 and H_2O for a complete reaction. The sensitizer gets oxidized upon electron injection to the CB of the host semiconductor and is reduced back to the original oxidation state by accepting electrons from the adsorbed pollutants.

Table 2-1. Common surface modification techniques.

Surface Modification Techniques	Sensitizer
Dye Sensitization	Methylene blue (MB) [11], 8-hydroxyquinone (HOQ) [9], acid red 44 [10], Rhodamine B (RB) [11]
Polymer Sensitization	Poly fluorine-co-thiophene (PFT) [12, 52]
Semiconductor Coupling	Bi_2S_3 [16], CdS [14, 16], V_2O_5 [15], CdSe [17]

The common surface modification techniques and sensitizers are summarized in Table 2-1. These techniques are very powerful to render TiO_2 sensitive to visible light but with inherent drawbacks. For dye sensitization, the dye physically adsorbs

to the host semiconductor via weak Van der Waals interaction. Frequent dye desorption has hindered the use of this technique for practical applications [53]. And the oxidized sensitizer needs to be regenerated with a suitable electron donor to prevent the destruction of dye [54]. Polymers such as poly fluorine-co-thiophene (PFT) are more stable sensitizers in water as compared to dye due to their low solubility in water, giving rise to higher degradation rate on VOC, e.g. phenol [12]. However, the red shift towards visible light is very limited, only up to 500 nm [12, 52]. Coupling TiO_2 with a narrow bandgap semiconductor (normally in core-shell structure) can effectively extend its photo-response to the visible light range and achieve charge carrier separation simultaneously. However, photo-corrosion of the sensitizer has been reported since holes are left behind in the valence band (VB) of the sensitizer without being consumed [14].

2.2.2.2 Bandgap Engineering

Various bandgap modification techniques are also employed to extend the photoresponse of TiO_2 into visible light range, including via creating oxygen vacancies and oxygen sub-stoichiometry [18, 19] and by doping TiO_2 with transition metals [20-23] and non-metals [19, 24-27].

Creation of Oxygen Vacancies

TiO_2 is reported to exhibit photocatalytic activity under visible light irradiation via creation of oxygen vacancies [18, 19] in its crystal structure. The oxygen vacancies can be easily introduced at the grain boundaries of the polycrystalline samples via

means such as plasma treatment, generating grain boundary defect state about 0.75 eV and 1.18 eV below the conduction band (CB) of TiO_2 [18]. Since the oxygen defect states are close to the CB, electrons trapped can be easily promoted to CB via visible light absorption, rendering TiO_2 visible light active. Nakamura et al. has extended the photo-response of TiO_2 to 600 nm for plasma treated TiO_2 [18].

Transition Metal Doping

Doping of transition metals including Fe [20], Cr [21], Cu [22] and Ni [23] at the Ti site of TiO_2 has been reported. These impurity ions create local energy band within the forbidden band of the host TiO_2, effectively narrowing the bandgap to approach the energy of visible light. Therefore, electrons from the introduced impurity state will absorb visible light photons to initiate the photocatalytic reactions. However, Bouras et al. has reported that transition metal doping may lead to loss of crystallinity and phase transformation to rutile, reducing the photocatalytic efficiency [20]. In addition, metal doping often suffers from thermal instability or is more prone to serve as recombination centers due to the dopants' localized d-states deep in the band gap of TiO_2 [55]. Pichat's research on oxidation of propene and 2-propanol with Cr-doped TiO_2 discovered that increase in electron-hole recombination at the Cr^{3+} ion sites has hindered the efficiency of the reaction [21].

Non-metal Doping

Asahi's report of N-TiO_2 as a visible light active photocatalyst in 2001 [24] was considered as a breakthrough to trigger tremendous research on anion-doped TiO_2 in recent years, although Sato has reported the NO_x-doped TiO_2 for improved visible

light photocatalytic performance on CO and ethane much earlier in 1986 [56]. Non-metal doping including N [24, 25], S [26], and C [27] was reported to shift the absorption threshold of TiO_2 more into the visible light range than the metal doping and has become an attractive choice for visible light-active TiO_2.

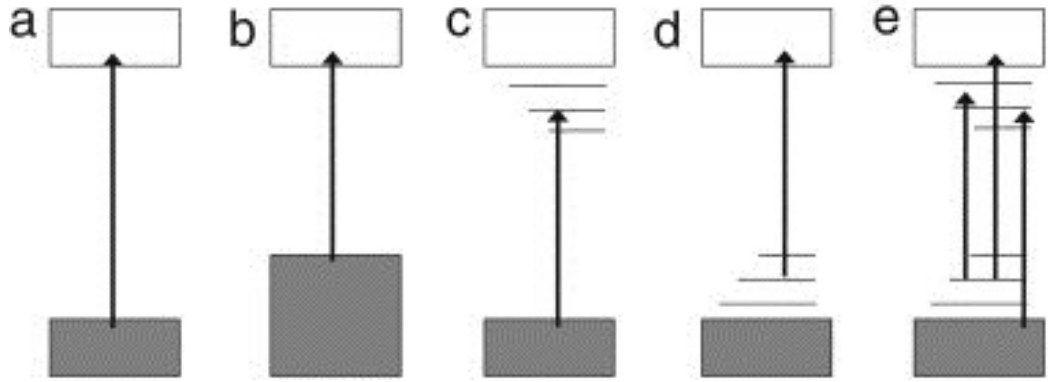

Figure 2-4. Various schemes illustrating the possible excitation processes of visible-light-responsive TiO_2 materials: (a) pristine TiO_2, (b) band gap narrowing model, (c) oxygen-deficient TiO_2, (d) localized midgap model, and (e) coexistence of oxygen deficiency and non-metal doped midgap levels [59].

Various postulations were developed to explain for the origin of the visible light absorption of anion-doped TiO_2. Asahi et al. suggested the mixing of N 2p level with the O 2p valence band for effective bandgap narrowing of TiO_2 to induce visible light absorption (Figure 2-4(b)) [24]. However, based on Lin et. al's calculation, the N 2p will still be localized midgap states just above the O 2p band even for a nitrogen concentration as high as 12.5% (Figure 2-4(d) and (e)); the mixing of N 2p with O 2p bands will require at least 20% N doping [57], which will practically result in the formation of TiN. A similar conclusion was drawn by Tachikawa et al. in

transient spectroscopy studies on C- and S-doped TiO_2 [58]. In addition to the non-metal states, it is often neglected that the oxygen vacancies formed due to the anion doping also introduces midgap states below the conduction band of TiO_2 (Figure 2-4(c) and (e)) and contributes to the visible light absorption [57].

2.2.2.3 Proposed Visible Light-Active Photocatalyst: Carbon-Doped TiO_2 via Thermal Oxidation of TiC

Among the three commonly studied anion dopants including N, C and S, nitrogen doping is the most extensively studied following the work of Asahi [24]. However, carbon doping was suggested to be the most promising based on the theoretical calculation by Wang and Lewis, due to a significant overlap between the O 2p state and the C 2p state near the valence band edge and thus the production of the largest valence band red shift [28]. Some C-TiO_2 photocatalytic products, like Kronos VLP series, have already been commercialized in the market [60]. In particular, Kronos vlp 7000 meant for visible light photocatalytic applications have been proven effective on a host of pollutants [61]. However, the maximum allowed processing temperature of 150 ºC has hindered the further modifications of this material for improvement on the photocatalytic efficiency.

There are various methods for preparation of C-TiO_2, including sol gel method [62], direct burning of titanium metal in natural gas flame [63], annealing TiO_2 under CO gas flow at high temperatures (500-800 ºC) [64] or thermal oxidation of TiC [65-69]. Among all, thermal oxidation of TiC has received relatively less attention, yet appears to be a repeatable process due to ease of control in the doping process. As it

is believed that higher temperature annealing would completely oxidize the TiC to form TiO_2, the few works as listed in Table 2-2 [65-69] normally employed mild oxidation of TiC at 350 °C with an optimized annealing time of 8-100 hours, which is very time-consuming. Oxidative annealing at higher temperature with reduced time could in fact yield C-TiO_2 with similar or better photocatalytic performance, which is more suitable for mass production of C-TiO_2.

Table 2-2. Preparation of C-TiO_2 by thermal oxidation of TiC in literature.

References	Oxidation conditions	C-TiO_2 size/phase information	Visible light photocatalytic performance evaluation
[65]	350 ºC for 36 hr in air followed by annealing at 600 ºC for 5 hr under O_2 flow	Anatase phase	IPA decomposition
[66, 67]	350 ºC for 5, 10, 50, and100 hr, 400 ºC for 20 hr, 600 ºC for 4 hr and 800 ºC for 2 hr in air	200-800 nm by SEM, anatase or anatase-rutile mixed phase	Methylene blue degradation
[68]	200-400 ºC for 4-16 hr in air	1 μm by SEM, anatase-rutile mixed phase	Trichloroacetic acid degradation
[69]	350 ºC for 50 hr in air followed by annealing at 400 ºC for 10 hr in air	1-2 μm by SEM, anatase phase	Water photooxidation

In the current project, formation of C-TiO_2 by oxidation of TiC at more aggressive process (at higher temperature of 400-600 °C with significantly reduced annealing time of 2 hours) is studied systematically in parallel with the mild oxidation process of TiC (at 350 °C for 2-50 hours) in an attempt to develop a simple and cost-effective

process for mass-production of visible light-active photocatalytic C-TiO_2 nanoparticles. The states of carbon in the TiO_2 lattice will be elucidated via various characterization techniques and the possible band structure and visible light photocatalytic mechanism of C-TiO_2 will be proposed.

2.2.3 Strategies to Enhance Charge Carrier Separation in TiO_2

To enhance the charge carriers separation so as to improve the overall quantum efficiency of TiO_2, strategies such as morphological modifications or chemical modifications have been adopted [34].

Examples of the morphological modifications include highly dispersed TiO_2 and TiO_2 nanotubes [70]. The advantages lie in the prolonged lifetime of the charge-transfer excited state of highly dispersed TiO_2 as compared to that of bulk TiO_2 materials, and the long diffusion length of charge carriers along the nanotube axis and low recombination at grain boundaries in TiO_2 nanotube, both giving rise to enhanced photoactivity [70].

Chemical modifications involve coupling or incorporation of additional components in the TiO_2 structure, such as coupling of TiO_2 with other semiconductors or load the TiO_2 surface with noble metals [70]. P25 TiO_2 with mixed phases of anatase and rutile is one special example of semiconductor coupling. Its excellent photocatalytic performance can be attributed to the intimate contact of the two phases. As the rutile phase can act as an electron sink for photogenerated electrons from the conduction band of the anatase phase due to the more positive conduction band potential of rutile

as compared to anatase, the separation of photogenerated electrons and holes can be enhanced, inhibiting the charge carriers recombination and thus improving the photocatalytic efficiency [34]. For TiO_2 loaded with noble metal, the noble metal can form a Schottky barrier with the TiO_2 surface to conduct away the photogenerated electrons irreversibly [35, 36], achieving spatial charge separation.

In this project, after the synthesis conditions for C-TiO_2 by thermal oxidation of TiC are optimized, co-doping of C and Pt/Ag will be studied for enhanced charge carrier separation to further improve the photocatalytic efficiency of C-TiO_2.

2.3 Application of TiO_2 Photocatalysis in Environmental Remediation

Owning to the strong oxidative decomposition capabilities with the use of only natural light and operating at near ambient temperature, TiO_2-based photocatalysts have been widely used in air cleaning, water purification, and microorganism disinfection applications. The major category of pollutants in these applications together with their reaction mechanisms or pathways will be briefly reviewed in the following sections.

2.3.1 Air Cleaning

Under suitable light irradiation, TiO_2-based photocatalysts can completely oxidize air pollutants into CO_2, H_2O and mineral acids giving sufficient O_2 supply and illumination [59]. This air-solid heterogeneous reaction can be influenced by a

number of parameters including light intensity/source, photocatalyst loading, pollutant concentration, humidity level, O_2 partial pressure, reaction temperature, gas flow rate and substrate type etc. The generation of byproducts can also affect the reaction rate and sometimes may lead to deactivation of photocatalysts due to blocking of active sites [59].

Among all the gaseous pollutants, volatile organic compounds (VOCs) are considered as one of the most important category of pollutants both in indoor and outdoor environment. They are organic compounds that have high enough vapor pressures under normal conditions to significantly vaporize and enter into the atmosphere, and typically belong to several categories of compounds, namely aldehydes, aromatics, alcohols and ketones.

2.3.1.1 Aldehydes

The aldehydes with a sharp and pungent smell are commonly encountered since they are frequently used as cleaning agents, biocides and constituents of resins. They follow the "First Member Rule" in that formaldehyde is the most toxic of the group [71]. Liu et al. has described the photocatalytic rate of formaldehyde over TiO_2 by Langmuir–Hinshelwood model and found CO as one of the byproducts [72]. Besides CO, Ao et al. has discovered formic acid as another important intermediate [73]. The mineralization of formaldehyde and the generation of formic acid decreased with increasing humidity levels [8]. The other aldehydes such as propionaldehyde and acetaldehyde were found to photocatalytically oxidized to corresponding acids, shorter carbon chain aldehydes, CO_2 and H_2O [8, 74]. However, in the case of

butyraldehyde, it was found that the active oxygen pathway involving the transformation from aldehydes into acids and subsequently shorter carbon chain aldehydes is favored as compared to the pathway involving hydroxyl group [74].

2.3.1.2 Aromatics

Most of the more commonly encountered organics found indoor are volatile aromatic hydrocarbons since they are most frequently used in solvents. The aromatic group also follows the "First Member Rule" with benzene as the most toxic member. The photocatalytic pathway of benzene has been presented by D'Hennezel et al. [75]. The major byproduct was phenol together with hydroquinone and 1,4-benzoquinone. Acetic and formic acids were also formed. Another mostly studied aromatic is toluene. It will react rapidly with O_2, but its intermediates will oxidize slowly into CO_2 [8]. D'Hennezel et al. have found benzoic acid, benzaldehyde, and benzyl alcohol as the three major intermediate products [75].

2.3.1.3 Alcohols

Alcohols are most frequently used as solvents, perfumes, cleaning agents and components of pharmaceuticals. Based on the review done by Mo et al. [8] on photodegradation of methanol, ethanol, and 1-butanol, they proposed the pathway for alcohol photodegradation: alcohols → aldehydes → acids → short carbon chain aldehydes and alcohols. The newly formed short chain aldehydes and alcohols will again follow similar reaction pathway to form methanol and formaldehyde, and finally CO_2 and H_2O. However, this pathway does not apply to 2-propanol [76].

2.3.1.4 Ketones

Ketones are occasionally found indoor and they are more as intermediate product in the PCO reaction. Raillard et al. have suggested the possible pathway for photodegradation of acetone to be: acetone → acetaldehyde + formic acid or CO_2 → formaldehyde + methanol → formic acid [77]. Vincent et al. have given another pathway: acetone → methyl ethyl ketone → acetalydehye [78]. In both cases, acetaldehyde is the main intermediate product.

2.3.2 Water Purification

Heterogeneous photocatalysis can completely degrade organic pollutants into CO_2, H_2O and inorganic ions ($Cl^-, Br^-, SO_4^{2-}, NO_3^-$ etc.) in aqueous environment. As compared to other advanced oxidation technologies including UV/O_3, UV/H_2O_2, and UV/Fenton, TiO_2-based photocatalysis requires oxygen as the only oxidant for simultaneous oxidative and reductive reactions on a broad range of organic and inorganic pollutants including alkane, halogenated hydrocarbon, alcohol, carboxylic acid, aromatics, polymers, dyes, surfactants, pesticides, and inorganic anions even in ppb range [3].

Photocatalytic water purification could be more complex than air cleaning due to the presence of both dissolved inorganic and organic species in the water system, which may strongly influence the rate and efficiency of the photocatalytic process [3]. For example, the dissolved anions ($Cl^-, ClO_4^-, SO_4^{2-}, NO_3^-, CO_3^{2-}, HCO_3^-, PO_4^{3-}$) can compete with the pollutants for reactive oxygen species, and decrease the reaction

rate of the pollutants. At the same time, these anions could form reactive radicals such as $SO_4^- \cdot$ during the photocatalytic process, and improve the degradation efficiency of the pollutants. Dissolved cations can promote the charge carrier separation by capturing the photogenerated electrons or holes and producing additional $OH \cdot$ through homogeneous Fenton-like reactions. However, the reaction will be inhibited if the concentration of cations is too high due to the filtering effect of the cations for UV absorption and precipitation of the dissolved metallic ions as hydroxides on the TiO_2 surface. Addition of inorganic oxidants such as $O^3, H_2O_2, ClO_4^-, BrO_3^-, S_2O_8^{2-}$ or adjustment of pH in the photocatalytic process can also affect the reaction rate significantly.

2.3.3 Microorganism Disinfection

Microbial pollutant is considered as the most important inducement for sick building syndrome (SBS) in pathognomy research [79]. Since the positive bactericidal effect of TiO_2 was first reported by Matsunaga in 1985 [80], TiO_2 as the leading candidate photocatalyst has been investigated extensively and proven effective on different types of microorganisms including bacteria [81, 82], viruses [83], algae [84], fungi [85], and tumor cells [86]. The sensitivity of microorganisms to TiO_2 photocatalysis is likely in the order of virus>bacterial cells (Gram-positive > Gram-negative > bacterial spores > fungi) [79].

Among all the microorganisms, *Escherichia coli* (*E. coli*), a Gram-negative bacterium, was extensively studied as a model microorganism, partly due to its rapid growth rate and simple nutritional requirements. Gram-positive *Enterococcus*

faecalis (*E. faecalis*) with different cell wall structure was often chosen as reference bacteria to *E. coli*. On top of the inner membrane, *E. coli* has a thin peptidoglycan layer and an additional outer membrane containing two lipid bilayers in its cell wall whereas *E. faecalis* only has a thicker and compacter peptidoglycan layer [87].

As compared to air cleaning and water purification, the microorganism disinfection is more complex due to the protection and recovery mechanism existing in microorganism cells. Thus, different reaction pathways have been proposed. Some of the important studies are discussed as follows.

The first proposed mechanism suggests that as a result of direct contact between photocatalyst and the target microorganism cell, the intracellular coenzyme A (CoA) is oxidized, inhibiting the cell respiration and leading to cell death [88].

The second photokilling mechanism suggests that bacterial death is caused by the disorder in cell permeability and decomposition of the cell walls [89] which can be best illustrated by a two-step process [90]. As shown in Figure 2-5, in the first stage, the cell outer membrane was partially decomposed by the reactive species produced by photocatalysis, such as $OH\cdot$ and $O_2^-\cdot$. The oxidation of organic cell wall components will subsequently induce disorder in cell permeability, leading to cell lysis and death. The proteins and nucleic acid etc. in the cell will also be destroyed by the ROS owning to their strong redox potentials [87].

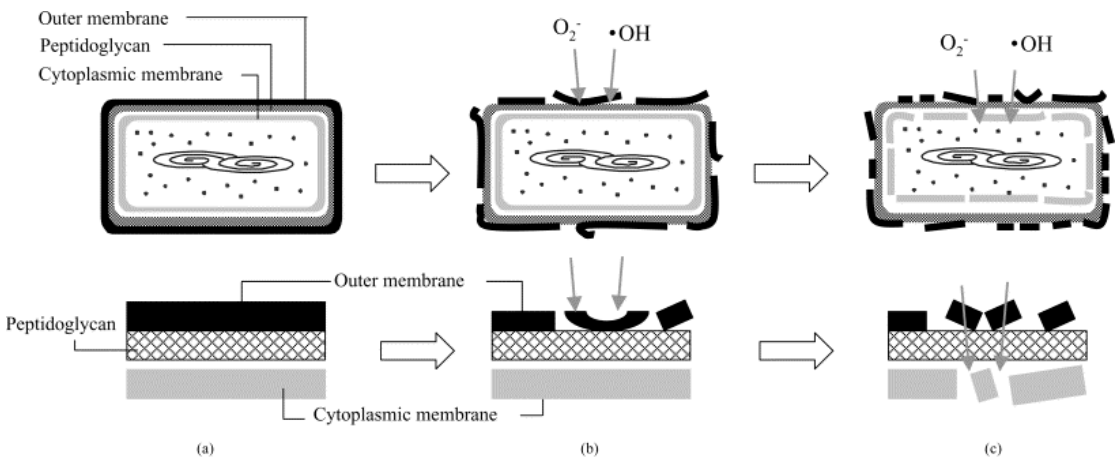

Figure 2-5. *E. coli* photokilling process on TiO_2 film [90].

In the case of TiO_2 photocatalysis, the irradiation of UV light will also cause cell damage by exciting photosensitive molecules within the cell and thus producing reactive species to adversely affect the genome and other intracellular molecules, resulting in cell mutations and growth delay [79].

In this project, the photocatalytic performance of the synthesized photocatalysts (C-TiO_2, Pt/C-TiO_2 and Ag/C-TiO_2) will be evaluated on selected pollutants including gaseous toluene, Rhodamine B, gram-negative *E. coli* and gram-positive *E. faecalis* in aqueous suspension for different environmental applications.

CHAPTER 3 : SYNTHESIS AND CHARACTERIZATION OF CARBON-DOPED TITANIUM DIOXIDE

In this chapter, we focus on the characterization of carbon-doped titanium dioxide (C-TiO_2) nanoparticles synthesized by thermal oxidation of titanium carbide (TiC). The thermal properties of the as-received TiC precursor were first studied by thermogravimetric analyzer (TGA) and differential thermal analyzer (DTA) to determine the suitable oxidation temperature and time for fabrication of C-TiO_2. The physicochemical properties of the synthesized nanoparticles were subsequently studied via various characterization tools. The effect of thermal oxidation on the crystallographic structure was characterized by X-ray diffractometry (XRD) and Raman spectroscopy. The surface morphology was monitored by Scanning Electron Microscopy (SEM), N_2 adsorption-desorption isotherms and Transmission Electron Microscopy (TEM). The surface bonding and elemental analysis was analyzed using Fourier transform infrared spectroscopy (FTIR) and X-ray photoelectron spectroscopy (XPS), focusing on the identification of the exact states of carbon in the TiO_2. UV-vis diffuse reflectance was used to confirm the successful extension of the absorption response into the visible light range due to introduction of carbon into the TiO_2 lattice or surface. Photoluminescence (PL) spectra were also recorded to investigate the fate of photogenerated carriers. With the above characterization

results, the band structure and possible visible light photocatalytic mechanism of the synthesized C-TiO_2 were finally proposed.

3.1 Synthesis of C-TiO_2

The thermal properties of the pristine nano-sized TiC (>99.0%, Hefei Kaier) were first measured using a Perkin Elmer thermogravimetric analyzer (TGA-7) and a differential thermal analyzer (DTA-7) with temperature scan from room temperature up to 800 °C at 10 °C/min in zero-air flow of 20 sccm. The simultaneous analysis of the weight gain and heat evolution provides useful information to determine the oxidation conditions for the synthesis of C-TiO_2.

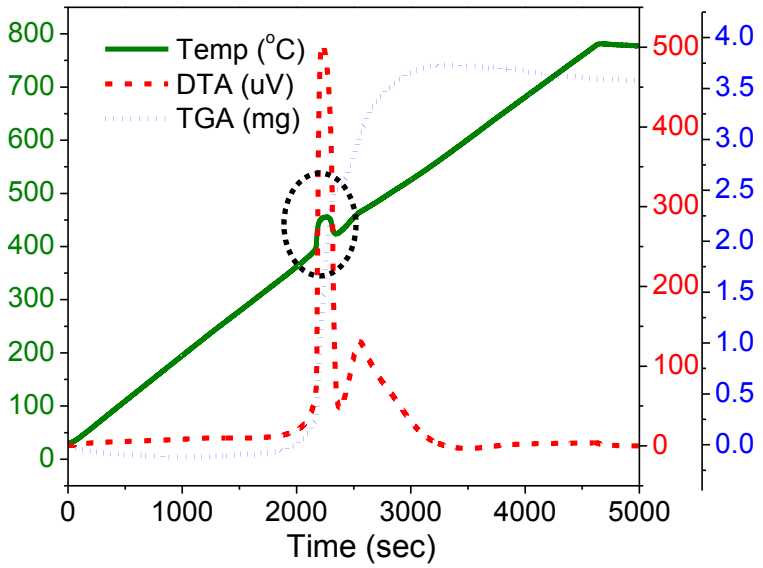

Figure 3-1. DTA-TGA curves of the TiC in air atmosphere.

As shown in Figure 3-1, during the heat up stage, a small weight loss of the TiC precursor was first noted below 200 °C due to the moisture desorption. The mild

oxidation of TiC occurred between 250-380 °C. Beyond 380 °C, strong oxidation began fiercely , as evidenced by an extremely strong exothermic peak (500 μV) between 380-425 °C and a 18% weight gain as compared to the original weight of 13.3 mg, possibly attributed to the consecutive reaction of TiC → oxycarbide (TiC_xO_{1-x}) → titanium suboxide (TiO, Ti_3O_5, or Ti_4O_9) → TiO_2, accompanying the large evolution of heat and CO_2 gas [91]. The inability to release the heat in time could result in a self-combustion condition, as indicated by the sudden elevation of oven temperature by 60 °C. A more controlled oxidation followed thereafter with an additional 9% weight gain and an exothermic peak centered at 470 °C, which could be associated with the transformation from anatase to rutile.

Based on the thermal analysis and taking into consideration of the larger packing volume and faster temperature ramping in the actual synthesis process, a calcination temperature of 350-600 °C was chosen for systematic study of the oxidation of TiC. The TiC was oxidized at 350 °C for 2-50 hours for mild oxidation study, similar to the few published works [60, 67, 68, 92, 93]. Meanwhile, oxidation of TiC with a more aggressive process at higher temperature of 400-600 °C was studied in parallel with significantly reduced annealing time of 2 hours in an attempt to develop a simple and cost-effective process for mass-production of visible light-active photocatalytic C-TiO_2 nanoparticles.

In a typical synthesis procedure, the pristine TiC nanoparticles were bestrewed on an alumina combustion boat and loaded into the muffle furnace (F62700, Barnstead) at room temperature. The furnace was then rapidly heated up in air within 30 minutes to reach the target temperature of 350-600 ºC and maintained for 2-50 hours for the

oxidation of the TiC into C-TiO_2 with different carbon : oxygen and anatase : rutile ratios. The black TiC powders turned into whitish-gray color after oxidation. The synthesized C-TiO_2 was denoted as CT-A-B where A and B refer to the oxidation temperature and time, respectively.

3.2 Characterization of C-TiO_2

3.2.1 Crystallographic Study

3.2.1.1 X-Ray Diffraction Spectra

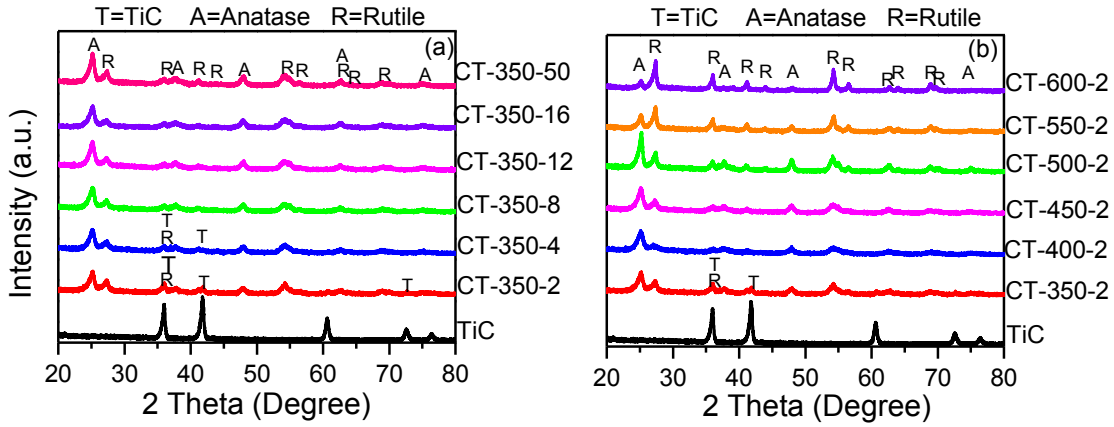

Figure 3-2. XRD patterns of C-TiO_2 synthesized at (a) 350 ºC for 2-50 hours and (b) 350-600 ºC for 2 hours.

X-ray diffraction (XRD) patterns were obtained to determine the TiO_2 phase formation using a Simens D5005 diffractometer with an X-ray source of 1.54 Å Cu

Kα. The accelerating voltage and applied current were 40 kV and 40 mA, respectively.

The XRD patterns of the as-prepared C-TiO_2 samples are presented in Figure 3-2. The conversion of the pristine TiC (JCPDS 65-0971) was complete after 8 hours of mild oxidation at 350 °C (CT-350-8) or after 2 hours of more aggressive oxidation above 400 °C (CT-400-2). Mixed phase of anatase (JCPDS21-1272) and rutile (JCPDS 65-1119) TiO_2 was observed in all the samples. The presence of rutile TiO_2 phase may help to enhance the charge separation by electron migration from conduction band of rutile to that of anatase [94]. The appearance of the rutile phase at such low temperatures could be explained by the self-combustion process accompanied with an uncontrollably higher oven temperature as discussed in Section 3.1.

Based on the XRD, the phase composition and crystallite size were estimated and summarized in Table 3-1 in comparison to commercial TiO_2 P25. The rutile content remained virtually the same at ca. 30% with prolonged oxidation at 350 ºC or increased oxidation temperature up to 500 ºC, resembling the phase structure of the P25 TiO_2 powder with high photoactivity [94]. With further increase in oxidation temperature, the rutile phase increased abruptly and became the more dominant phase as expected, approaching 89.7% at 600 ºC (CT-600-2). The crystallite size of the TiC precursor was estimated to be ca.15.5 nm based on the strongest peak at 2θ = 41.7°. Upon oxidation, the crystallite size of the synthesized C-TiO_2 nanoparticles followed a trend of first-decrease and then-increase with prolonged oxidation at 350 ºC or higher oxidation temperature of 400-600 ºC. This observation could be

explained by the grain cracking of TiC to allow renucleation of TiO_2 with much smaller crystallite size to be observed. At the same time, the dispersed carbon atoms from the broken Ti-C bond could retard the grain growth of the newly formed anatase and rutile crystalline phases [95]. Once the recovery and recrystallization were completed, grain growth was resumed to further reduce the internal energy.

Table 3-1. Summary of phase composition and crystallite size of the photocatalysts.

Sample	rutile content [a]	crystallite size (nm) [b]	
		anatase	rutile
CT-350-2	30.1	9.6	6.4
CT-350-8	30.1	9.6	5.2
CT-350-16	30.4	8.7	4.9
CT-350-50	30.9	9.5	6.6
CT-400-2	30.2	7.0	5.8
CT-450-2	31.2	7.7	5.3
CT-500-2	31.0	9.8	5.4
CT-550-2	66.1	11.9	10.4
CT-600-2	89.7	18.7	15.8
P25	23.7	14.9	11.4

[a] Rutile content=$(1+0.8I_A/I_R)^{-1}$ where I_A and I_R are the X-ray intensities of the anatase and the rutile peaks at Bragg peaks $2\theta = 25.1°$ and 27.3° respectively

[b] Estimated with Scherrer Formula $D=0.94\lambda/\beta\cos\theta$

In summary, the XRD reveals TiO_2 phase formation at 350 °C. The removal of the pristine TiC was complete after 8 hours at 350 °C or after 2 hours above 400 °C. The rutile content remained at ca. 30% with oxidation up to 500 °C for 2 hours and

became the dominant phase with further increase in oxidation temperature. The crystallite size was found shrinking as compared to the pristine TiC during initial oxidation stage, due to grain cracking and renucleation of TiO_2 clusters as well as the dispersed carbon atom. Grain growth was observed again once recovery and recrystallisation were complete to further reduce the internal energy.

3.2.1.2 Raman Spectra

A Raman spectroscopy (Witec alpha 300R) equipped with a green laser source (532 nm) was used to analyse the Raman spectra of the synthesized C-TiO_2 in pellet form.

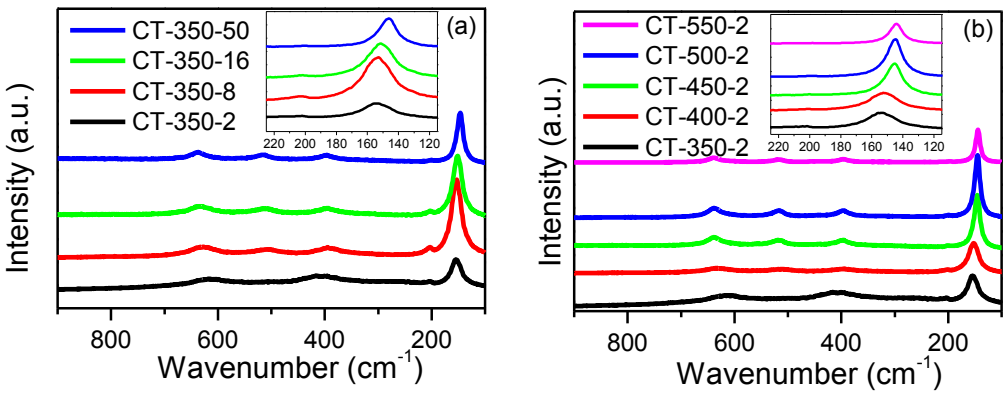

Figure 3-3. Raman spectra of C-TiO_2 synthesized at (a) 350 ºC for 2-50 hours and (b) 350-600 ºC for 2 hours with the inset showing expanded part of the spectra.

As shown in Figure 3-3, backscattered Raman signals were collected and recorded from 900 to 100 cm^{-1} with a resolution of 0.8 cm^{-1} to analyze the formation of TiO_2. The observed peak at around 638 cm^{-1} (E_g), 516 cm^{-1} (A_{1g}), 396 cm^{-1} (B_{1g}), 200 cm^{-1} (E_g, very weak), and 146 cm^{-1} (E_g) can be attributed to the characteristics peaks of the predominant anatase phase [96]. The four fundamental Raman bands due to rutile

phase at 826 cm^{-1} (B_{2g}), 612 cm^{-1} (A_{lg}), 447 cm^{-1} (Eg) and 143 cm^{-1} (B_{1g}) were not distinct, suggesting anatase TiO_2 as the dominant phase, which is consistent with the XRD analysis. Closer inspection of the strongest and sharpest peak at around 146 cm^{-1} revealed a red shift towards lower wavenumber for prolonged oxidation time at mild oxidation temperature of 350 ^{o}C or higher oxidation temperature from 400 to 600 ^{o}C, indicating the reduction of surface defects due to temperature processing [97]. The initial increase in peak intensity can be ascribed to the enhanced crystallinity due to the formation of anatse TiO_2 while the later reduction could be due to the increase in rutile content whose B_{1g} mode (143 cm^{-1}) is at similar frequency but weak in signals [96].

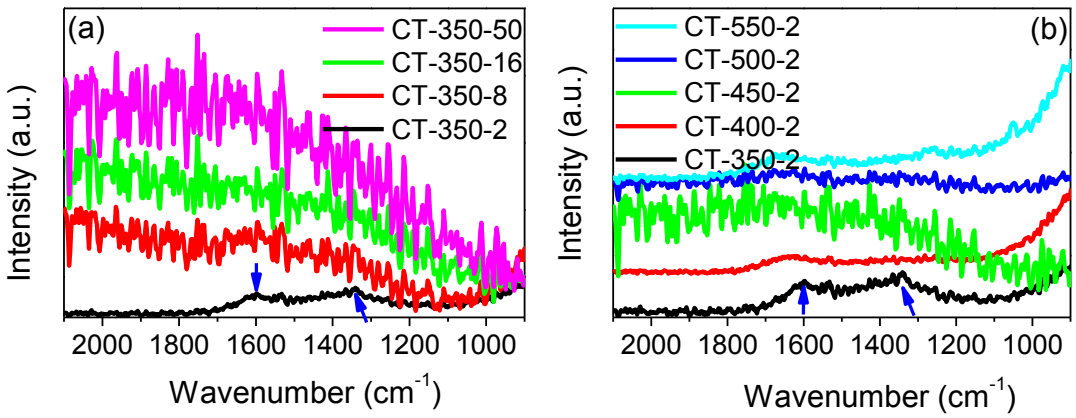

Figure 3-4. Raman spectra of C-TiO_2 synthesized at (a) 350 ºC for 2-50 hours and (b) 350-600 ºC for 2 hours exhibiting graphitic modes.

In the XRD investigation, it is believed that the dispersed carbon atom was involved in the initial oxidation stage to suppress the grain growth. However, no carbon peak was identified to support this hypothesis. Backscattered Raman signals were

collected and recorded from 2100 to 900 cm^{-1} to identify the presence of carbon species.

As shown in Figure 3-4, in the initial oxidation stage (CT-350-2), two very weak peaks corresponding to the G-band and D-band of amorphous carbon were observed [93], ascribed to carbon diffusion after Ti-C bond breaking. The G-band centering at around 1600 cm^{-1} is E_{2g} Raman active mode of graphite composed of local sp^2-bonded structure while the D-band centering near 1350 cm^{-1} is often associated with bond-angle disorders and asymmetry lattices in graphitic structure [98]. With increasing oxidation time or temperature, the D-band became almost indistinguishable with weakened intensity, suggesting the removal of bond-angle disorder. However, it should be noted that the absolute peak intensity may vary depending on the relative phase content of the laser excitation area. Changes in band frequency are more worth noting. The two bands separated further apart with the G-band to higher frequencies, suggesting the increased graphitic ordering [93]. It is very likely that carbon near the surface of C-TiO_2 was present as graphite-like carbonaceous species, similar to the observation by Chen et al. in the study of C-TiO_2 through precipitation of tetrabutyl titanate in water [99] .

In summary, Raman spectra show anatase as the predominant phase for the synthesized C-TiO_2. Shift of the E_g peak at 146 cm^{-1} towards lower frequency suggests the reduction of surface defects with increased oxidation time or temperature. Amorphous carbon with mixed sp^2 and sp^3 bonds was revealed, ascertaining the diffusion of carbon from TiC upon annealing. With increasing

oxidation time or temperature, the structure became more graphitic-ordered as suggested by the shifting of G-band to higher frequencies and weakening of D-band.

3.2.2 Surface Morphology

3.2.2.1 Field-Emission Scanning Electron Microscopy

The morphology of the C-TiO_2 in coated form was observed using the field-emission scanning electron microscope (FESEM, JEOL JSM-7600F). The C-TiO_2 coating was prepared as follows: 1) 3 gram of nano-sized TiC was added into 20 mL ethanol in a 30 mL beaker and stirred at 350 rpm for 10 min; 2) 9 mL terpineol was added into the beaker subsequently and stirred at 600 rpm for 5 min; 3) the mixture was heated at 80 ºC at 700 rpm for 6 hours to evaporate the ethanol to obtain a viscous paste; 4) the paste was applied onto the conducting fluorine-doped tin oxide (FTO)-glass substrate by doctor blading method [100] using adhesive tape (Scotch brand) as a frame and spacer; 5) the coated glass was dried at 70 ºC for 30 min and subject to oxidation in the muffle furnace (F62700, Barnstead) for preparation of C-TiO_2 coating at 350-550 ºC for 2-50 hours.

As shown in Figure 3-5, CT-350-2 showed a non-uniform size distribution in the range of 20-100 nm. CT-500-2 exhibited similar morphology with slightly increased particle size of 40-100 nm. Agglomeration of particles in large aggregates of ca. 200 nm was also observed in both samples, possibly due to the sintering process as well as the long-time stirring of TiC precursor in ethanol during the paste preparation. The particle size of the C-TiO_2 could be smaller in powder form than in the coated form.

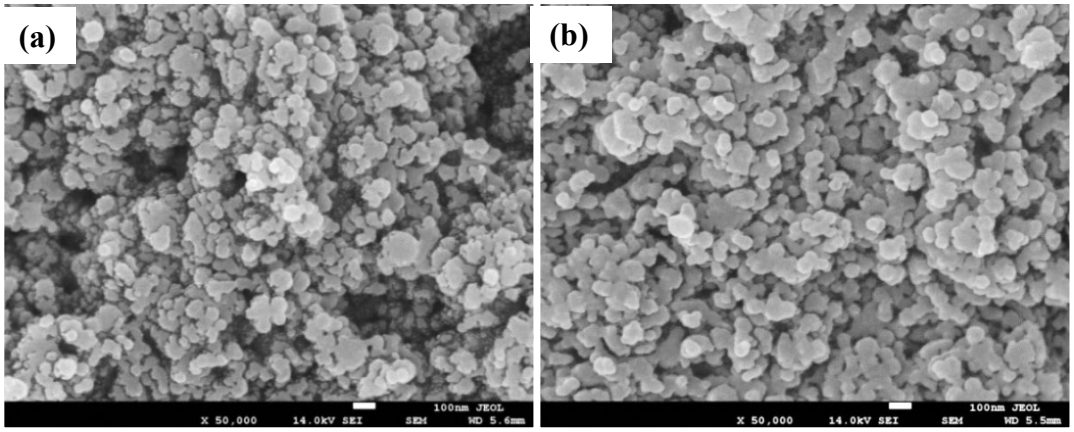

Figure 3-5. FESEM morphology of (a) CT-350-2 and (b) CT-500-2.

The specific surface area (SSA) of the C-TiO_2 particles was measured at liquid nitrogen temperature (77 K) with Micromeritics ASAP 2020 based on Brunauer, Teller and Emmet (BET) model in order to correlate with the FESEM observation. Before analysis, the powder samples were de-gassed at 200 °C under vacuum for 2 hours.

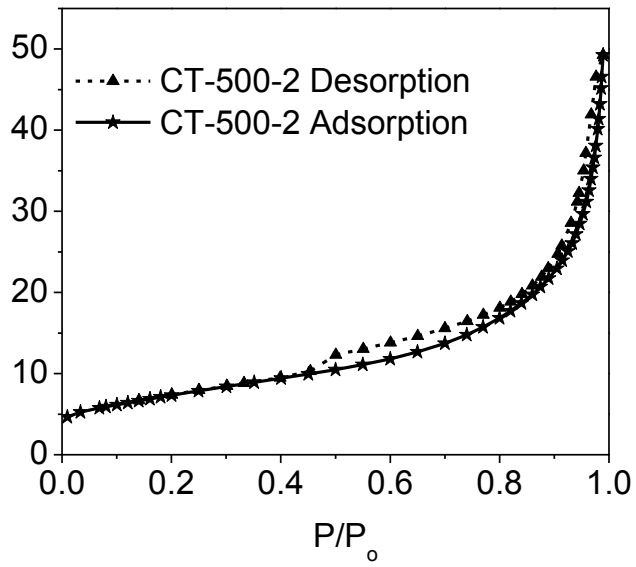

Figure 3-6. N_2 absorption-desorption isotherm for CT-500-2.

The typical N_2 absorption-desorption isotherm of the synthesized C-TiO_2 is shown in Figure 3-6. It is of type IV isotherm with hysteresis loop according to IUPAC classification, which is characteristic of mesoporous materials. The H3 hysteresis loop without any limiting adsorption at high P/P_o indicates the formation of aggregates, giving rise to slit-shaped pores [101], which is in good agreement with the FESEM observation. At high gas pressure, complete coverage of the powder samples by N_2 gas molecules can be achieved to fill all the pores. The pore diameter, volume and distribution can be derived from the Barrett-Joyner-Halenda (BJH) desorption isotherms by BJH calculation.

Table 3-2. BET surface area and BJH pore information for C-TiO_2.

Sample	BET SSA (m^2/g)	BJH pore size (nm)	Particle size (nm) *
TiC#	23.0	NA	50.0
CT-350-2	31.9	10.3	48.3
CT-350-8	32.6	10.0	47.1
CT-350-16	35.2	9.9	43.7
CT-350-50	30.5	9.9	50.5
CT-400-2	44.1	9.4	34.9
CT-450-2	30.8	10.3	49.9
CT-500-2	26.6	11.6	57.9
CT-550-2	15.6	14.8	98.5
Kronos	297.4	5.0	5.2

* $d_{BET} = 6/S_{BET}\rho$ assuming the particles are roughly spherical, $\rho_{TiO2\ anatase} = 3.90\ g/cm^3$ [102]

Information obtained from the supplier Hefei Kaier Nanometer Energy & technology

The BET surface area, BJH pore size and the estimated particle size of the synthesized C-TiO_2 were summarized in Table 3-2.

The estimated average particle size of 48.3 nm for CT-350-2 and 57.9 nm for CT-500-2 are consistent with FESEM observation as well. In general, the BET surface area of the synthesized C-TiO_2 is satisfactory in the range of 15-45 m^2/g, which is approaching that of the commercial TiO_2 Degussa P25 (~50 m^2/g), yet much lower than that of the commercial visible light-active C-TiO_2 Kronos vlp 7000 (~300 m^2/g). With prolonged oxidation time at 350 ºC, the BET surface area increased from 23.0 m^2/g for the pristine TiC to 35.2 m^2/g for CT-350-16 and then decreased again to 30.5 m^2/g for CT-350-50. With increased oxidation temperature in the range of 350-550 ºC for 2 hours, the surface area follows similar trend by increasing to 44.1 m^2/g for CT-400-2 first and then reduced drastically to 15.6 m^2/g for CT-550-2. The change in BET surface area corresponds to a first-decrease and then-increase particle size, which is in good agreement with the trend of crystallite size as determined by the XRD analysis. The initial decrease of particle size is caused by the continuous cracking of the original TiC grains and renucleation of the TiO_2 grains while the later increase of size is due to grain growth after the completion of recrystallization. Apparently, the oxidation temperature has a much higher impact on the change of particle size than the oxidation time. The BJH desorption isotherm shows that the synthesized C-TiO_2 samples have an average pore diameter of 9.4-14.8 nm, consistent with the characteristics of mesoporous materials.

3.2.2.2 Transmission Electron Microscopy

Further insights into the effect of oxidation on the morphology and structure of the pristine TiC can be obtained by Transmission Electron Microscopy (TEM) observations (JEOL JEM-2100F). The TEM samples were prepared by dispersing the

powders in ethanol via ultrasonication and subsequently dropping the dispersion onto carbon copper grids.

Error! Reference source not found.(a) shows a TEM bright-filed image of the pristine TiC appearing as large and compact particles with diameter falling in the range of 20-100 nm. Many TiC particles possessed a well-developed hexagonal characteristic, indicating the faster growth rate on the TiC {110} side facets than on the (111) facet [103]. HRTEM as shown in **Error! Reference source not found.**(b) revealed lattice atomic images of 0.217 nm and 0.250 nm, matching well with the d-spacing of (200) and (111) planes in TiC. The selected area electron diffraction (SAED) pattern shown in the upper right inset further confirmed the single crystalline nature of the pristine TiC. After oxidation, TEM and HRTEM images of CT-350-2 (Figure 3-8) showed clear core-shell structure polycrystalline in nature, which may serve as a paradigm to link with the incomplete oxidation unveiled in the XRD analysis with residual TiC precursors. A close examination at the core revealed atomic images of 0.339 nm corresponding to (002) plane of the partially graphitized carbon phase [104], as well as amorphous structure possibly attributed to mixture of residual TiC, amorphous carbon, and TiO_2. The shell was mainly composed of anatase (101) planes and rutile (110) planes with lattice atomic images of 0.352 nm and 0.324 nm respectively, in good agreement with XRD analysis. With more aggressive oxidation at 500 ºC for 2 hours, the crystallinity was enhanced significantly (Figure 3-9), allowing clear identification of rutile (110) planes and anatase (101) planes of TiO_2.

In summary, FESEM revealed a non-uniform size distribution of C-TiO_2 nanoparticles in the range of 20-100 nm, consistent with the particle size estimated by BET surface area. The particle size followed a first-decrease then-increase trend with increasing oxidation time/temperature, in good agreement with the change of grain size based on XRD analysis. The gradual oxidation of single crystalline TiC precursor to TiO_2 was clearly observed by TEM and HRTEM. For CT-350-2, core shell structure was observed due to incomplete oxidation, ascertaining the XRD analysis. Better crystallinity was achieved with higher oxidation temperature of 500 ºC. For both samples, mixed phase of anatse and rutile was observed, resembling the phase structure of commercial P25, which was reported to be beneficial to interfacial charge transfer [94].

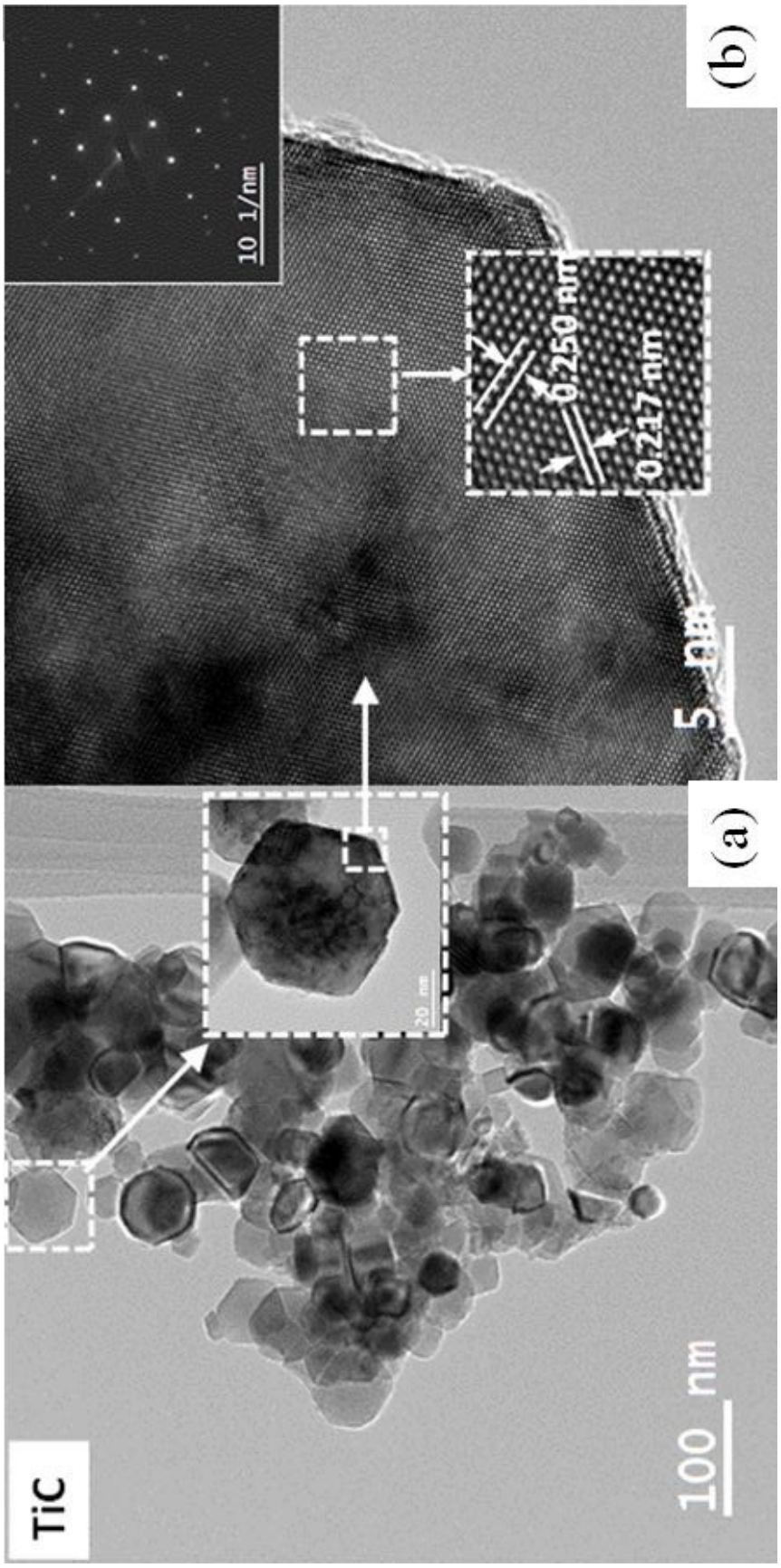

Figure 3-7. TEM and HRTEM images of pristine TiC.

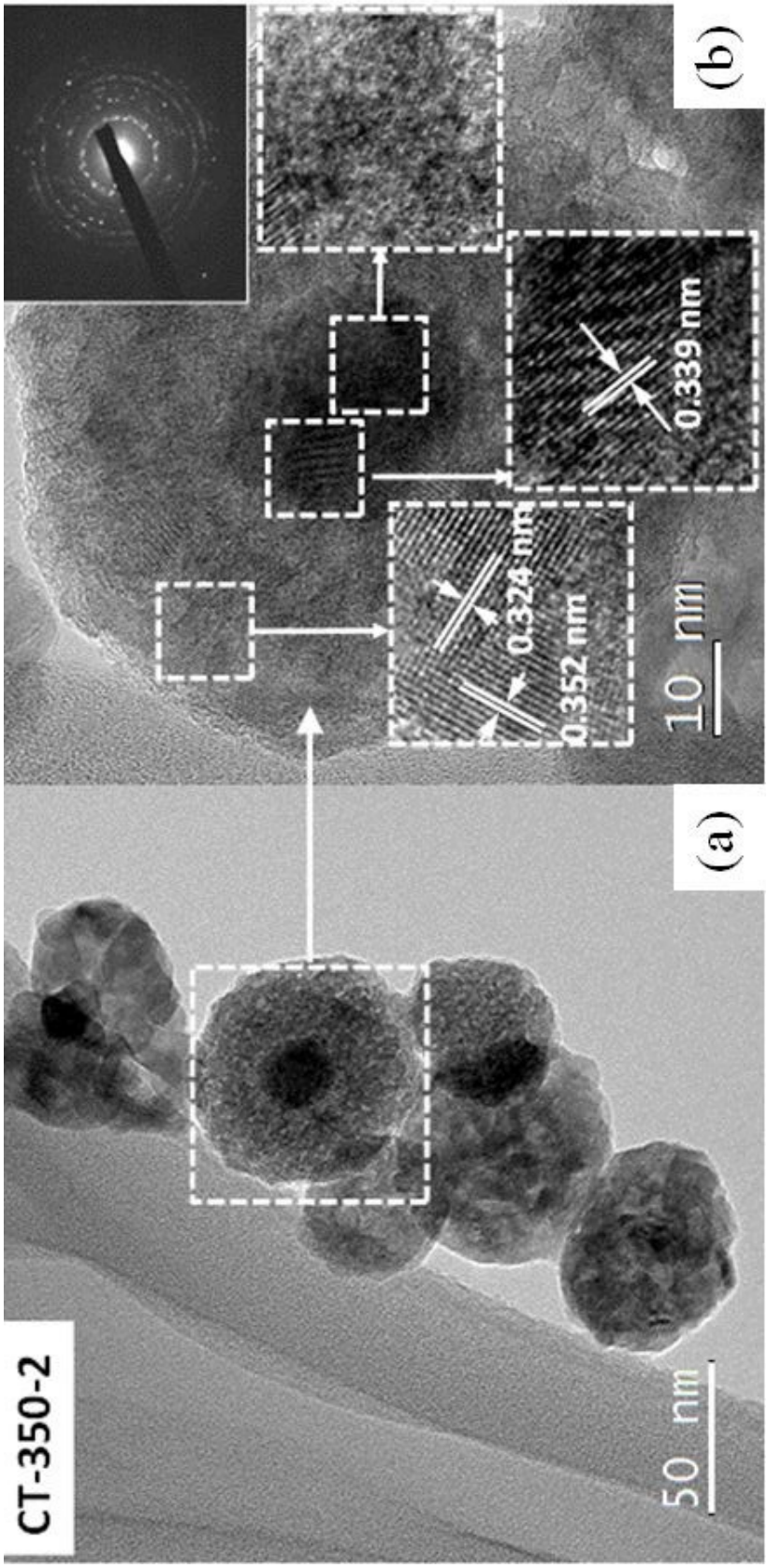

Figure 3-8. TEM and HRTEM images of CT-350-2.

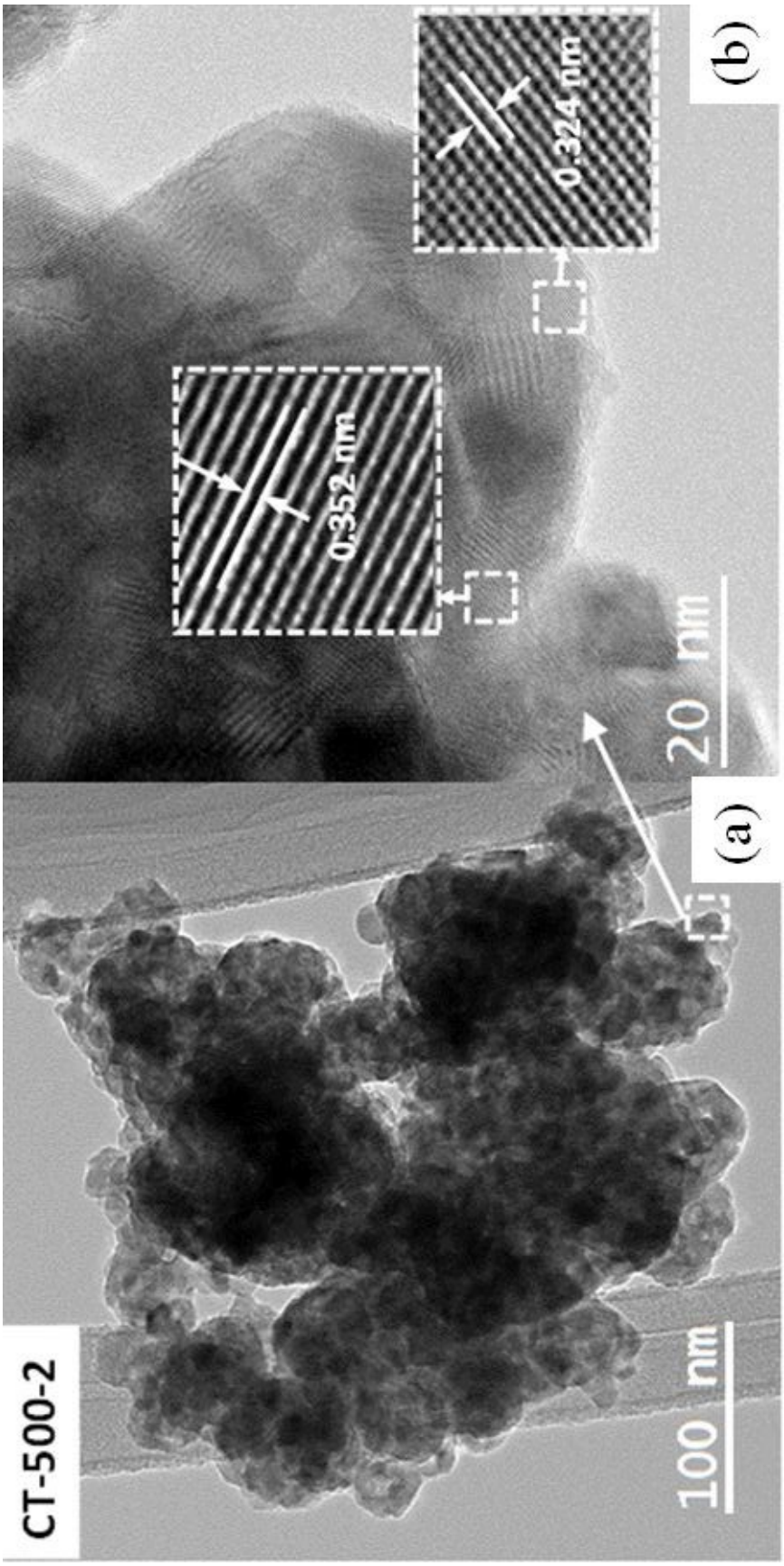

Figure 3-9. TEM and HRTEM images of CT-500-2.

3.2.3 Surface Chemical Analysis

3.2.3.1 Surface Hydrophilicity and Chemical Bonding Analysis

FTIR analysis was carried out for the examination of surface hydroxyl groups and chemical bonding of the synthesized C-TiO_2 in comparison to the commercial visible light-active C-TiO_2 (Kronos vlp 7000). Infrared spectra were recorded relative to air on KBr pellets (powder: KBr=1:100 by weight) in the range of 4000-400 cm^{-1} at the scan rate of 4 cm^{-1} by a FTIR spectrophotometer (Shimadzu IRPrestige-21).

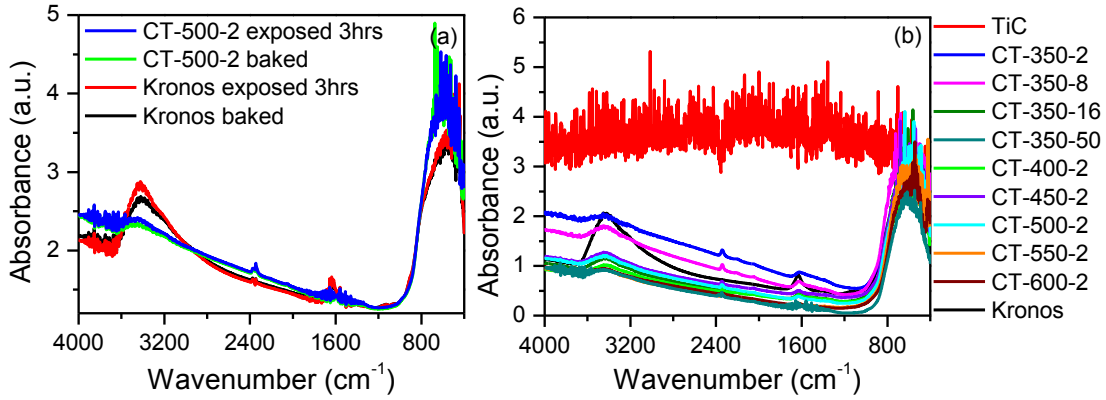

Figure 3-10. FTIR absorption spectra for (a) CT-500-2 and Kronos C-TiO_2 with/without baking and (b) all the C-TiO_2 samples.

As shown in Figure 3-10, the broad IR absorption centered at ca. 3427 cm^{-1} arises from the superposition of the υ_{OH} mode of interacting hydroxyl groups and the symmetric and antisymmetric υ_{OH} modes of molecular water coordinated to Ti^{4+} sites [105, 106] while the peak centered at ca. 1630 cm^{-1} is attributed to the bending mode of the physisorbed water [105, 107]. These two peaks corresponding to the

stretching vibrations of water or hydroxyl groups remained virtually the same in all the synthesized C-TiO_2 yet appeared much broader and stronger in the commercial C-TiO_2 Kronos vlp 7000, regardless of whether they were freshly baked or have been exposed in air for 3 hours (Figure 3-10(a)). These surface groups can serve as hole trapping sites to generate hydroxyl radicals with strong oxidation power and effectively suppress electron-hole recombination, thus enhancing the photocatalytic efficiency. The higher hydrophilicity with Kronos C-TiO_2 can be attributed to its extremely high BET surface area of ca. 300 m^2/g, which can provide more active sites for attachment of hydroxyl groups.

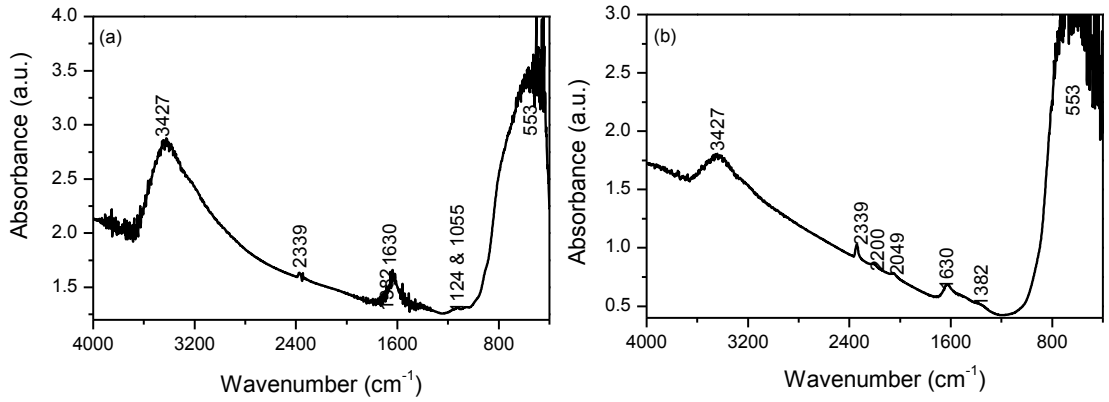

Figure 3-11. FTIR spectra for (a) Kronos C-TiO_2 and (b) CT-350-8 with peak assignment.

As shown in Figure 3-11, besides these two strong peaks associated with the hydroxyl groups, there was also a broad absorption band at 553 cm^{-1} and a small peaks at 1382 cm^{-1} appearing in all the samples, which could be attributed to Ti-O-Ti bonds vibration [108, 109] and carboxylate species [92] , respectively. For Kronos C-

TiO_2, there are two additional weak peaks appearing at 1124 cm^{-1} and 1055 cm^{-1} (Figure 3-11(a)), which could be ascribed to the vibration of Ti-O-C bonds to form carbonate species, suggesting the substitution of titanium by carbon atoms [110, 111]. The peak at ca. 2339 cm^{-1} was assigned to the υ(CO) mode of adsorbed CO_2, which could be due to slight change in ambient environment [107] or a likely intermediate in the formation of surface carbonate and bicarbonate species [112]. For the synthesized C-TiO_2 by thermal oxidation of TiC (Figure 3-11(b)), the peaks centered at 2200 cm^{-1} and 2049 cm^{-1} could be ascribed to stretching vibration of graphitic-like carbon due to carbon diffusion, which can be correlated with the Raman analysis. Careful examination (Figure 3-12) revealed that these two peaks diminished with increasing oxidation time and temperature, eventually faded away in sample CT-550-2 and CT-600-2, possibly due to complete oxidation of carbon species to gaseous CO_2.

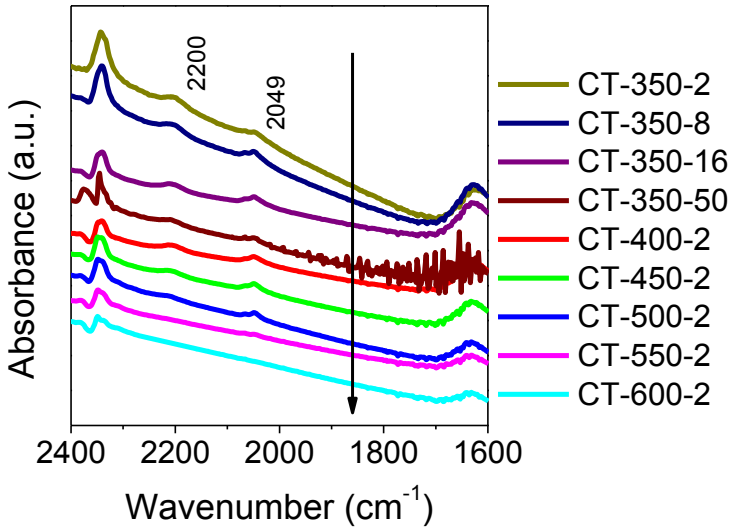

Figure 3-12. FTIR peak fading at 2200 cm^{-1} and 2049 cm^{-1} in C-TiO_2 samples.

Besides the surface hydrophilicity and chemical bonding analysis, it is interesting to observe the appearance of Ti-O-Ti bond vibration in TiC after exposure in air for 3 hours (Figure 3-13), signifying the native oxide formation. Further exposure in air up to 9 hours did not promote the further conversion from TiC to TiO_2, suggesting that such conversion may appear only at the sample surface.

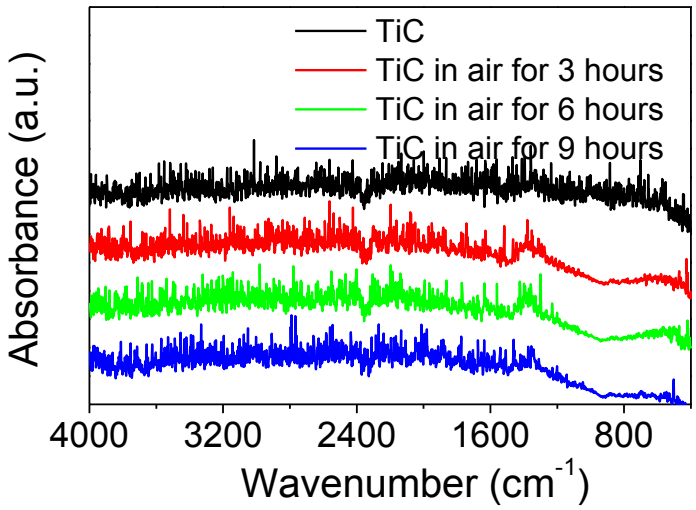

Figure 3-13. FTIR absorption spectra for pristine TiC before and after exposure to air.

In summary, FTIR analysis reveals the lower hydrophilicity with the synthesized C-TiO_2 as compared to the commercial Kronos C-TiO_2, possibly due to its lower BET surface area with less surface active sites. In the synthesized C-TiO_2 by thermal oxidation of TiC, the presence of carboxylate species at ca. 1382 cm^{-1} indicates the successful incorporation of carbon into TiO_2 lattice. Graphitic bonds were found fading away with increasing oxidation time or temperature, indicative of carbon diffusion and oxidation, supporting the previous Raman analysis. It is also noted that

the pristine TiC is prone to surface oxidation to form native oxide in ambient environment.

3.2.3.2 Chemical States Analysis

Chemical states and valence band analysis of the synthesized C-TiO_2 nanoparticles were performed with X-ray photoelectron spectrometer (XPS, Axis-Ultra, Kratos) equipped with monochromatic Al Kα X-ray source (KE = 1486.6 eV, 15 kV, 150W). Ar^+ ion sputtering at 4 kV for 6 minutes on 4 mm × 4 mm area was used to remove the surface oxide to unveil subsurface information for comparison. All XPS spectra were referenced to the C1s peak of adventitious hydrocarbon contamination located at 284.8 eV to correct the charging effect. Peak fitting of the XPS data was accomplished with a Shirley-type background subtraction using the spectra deconvolution software CasaXPS. Survey scan in Figure 3-14 confirms that the main elements on the surface of all the samples are titanium, oxygen and carbon only.

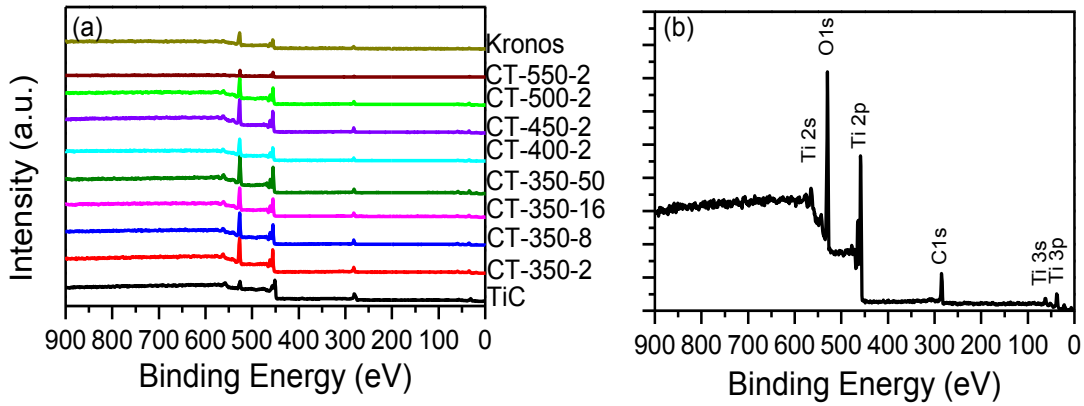

Figure 3-14. XPS survey spectra for (a) all the samples and (b) CT-500-2.

Figure 3-15 shows the core level XPS spectra for Ti 2p, C 1s, and O 1s before Ar^+ sputtering and Table 3-3 tabulates the core-level binding energy and atomic concentration information for all the samples in details.

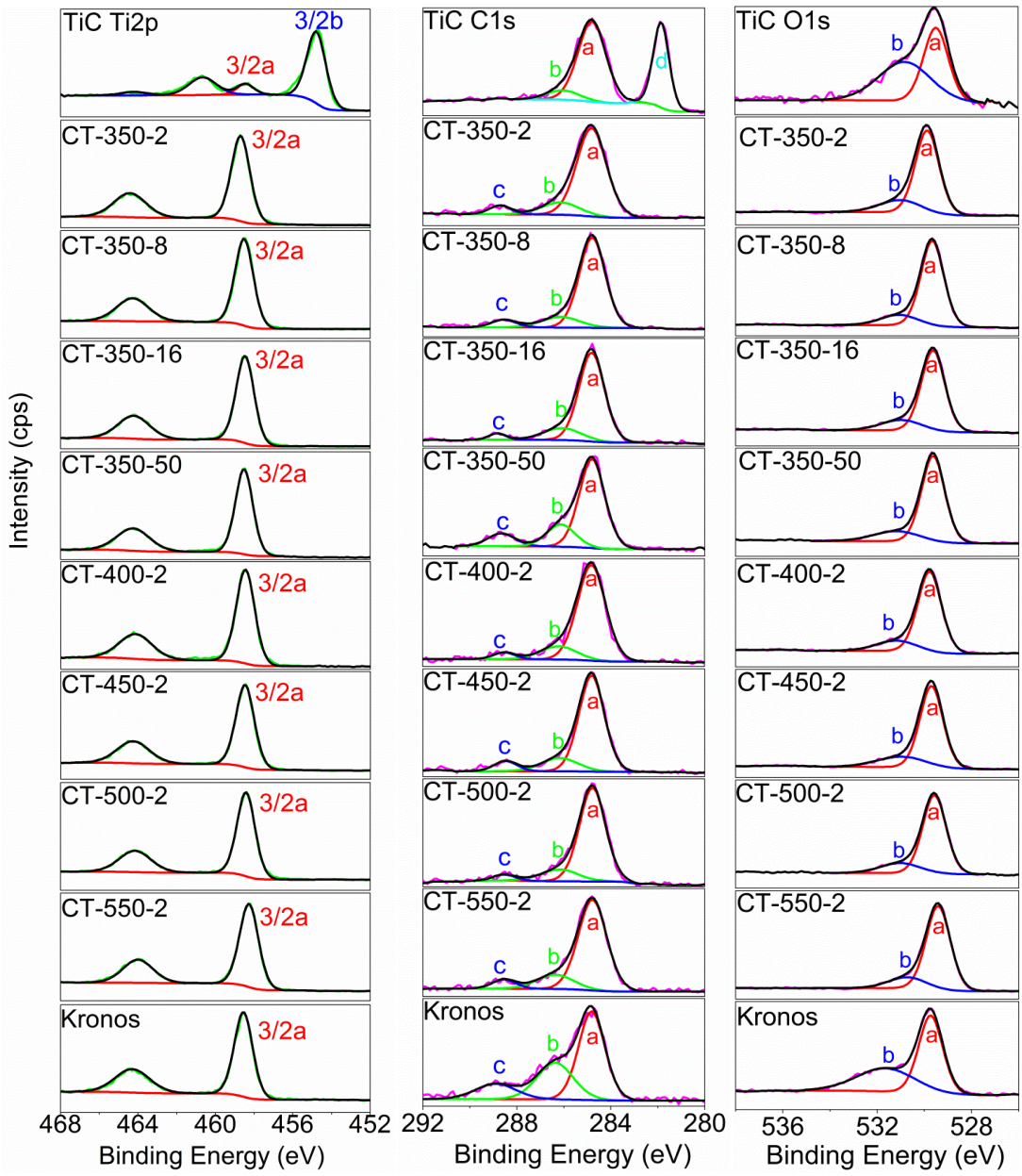

Figure 3-15. Core level XPS spectra for Ti 2p, C 1s and O 1s.

Table 3-3. Core-level binding energy and at% information.

Peaks		Ti 2p				C 1s				O 1s	
Label		3/2a	1/2 a	3/2b	1/2 b	a	b	c	d	a	b
BE (eV)		458.5	464.2	454.7	460.4	284.8	286.2	288.8	281.9	529.5	531.0
Peak assignment		TiO_2	TiO_2	TiC	TiC	C-H	C-O	C=O	TiC	O^{2-}	CO_3
TiC	BE	458.5	464.2	454.7	460.8	284.8	286.3	-	281.9	529.5	530.8
	at.%	2.5	0.98	13.82	4.99	35.47	4.06	-	20.59	8.41	9.19
CT-350-2	BE	458.7	464.4	-	-	284.8	286.1	288.7	-	529.9	531.0
	at.%	13.66	6.65	-	-	25.46	4.53	1.87	-	37.95	9.88
CT-350-8	BE	458.5	464.3	-	-	284.8	286.1	288.7	-	529.7	531.1
	at.%	14.43	6.69	-	-	22.52	3.95	2.03	-	42.14	8.23
CT-350-16	BE	458.5	464.3	-	-	284.8	286.1	288.9	-	529.7	531.0
	at.%	14.45	6.68	-	-	21.91	4.46	1.05	-	42.26	9.18
CT-350-50	BE	458.5	464.2	-	-	284.8	286.1	288.7	-	529.6	531.2
	at.%	14.86	7.403			16.23	4.546	2.632		44.27	10.06
CT-400-2	BE	458.4	464.1	-	-	284.8	286.2	288.7	-	529.8	531.2
	at.%	17.38	7.9	-	-	9.29	1.75	0.52	-	52.08	11.07
CT-450-2	BE	458.5	464.2	-	-	284.8	286.1	288.7	-	529.7	530.9
	at.%	13.99	6.64	-	-	22.82	4.05	2.61	-	39.22	10.67
CT-500-2	BE	458.4	464.2	-	-	284.8	286.2	288.7	-	529.6	530.9
	at.%	14.72	6.63	-	-	19.82	4.7	1.51	-	44.51	8.1
CT-550-2	BE	458.3	464.0	-	-	284.8	286.4	288.6	-	529.4	530.7
	at.%	14.68	6.51	-	-	21.11	4.35	1.77	-	42.82	8.78
Kronos	BE	458.6	464.3	-	-	284.8	286.3	288.8	-	529.7	531.7
	at.%	10.41	5.44	-	-	18.87	10.47	4.57	-	29.32	20.92

The Ti 2p spin-orbital splitting pair for the pristine TiC should appear at ca. 454.7 eV (2p3/2 b) and 460.4 eV (2p1/2 b) with peak separation of 5.7 eV. However, in the TiC sample, an additional pair of spin-orbital splitting peaks were observed at 458.5eV (2p3/2 a) and 464.2 eV (2p1/2 a), which accounts for 16 ca.% of the total Ti 2p. They are assigned to the formation of TiO_2 [64] due to the surface oxidation of TiC in ambient environment as supported by the FTIR analysis. For all the C-TiO_2 samples, including the commercial C-TiO_2 Kronos vlp 7000, only a pair of symmetric Ti 2p peaks resulting from TiO_2 were observed.

The major carbon peak at 284.8 eV (C 1s a) for all the samples was due to physically absorbed hydrocarbon contaminations and might overlap with the graphitic-like C-C bonding (285.0 eV) as evident in Raman and FTIR analysis. In the TiC sample, the peak at ca. 286.2 eV (C 1s b) can be attributed to C-O bond [64], probably associated with weakly adsorbed surface species while the peak suited at ca. 281.9 eV (C 1s d) corresponds to the Ti-C bond [67]. In the C-TiO_2 samples, besides the peak at 286.2 eV (C 1s b), an additional peak at 288.5-288.8 eV (C 1s c) was observed, which could be ascribed to C=O bonds. The concurrent presence of C–O and C=O bonds could indicate the formation of carbonate-like species due to interstitial of carbon into TiO_2 lattice [113] .

In all the samples, an intense peak is observed at around 529.5 eV (O 1s a) in the O 1s spectra, which could be attributed to the O^{2-} anions of the crystalline network, suggesting that the chemical state of oxygen is main lattice oxygen in TiO_2. The atomic ratio between O 1s a and the associated Ti 2p a falls in the range of 1.9 to 2.1 for the C-TiO_2. For all the samples, there was another relatively lower peak at ca. 531.0 eV (O 1s b), possibly due to weakly adsorbed surface species such as surface hydroxyl group (O-H) [64] or could be linked to C 1s b and C 1s c ascribed to the carbonate-like species. P. Zabek, et al. have also assigned this peak to coordinated carboxylate group in Kronos C-TiO_2 [61].

Surface oxidation, hydroxylation and/or carbonation phenomena have brought difficulties in obtaining reliable C 1s data pertaining to the surface sensitivity of XPS only up to top 1-10 nm of the sample surface. Other bonds could exist in the subsurface covered by the native oxide or carbonate species. Therefore, Ar^+ was used

to remove the surface oxide for all the samples to reveal more comprehensive and conclusive information as shown in Figure 3-16 and

Table 3-4.

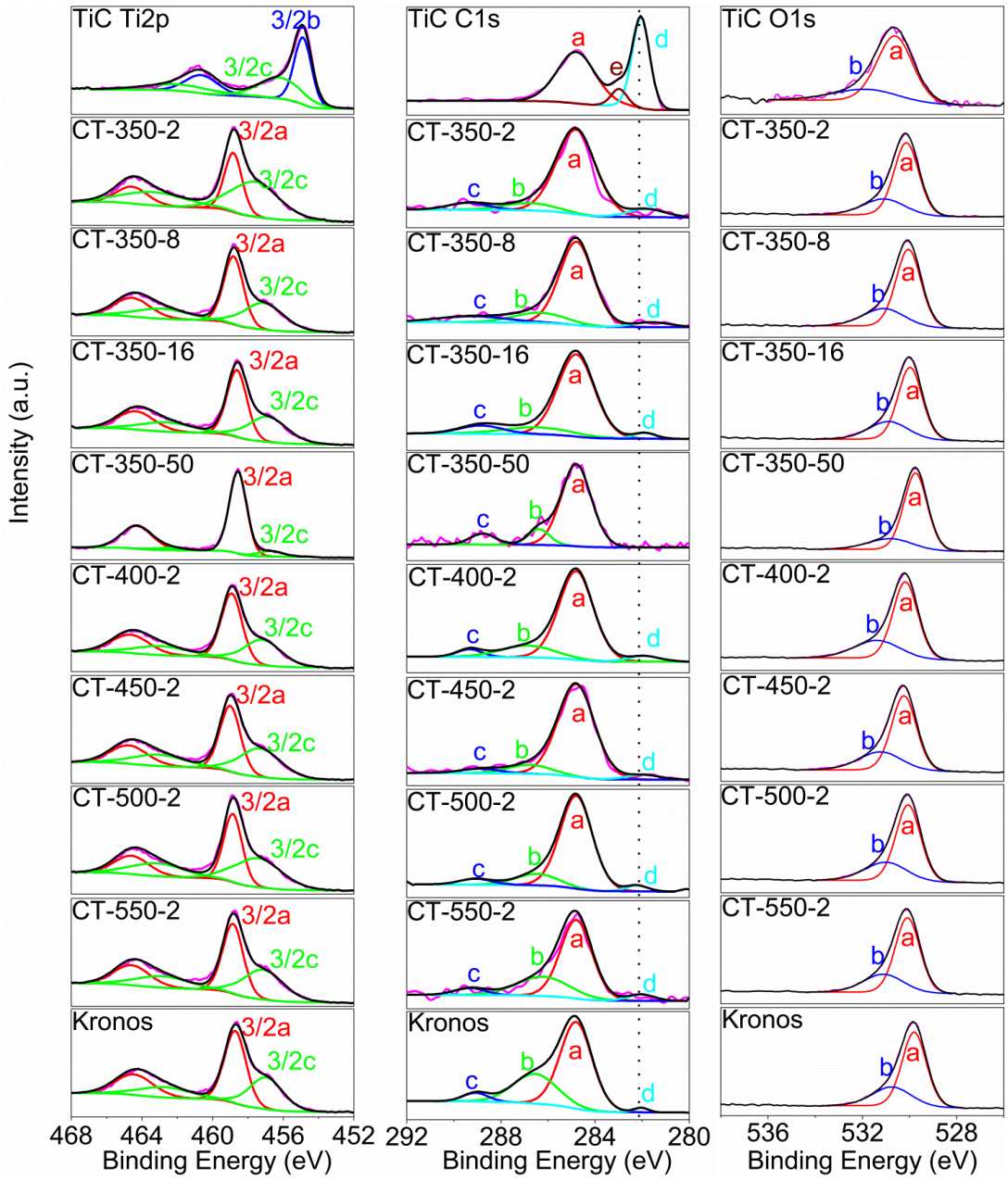

Figure 3-16. Core level XPS spectra for Ti 2p, C 1s and O 1s after Ar^+ sputtering.

Table 3-4. Core-level binding energy and at% information after Ar^+ sputtering.

Peaks		**Ti 2p**				**C 1s**				**O 1s**	
Label		3/2a	1/2 a	3/2c	1/2c	a	b	c	d	a	b
BE (eV)		458.5	464.2	457.0	462.7	284.8	286.2	288.8	281.9	529.5	531.0
Peak assignment		TiO_2	TiO_2	Ti_2O_3	Ti_2O_3	C-H	C-O	C=O	Ti-C	O^{2-}	CO_3
CT-350-2	BE	458.9	464.6	457.6	463.4	284.8	286.8	289.4	281.8	530.2	531.1
	at.%	7.182	3.578	11.41	5.686	9.267	1.069	0.775	0.856	43.73	16.44
CT-350-8	BE	458.8	464.5	457.1	462.8	284.8	286.4	289.2	281.8	530.0	531.1
	at.%	10.14	5.053	8.091	4.031	7.827	1.46	1.15	0.515	44.62	17.1
CT-350-16	BE	458.6	464.3	456.9	462.6	284.8	286.5	288.8	281.9	530.0	530.9
	at.%	10.82	5.389	7.99	3.981	7.95	1.288	0.946	0.337	43.65	17.65
CT-350-50	BE	458.6	464.3	456.7	462.5	284.8	286.4	288.8	-	529.7	530.8
	at.%	15.27	7.605	1.421	0.708	13.19	1.811	1.51	-	46.1	12.38
CT-400-2	BE	458.9	464.6	457.2	462.9	284.8	286.9	289.8	281.9	530.2	531.4
	at.%	10.51	5.234	7.242	3.608	8.523	1.769	0.447	0.675	43.4	18.59
CT-450-2	BE	459.0	464.7	457.3	463.0	284.8	286.8	288.9	281.9	530.2	531.2
	at.%	9.887	4.926	8.645	4.307	10.14	1.132	0.525	0.484	42.12	17.84
CT-500-2	BE	458.9	464.6	457.4	463.1	284.8	286.5	289.1	282.2	530.1	531.0
	at.%	9.071	4.519	9.745	4.855	8.599	1.376	0.545	0.387	43.19	17.72
CT-550-2	BE	458.8	464.5	457.1	462.8	284.8	286.2	289.3	282.0	530.0	531.0
	at.%	10.29	5.125	8.642	4.305	6.318	2.603	0.555	0.435	44.27	17.46
Kronos	BE	458.7	464.4	457.0	462.7	284.8	286.6	289.0	282.0	530.0	531.5
	at.%	8.917	4.442	6.166	3.072	9.267	3.969	0.721	0.369	38.77	24.31

In the TiC sample, the Ti 2p doublet due to Ti^{4+} in TiO_2 was replaced by a new pair of spin orbit splitting peaks at ca. 456.1 eV and 461.9 eV, ascribed to an intermediate state between Ti^{2+} and Ti^{3+} [114] induced by ion etching. The corresponding O 1s peaks were also shifted towards higher binding energy at 530.6eV (O 1s a) due to formation of intermediate state between O^- and O^{2-}. In its core level C 1s spectra, a third peak (C 1s e) at ca. 283.0 eV has been observed in addition to the Ti-C and C-C

peak, attributed to an additional bonding state in the carbide/matrix interface promoted by prolonged ion etching [99].

In all the C-TiO_2 samples, the contribution to the Ti 2p spectra due to TiO_2 decreased while contribution due to Ti_2O_3 appears at ca. 457.0 eV and 462.7 eV, again induced by the ion sputtering. It is noteworthy that the peak intensities and atomic concentration of the carbon and carbonate species decreased significantly after Ar^+ sputtering, suggesting the preferential covering of graphite-like carbon and carbonate species on the surface of C-TiO_2. The C 1s c peak at ca. 281.9 eV ascribed to Ti-C bond was observed after Ar^+ sputtering, suggesting the successful substitution of carbon for the oxygen atom in the lattice of TiO_2, which was previously covered by the surface-enriched carbonaceous species. The carbonate content increased with prolonged oxidation at elevated temperature, possibly due to the carbon diffusion to sample surface to a greater extent.

The O 1s b peak at ca. 531.0 eV was previously attributed to either weakly adsorbed surface species or the carbonate-like species. It was noted that its atomic concentration was increased instead of reduced after sputtering, unlikely ascribed to weakly absorbed species such as hydroxyl groups or water. Thus, it is more reasonable to assign O 1s b to carbonate-like species which can be linked to C 1s b and C 1s c.

Carbon doping of TiO_2 should lead to an increase of the density of states (DOS) just above the TiO_2 valence band edge to enhance the visible-light absorption [115].

Direct evidence on the modification of the TiO_2 valence band by carbon doping was obtained via valence band XPS scan as shown in Figure 3-17. An increase of the DOS above the TiO_2 valence band edge was unveiled due to the contribution of C 2p orbitals [55]. The increase was more obvious after sputtering, suggesting the substitutional carbon instead of interstitial carbon introduces more states near the VB edge of TiO_2, consistent with the theoretical calculation by Di Valentin et al. [116].

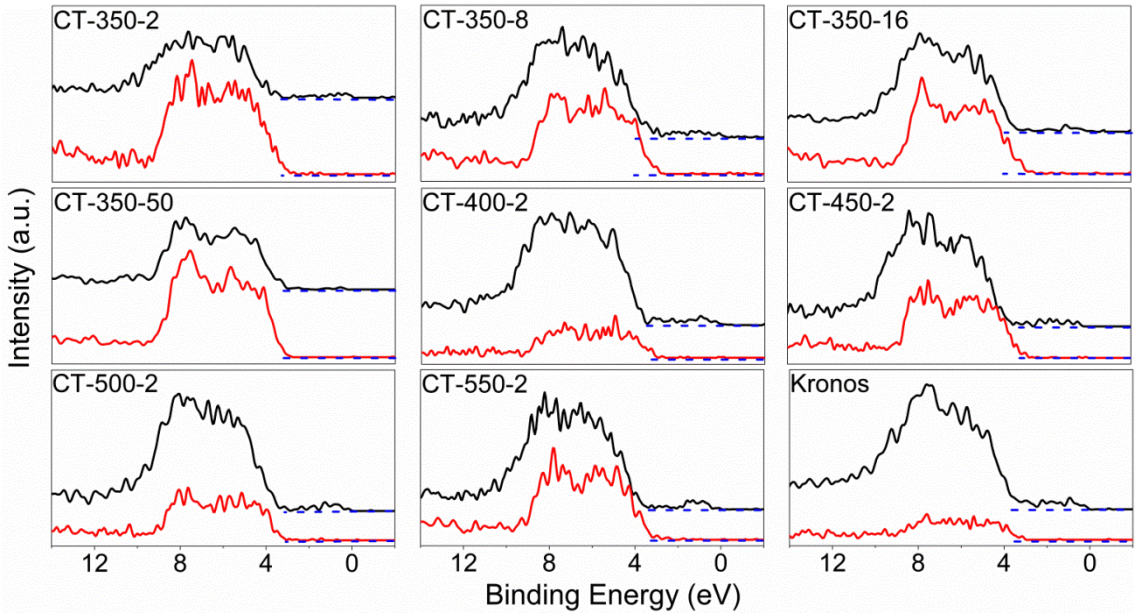

Figure 3-17. Valence band XPS spectra for C-TiO_2 (red: before sputtering; black: after sputtering).

In summary, simultaneous presence of substitutional carbon and intestinal carbon was revealed by XPS analysis to collectively enhance the visible light absorption of TiO_2. The substitutional carbon at oxygen sites introduces additional C 2p states above the O 2p band to effectively narrow the bandgap of TiO_2, which is evident by the valence band scan. The interstitial carbon forms carbonate species preferentially

covering the sample surface to serve as photosensitizer to induce visible light absorption. Graphitic carbon should also cover on the TiO_2 surface to serve as photosensitizer similar to carbonate species, as revealed by the Raman and FTIR analysis. However, its presence may be masked by the major hydrocarbon contamination peak with similar binding energy in the XPS analysis.

3.2.4 Optical Study

3.2.4.1 UV-Vis Absorption Spectra

Diffuse reflectance spectra were recorded in the range of 240-800 nm in reference to barium sulphate ($BaSO_4$) using a UV-Vis spectrometer (UV-2450, Shimadzu) fitted with a multipurpose sample compartment (MPC-2200, Shimadzu). A Kubelka-Munk (KM) transformation was done on the reflectance data to obtain the absorption spectra for red shift observation.

Figure 3-18(a) shows the optical absorption spectra of commercial TiO_2 powders. The rutile and antase TiO_2 exhibited a strong absorption near the UV range at 407 nm and 380 nm, corresponding to bandgap energy of 3.05 eV and 3.26 eV respectively, which is close to the reported values in literature [117]. Kronos vlp 7000 as a commercial visible light-driven C-TiO_2 was also studied as a reference. The fundamental absorption edge of 380 nm was similar to that of anatase phase, corresponding to bandgap energy of 3.26 eV, suggesting anatase as the main phase for Kronos. Additional red-shift was observed with absorption tail up to 600 nm,

possibly attributed to the substitution of C atoms at O sites or Ti sites [116] or due to the formation of carbonate species as revealed in FTIR and XPS analysis.

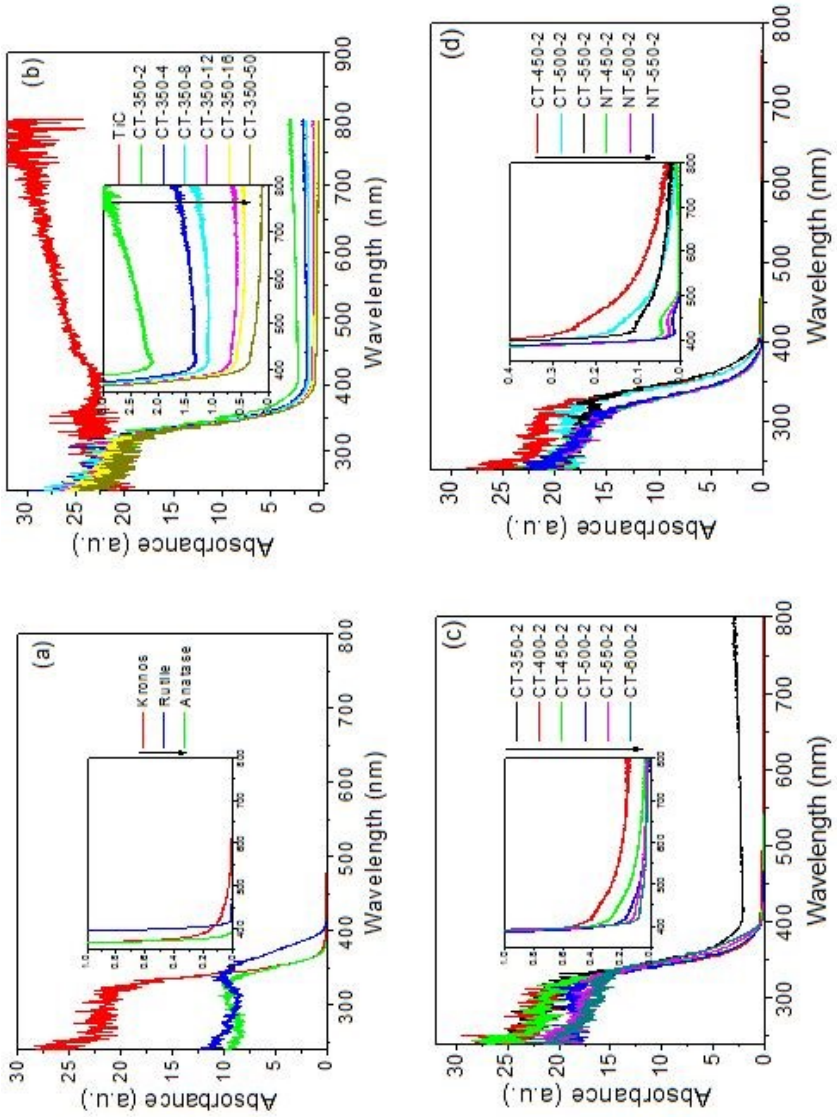

Figure 3-18. Optical absorption spectra with zoom in-view in the inset for (a) commercial TiO_2 powders, (b) C-TiO_2 synthesized at 350 °C for 2-50 hours, (c) C-TiO_2 synthesized at 350-600 °C for 2 hours, and (d) C-TiO_2 in comparison to N-TiO_2 synthesized at 450-550 °C for 2 hours by thermal oxidation of TiN.

The absorption spectra of pristine TiC and C-TiO_2 synthesized by mild oxidation at 350 °C for 2-50 hours are presented in Figure 3-18(b). The TiC precursor revealed no fundamental absorption edge characteristic as TiO_2. After thermal oxidation at 350 °C for 2 hours, the absorption edge starts to appear at around 400 nm, corresponding to the characteristic of rutile TiO_2. However, it should be noted that the absorption profile in the high wavelength range (450-800 nm) was still dominated by that of TiC with a characteristic drifting up tail for oxidation time up to 12 hours, indicative of the presence of unoxidized TiC which was not detected in XRD measurement except for CT-350-2, possibly due to the better sensitivity of UV-Vis diffuse reflectance technique. The absorption characteristic for TiC disappeared thereafter, suggesting the complete removal of TiC phase. For all the samples, the overall visible light absorbance intensities were enhanced with the absorption tail extending up to 800 nm, which can be attributed to the presence of graphite-like carbon and coexistence of substitutional and interstitial carbon in the TiO_2 to either narrow the band gap or serve as photosensitizer [94, 101, 118].

As compared to the mild oxidation at 350 °C with a long annealing time, the modification to the absorption characteristics was more immediate with more aggressive oxidation process at higher temperature of 400 °C – 600 °C for 2 hours as shown in Figure 3-18(c). No TiC but only TiO_2 absorption characteristic was observed for all samples, with an absorption tail extending to 800 nm in the visible light range. With the increasing oxidation temperature, more carbon species was oxidized, resulting in a decrease in absorption intensity in the visible light range. A comparison with N-TiO_2 synthesized by thermal oxidation of TiN at 450-550 °C for

2 hours (Figure 3-18(d)) revealed that the effect of carbon doping was more pronounced than nitrogen doping by producing larger valence band red shift, consistent with the theoretical calculation by Wang and Lewis [55].

In summary, TiC oxidized at different temperature (350-600 °C) for different time (2-16 hours) have all exhibited visible light absorption up to 800 nm due to the carbon doping in TiO_2. The absorbance decreased with increasing temperature or time due to the less carbon content retained in the lattice. The increasing oxidation temperature (350-600 ºC) has shown a more drastic modification on the characteristic absorption as compared to prolonged calcination time at lower temperature of 350 °C. As compared to N-TiO_2 synthesized at the same condition by thermal oxidation of TiN, the C-TiO_2 appeared to be more promising with larger valence band red shift.

3.2.4.2 Photoluminescence

Recombination of photogenerated electrons and holes in semiconductor photocatalyst often incurs low quantum efficiency to hinder its applications. Photoluminescence (PL) emission spectra resulting from the recombination of free carriers were recorded using a photoluminescence mapping system (Nanometrics RPM2000) equipped with a 325 nm He-Cd laser and a 345 nm LP filter to investigate the fate of charge carriers after photogeneration.

As shown in Figure 3-19, a broad peak centered at ca. 600 nm was observed in all the synthesized C-TiO_2 samples, which might originate from the non-integrality of the crystallite such as the lattice distortion or surface oxygen vacancies caused by carbon

doping [119]. Two small peaks near ca. 400 nm and 805 nm were also observed in all the samples. The former signal is ascribed to the emission of the band gap transition, with the main emission peak cut by the 345 nm LP filter, leaving with an emission tail. The latter near-infrared PL peak is possibly associated with the rutile structure [115]. The main peak at 600 nm can be observed to exhibit a stronger emission with prolonged oxidation time at 350 ºC or increased oxidation temperature up to 450 ºC, possibly due to the lattice distortion caused by carbon diffusion. With further increase in temperature up to 550 ºC, this peak was seen reduced, which could be attributed to the completion of carbon diffusion to the outer surface and recrystallization process.

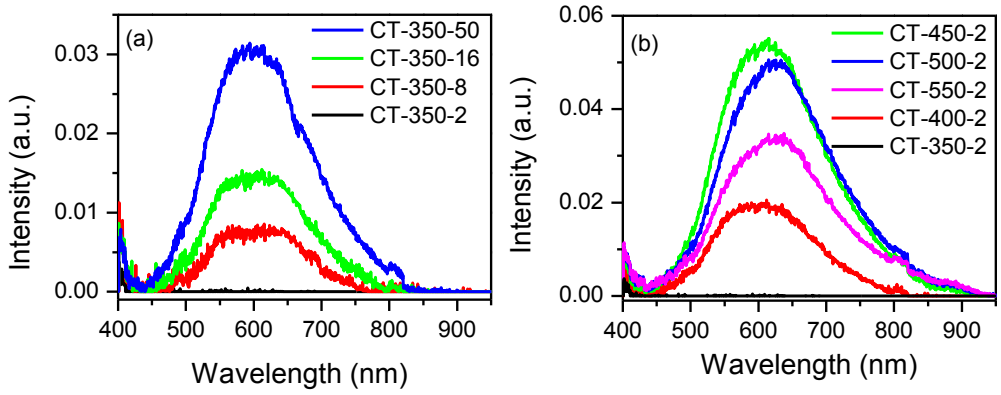

Figure 3-19. PL spectra of C-TiO_2 synthesized at (a) 350 ºC for 2-50 hours and (b) 350-600 ºC for 2 hours.

3.3 Proposed Band Structure and Visible Light Photocatalytic Mechanism of C-TiO_2

Based on the characterization of C-TiO_2, the possible band structure and visible light photocatalytic mechanism of the C-TiO_2 was proposed as shown in Figure 3-20. There are three possible pathways to generate active species for the degradation of attached organic pollutants under visible light irradiation. With these three pathways, a greater number of hydroxyl radicals are expected to be generated in C-TiO_2 to yield an improved visible light photocatalytic performance in comparison to pure TiO_2.

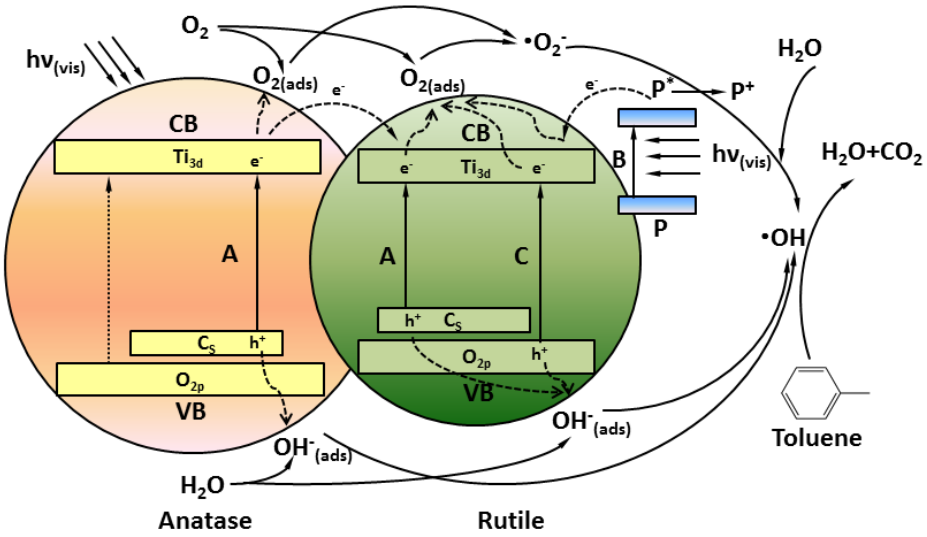

Figure 3-20. Proposed band structure of multi-type carbon-doped TiO_2 and visible light photocatalytic process.

Pathway A The substitutional carbon (C_s) at oxygen sites modifies the electronic band structure of TiO_2 by mixing C 2p orbitals with O 2p orbitals, resulting in band gap narrowing [120]. Upon visible light irradiation, electrons can be excited directly

into the TiO_2 conduction band and transferred to the adsorbed oxygen molecule ($O_{2(abs)}$) to produce $\cdot O_2^-$ and subsequently ·OH with strong oxidation power. Meanwhile, the photogenerated hole will oxidize the adsorbed water molecule (OH^-) to produce ·OH radical as well. The attached organic pollutants can thus be attacked by ·OH radical and be mineralized into CO_2 and H_2O after a series of reactions.

Pathway B The graphite-like carbon and carbonate species on the surface of TiO_2 can serve as photosensitizer (P) to absorb visible light and inject electrons into conduction band of TiO_2 [94, 118]. The injected electrons can be transferred to $O_{2(abs)}$ to trigger the subsequent red-ox reactions similar to pathway A. In addition to work as sensitizer, the graphite-like carbon can help to enhance the charge carrier separation by electron coupling of π states with the conduction band states of TiO_2 [101].

Pathway C Although rutile has a narrow band gap for some visible light absorption, its photocatalytic activity was reported to be low rate due to high recombination. Yet, the performance can be substantially improved to be comparable to anatase when charge recombination is inhibited by a photosensitizer [87]. In the C-TiO_2, both the coupling with anatase and carbonaceous sensitizer can help to enhance the charge separation to enhance the visible light photocatalytic activities.

3.4 Chapter Summary

C-TiO_2 nanoparticles with mixed anatase/rutile phases were successfully synthesized by conventional mild oxidation of TiC at 350 ºC for 2-50 hours and more aggressive

oxidation at higher temperature of 400-600 ºC for 2 hours in air. With prolonged oxidation time or increase in oxidation temperature, the rutile content remained virtually the same at ca. 30% with prolonged oxidation at 350 ºC for up to 50 hours or increased oxidation temperature up to 500 ºC for 2 hours, resembling the phase structure of the P25 TiO_2 powder with high photoactivity. Initial decrease in crystallite size and increase in specific surface area were unveiled due to cracking of TiC grains, renucleation of TiO_2 and diffusion of carbon atoms. Once recovery and recrystallisation were complete, grain growth was observed again to further reduce the internal energy. The carbon doping in the TiO_2 matrix was found to exist as graphite-like carbon, interstitial carbon in the form of carbonate species and substitutional carbon in the oxygen sites. The former two carbon states may serve as photosensitizers while the substitutional carbon narrows the band gap of TiO_2 by introducing additional electronic states just above the valence band, collectively enhancing the visible light photocatalytic activities. Three possible pathways for enhanced photocatalytic oxidation processes in C-TiO_2 nanoparticles were elucidated according to the proposed band structures.

CHAPTER 4 : VISIBLE LIGHT PHOTOCATALYTIC ACTIVITIES FOR ENVIRONMENTAL REMEDIATION

In this chapter, the visible light photocatalytic performance of the synthesized C-TiO_2 was evaluated for volatile organic compounds (VOC) removal and microorganism disinfection in comparison to commercial visible light-active C-TiO_2 Kronos vlp 7000 and N-TiO_2 synthesized with a similar recipe. The design and setup of the custom-built test system for VOC removal was first discussed in details, which enables the systematic evaluation of planar photocatalytic test pieces under both static and dynamic flow conditions with tunable light sources/intensity, feed pollutant concentration, humidity level, balancing gas and flow rates. The C-TiO_2 nanoparticles in coated form were evaluated for destruction of gaseous toluene as a probe VOC pollutant in this test system under different conditions. Then, we focused on the photocatalytic disinfection of Gram-negative *Escherichia coli* (*E. coli*) and Gram-positive *Enterococcus faecalis* (*E. faecalis*) with different cell wall structures in aqueous suspension under different light irradiation conditions (dark/Xenon+GG400 filters/Xenon+GG435 filters). The potential of utilizing the synthesized C-TiO_2 nanoparticles for actual environmental remediation was thus demonstrated.

4.1 Photocatalytic Destruction of Air-Bound Volatile Organic Compounds

4.1.1 Test System for Evaluating Photocatalytic Coating on Destruction of Air-Bound Volatile Organic Compounds

The feasibility of incorporating the C-TiO_2 coating in the air purification system will be examined in a custom built test system by studying the removal of the target gaseous pollutant. The design and setup of the test system followed the flow chart as shown in Figure 4-1.

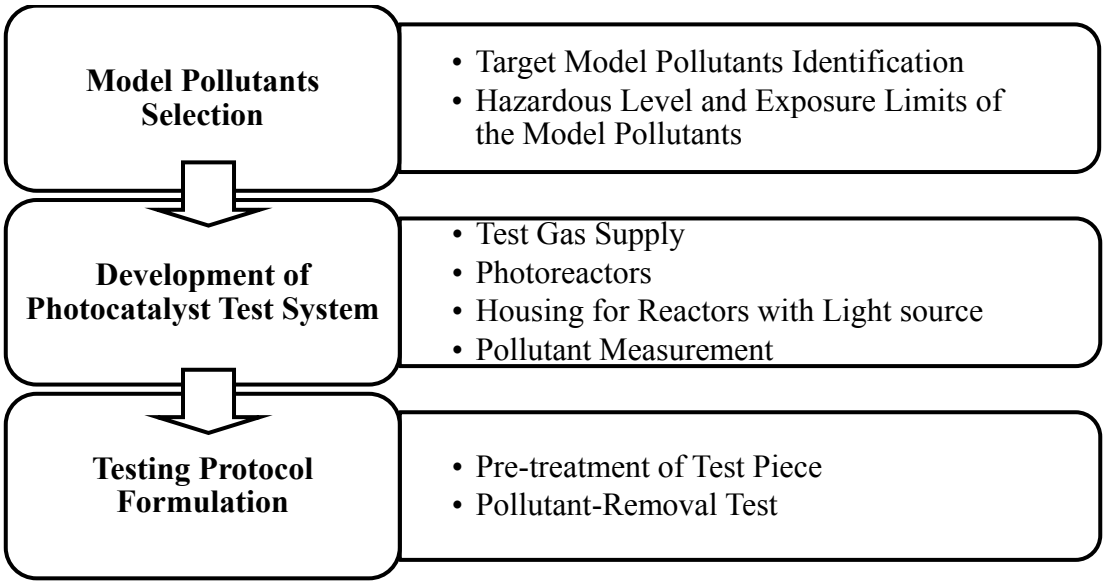

Figure 4-1. Flow chart for photocatalytic test system design.

Since the gas flow capacity and control of the test system will depend on the nature

of the feed model gases, the model pollutants have to be identified in the first place with the associated exposure standards studied to determine the test concentration. The test system can then be designed and set up by considering four main modules: test gas supply, photoreactors, housing for photoreactors with light source, and pollutant measurement. Finally, the testing protocol has to be developed by specifying the test piece pre-treatment method and the pollutant-removal test.

4.1.1.1 Model Pollutants Selection

Since photocatalytic technology is known to be able to degrade VOCs very efficiently, the air purification performance of the synthesized C-TiO_2 coating will be studied on selected pollutants from this category based on their ease of encountering and level of hazards, namely, isopropanol (IPA), benzene, and toluene. Their hazardous level and exposure standards are reviewed to determine the pollutant concentration in the photocatalytic test. It should be noted the photocatalytic test system is designed for but not only limited to these gaseous pollutants.

Health Hazards of the Target Air Pollutants

Isopropanol (IPA) is a clear liquid with a sharp and musty odour. It is a common component of many antiseptic and cosmetic products, including solvents, perfumes, cleaning agents, and components of pharmaceuticals. It is an irritant of the eyes and mucous membranes and may cause central nervous system depression at very high concentrations with poisoning symptoms including dizziness, incoordination, headache, and confusion [121].

Benzene is a colorless and highly flammable liquid with a sweet smell and a relatively high melting point. Indoor air generally contains levels of benzene higher than those in outdoor air, mainly from environmental tobacco smoke, stored paint supplies, and automobile emissions in attached garages. The short term breathing of low levels of benzene can cause drowsiness, dizziness, rapid heart rate, headaches, and unconsciousness while high levels can result in death. The major effects of benzene are chronic exposure that causes cancer [75, 122-125]. It can damage the bone marrow and cause a decrease in red blood cells, leading to anemia. It can also cause excessive bleeding and depress the immune system, increasing the chance of infection and causing blood cancer.

Because of the high hazardous level of benzene, toluene with similar solvent-properties is often used as a substitute of benzene in laboratory research [75, 126-129]. As compared to benzene, it is less toxic and has a wider liquid range. The indoor source of toluene usually comes from the use of common household products, printing, painting, and cigarette smoke [130]. Short term exposure to elevated level of toluene often causes central nervous system dysfunction and narcosis while chronic exposure also causes irritation of the upper respiratory tract and eyes, sore throat, dizziness, and headache [130].

Exposure Limits of the Target Air Pollutants

Due to the hazards associated with the selected pollutants, their exposure limits by the main environmental agencies are studied and summarized in Table 4-1. Among all these standards, National Institute for Occupational Safety and Health (NIOSH)

standard was chosen as a guideline in our photocatalytic study due to its comprehensiveness. The test concentration for the target model pollutants is selected in between the Immediately Dangerous to Life (IDLH) concentration and Time-Weighted Average (TWA) limits as shown in Table 4-1.

Table 4-1. Exposure limits and test concentration of the model pollutants, ppm [131].

Pollutant	NIOSH			OSHA			ACGIH		Test Concentration
	IDLH	TWA	ST	TWA	ST	C	TWA	ST	
Isopropanol (IPA)	2000	400	500	400	-	-	400	500	500
Benzene	500	0.1	1	1	5	-	0.5	2.5	10
Toluene	500	100	150	200	500	300	50	-	200

NIOSH: National Institute for Occupational Safety and Health

OSHA: Occupational Safety and Health Administration

ACGIH: American Conference of Governmental Industrial Hygienists

IDLH: Immediately Dangerous to Life or Health concentration for 30 minutes exposure

TWA: Time-Weighted Average concentration for up to a 10-hour workday during a 40-hour workweek

ST: Short-Term exposure limit for 15 minutes TWA unless stated otherwise

4.1.1.2 Development of the Photocatalytic Test System

The design and set up of the photocatalytic test system is based on the latest international standards for the characterization of photocatalyst (ISO 22197-1:2007 [132], JIS R 1701-2: 2008 [133] and JIS R 1701-3:2008 [134]) with modifications to fit in with the existing analytical instruments. The simplified illustration is depicted in

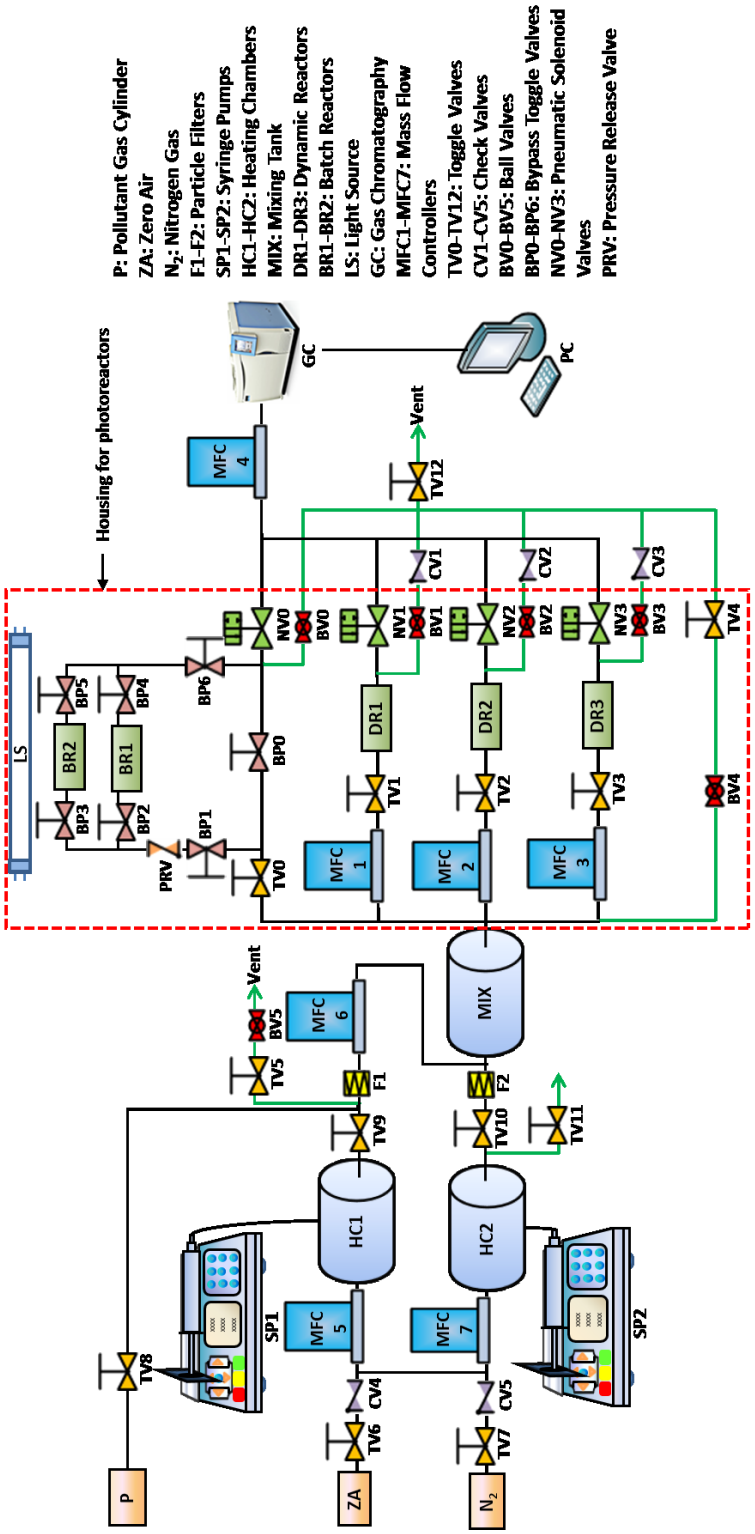

Figure 4-2. Test system design.

while the detailed specification of the system components is listed in Appendix A. In general, the test system will consist of a test gas supply, two batch photoreactors and

three dynamic photoreactors enabling the evaluation of photocatalytic test pieces under both static and continuous flow conditions, housing for the photoreactors with different light sources, and gas sampling and analysis configurations. The important considerations for each part will be discussed separately in the following section.

Test Gas Supply

In general, the pollutant gas is generated by evaporating the liquid source and brought into the photoreactors by the diluting air. Specifically, the pollutant in liquid form (>99%) in a stainless steel syringe (50 mL, KD Scientific) will be injected into a heating chamber (**HC1**) at a constant infusion rate as controlled by a syringe pump (**SP1**) and it will get vaporized at around 50 ºC. At the same time, compressed dry air (**CDA**) will go through a zero air gas generator (**ZAG**, ZA300, Peak Scientific Instrument) to produce a constant flow of Zero Grade Air with a hydrocarbon content (as Methane) of less than 0.1 ppm. The zero air will serve as both diluting and carrier gas for the vaporized pollutant to achieve a first stage dilution concentration of ca. 2000 ppm by setting the flow rate of the mass flow controller **MFC5**. The diluted pollutant gas will undergo second stage dilution by homogenizing with the humidified zero air in a mixing chamber (**MIX**) with a temperature/humidity/pressure probe. The final concentration of the pollutant in **MIX** will be controlled by **MFC6** and **MFC7** while the relative humidity of the gas stream is determined by the water infusion rate set by another syringe pump (**SP2**). The supply gas will then be supplied into the photoreactors (**PR1-PR3** or **BR1-BR2**) with different test pieces. Two sets of pressure release valves including toggle valves

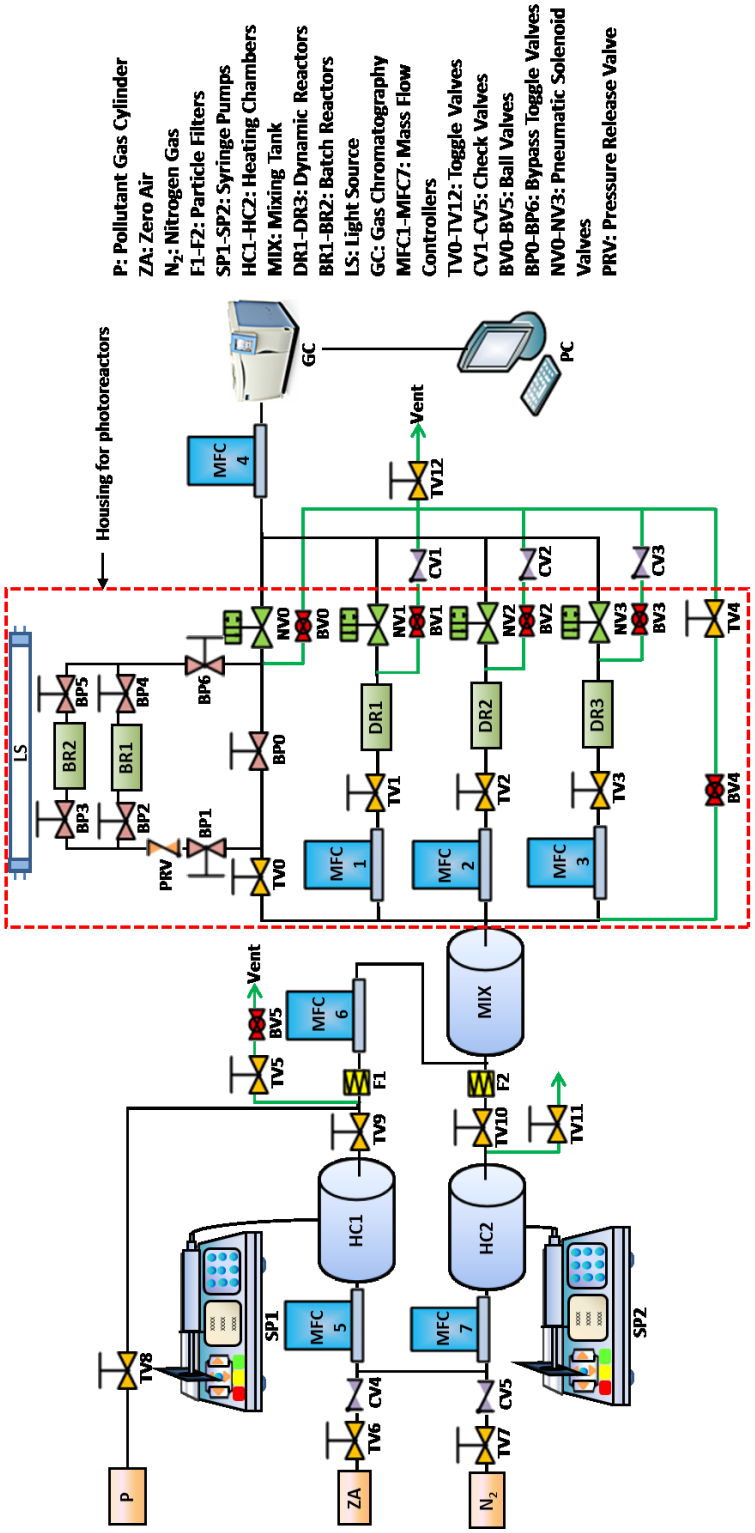

Figure 4-2. Test system design.

(**TV4 & TV5**) and ball valves (**BV4 & BV5**) will be used to establish a positive pressure to ensure the proper functioning of **MFC5** and **MFC6**.

Besides the **CDA** gas line, there is a **N_2** gas line to study the photocatalytic reaction in the absence of O_2. Pollutant cylinder (**P**) can also be connected to **TV8** for periodic calibration of the pollutant gas concentration. The flow rates for all the SPs and MFCs to produce the test pollutant concentration are listed in Table 4-2 with the detailed calculation method specified in Appendix B. Thus, the flow capacity of the mass flow controllers can be determined accordingly.

Table 4-2. Flow rate specification for syringe pumps and mass flow controllers.

Pollutant	**Physical Property**		**Flow Rate**							**Final Conc.**
	MW	Density g/mL	SP1 mL/hr	SP2 mL/hr	MFC1-MFC3 slm	MFC4 sccm	MFC5 slm	MFC6 slm	MFC7 slm	ppm
IPA	60.1	0.786	1.91	5.29	50-300	100	4.99	2.5	7.5	500
Benzene	78.1	0.8765	2.22	5.29	50-300	100	4.99	0.05	9.95	10
Toluene	92.1	0.8669	2.65	5.29	50-300	100	4.99	1	9	200

Photoreactors

The flexibility to choose from batch reactors and dynamic reactors will enable a more thorough understanding of the photocatalyst efficiency and mineralization pathway. Thus, two batch reactors (**BR1-BR2**) and three dynamic reactors (**DR1-DR3**) are designed in the photocatalyst test system to hold planar test samples coated with different photocatalysts for photocatalytic evaluation under static and

continuous flow conditions, respectively. The design of the photoreactors is depicted in Figure 4-3 and Figure 4-4.

As shown in Figure 4-3, the two batch reactors with internal dimension of 300 mm × 200 mm × 100 mm (L×W×H) are placed on an aluminum frame on top of the dynamic reactors. They can be easily dismantled from the system by disassembling the aluminum frame if dynamic flow tests are to be carried out. They are made of anodized aluminum for its low affinity to test gas and relatively light weight for easy disassembling. The reactor body is separated into two parts with two O-ring seals in between and the optical window is firmly attached to the upper part (**P1**). The test pieces can thus be replaced conveniently by removing **P1** without excessively stressing the optical window.

The three dynamic reactors are made of stainless steel for its low affinity to test gas and strong endurance against different light sources. As shown in Figure 4-4, the test piece of size 50 mm × 100 mm coated with different photocatalysts is placed onto a stainless steel adaptor fitted inside the reactor. The gap between the test piece and the optical window is kept at 5 mm. The gas stream enters the reactor from the sidewall into a tapered area to prevent turbulence. A baffle plate with an opening of height of 5 mm at the bottom is placed in front of and behind the adapter to provide a uniform flow channel for the gas steam. The adapter length is three times the length of the test piece to ensure a stable laminar flow. A plastic clamp and an O-ring seal are used between the optical window and the reactor to ensure proper sealing. A piece of UV-blocking filter can be placed on top of the optical window to cut-off the UV light portion from the light source for photocatalytic study under visible light.

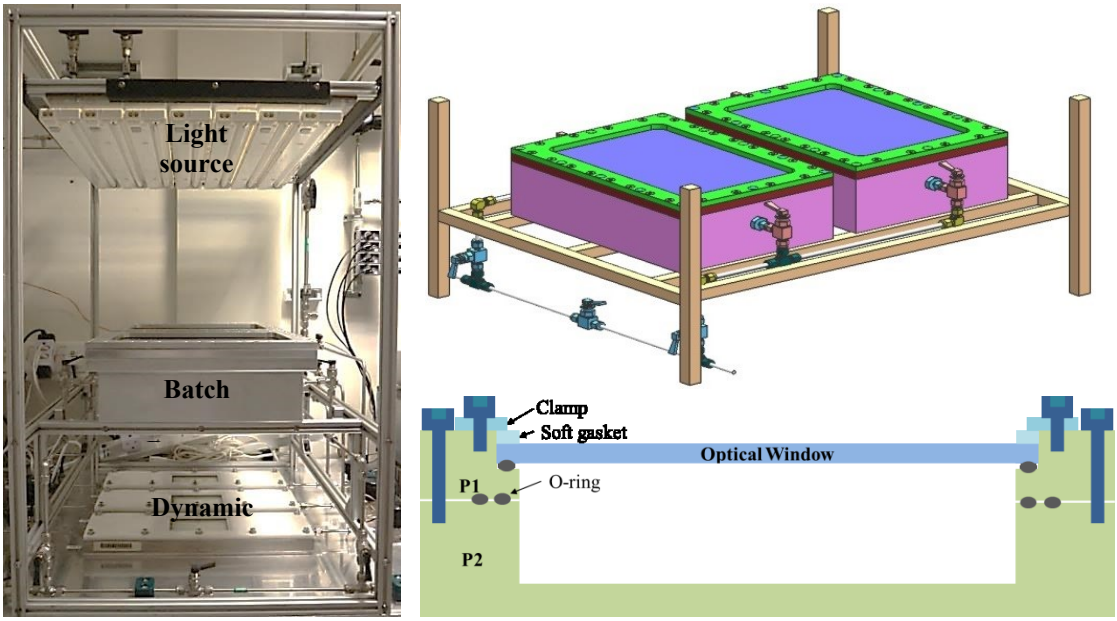

Figure 4-3. Overview of the photoreactors and design of the batch reactors.

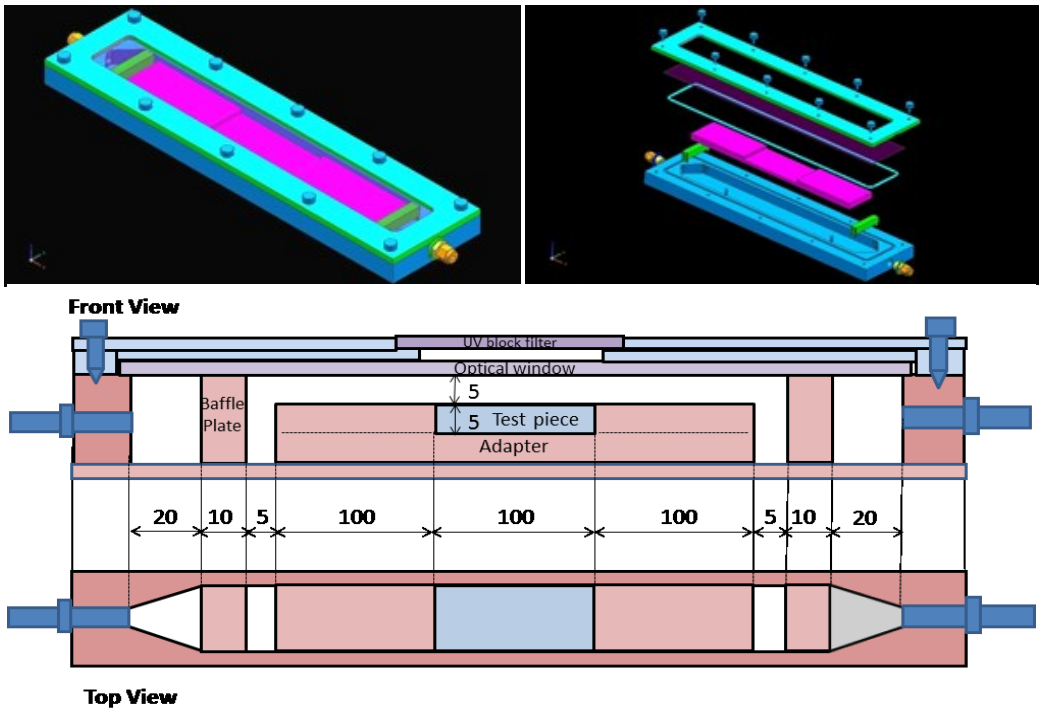

Figure 4-4. Design of the dynamic reactors.

Housing for Photoreactors with Light source

The housing of the photoreactors has been built with aluminum profile covered with thick cloth to cut out the ambient light as shown in Figure 4-3. The internal dimension of the housing is ca. 520 mm × 600 mm × 780 mm (L×W×H).

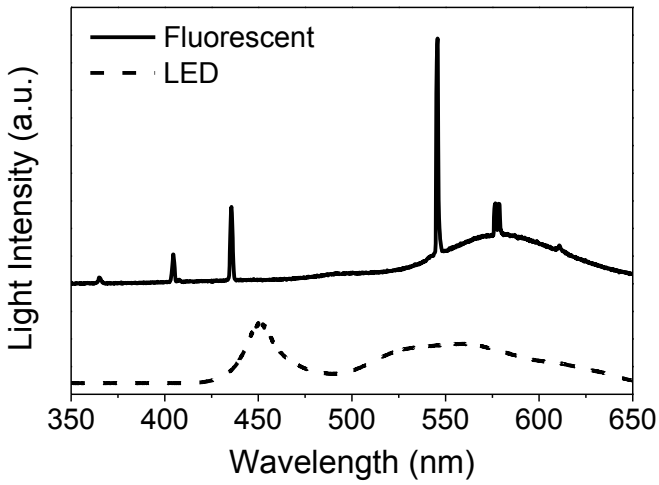

Figure 4-5. Measured emission spectra of fluorescent and LED light.

Seven pieces of cool daylight fluorescent lamp (6500K, 13W, OSRAM) and twenty pieces of T4 style LED strip light (5000K, 4.5W, Planetsaver) are used to compare the photocatalytic performance of C-TiO_2 under different light irradiation. The emission spectra for both light sources were measured using a portable UV-vis spectrometer (Ocean Optics, USB4000) as shown in Figure 4-5. Only visible light was detected under the LED irradiation with two broad emission peaks centered at ca. 450 nm and 560 nm, respectively. Under fluorescent light irradiation, a small emission peak in the UV range was detected on top of the five relatively strong peaks

in the visible light range. An optical filter (Melles Griot, GG400) was used to remove the UV peak when visible light-activated photocatalytic performance is of concern.

Gas Sampling and Analysis

The analyzer employed for the gas concentration measurement is a gas chromatography (**GC**, Clarus 600, Perkin Elmer) with flame ionization detectors (**FID**). The gas sampling configuration into the GC system is depicted in details in Figure 4-6 with the red frame part redrawn from the overall system design in

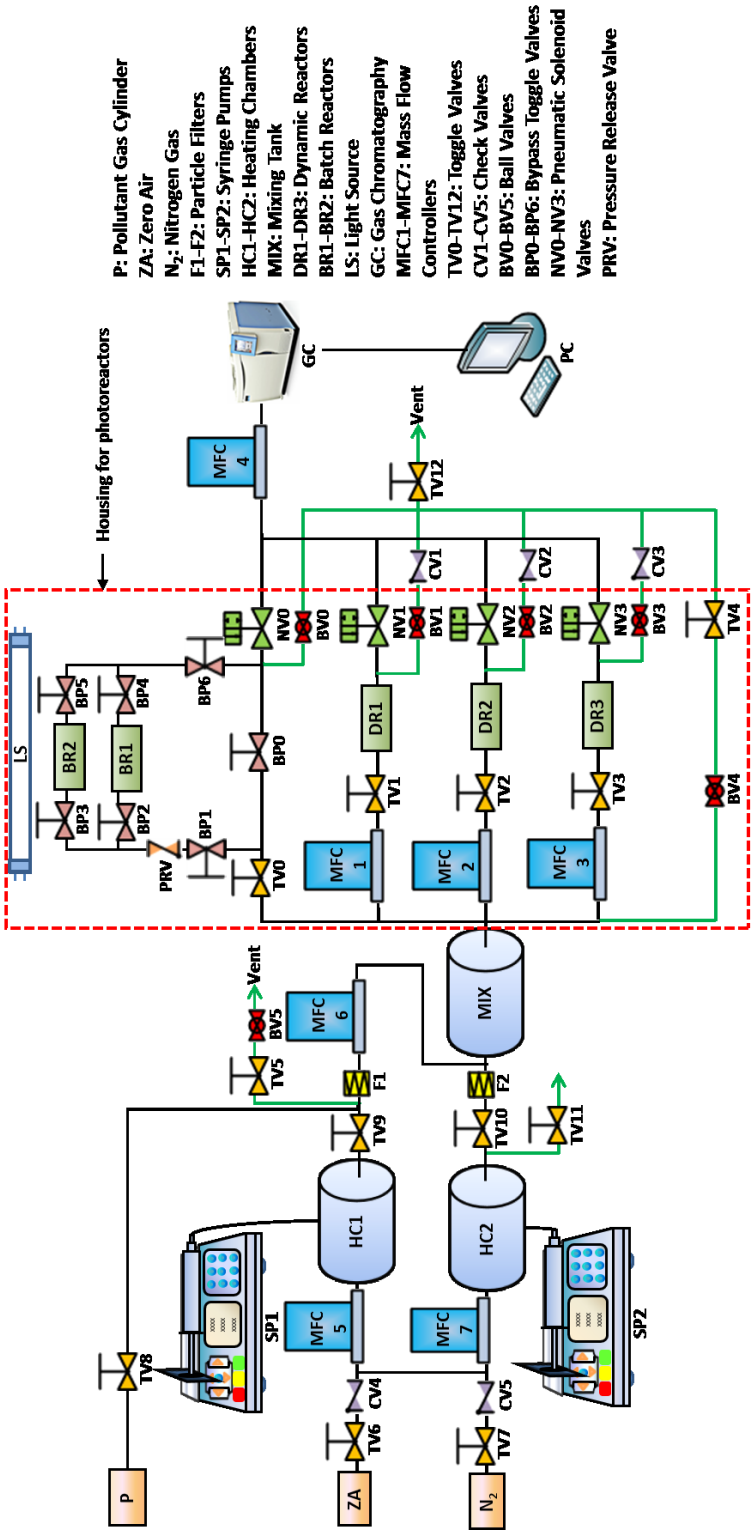

Figure 4-2. Test system design.

. The pre-programmed sampling sequence is first loaded into the relay control unit (**RCU**) attached to the GC equipment to sequentially activate the selected pneumatic

solenoid valve (**NV0-NV3**) by giving a 24V DC voltage. The gas stream from the inlet or photoreactors can then enter the GC system for sampling and analysis upon the switching on of the connected pneumatic solenoid valve. The sampling rate is controlled by **MFC4** at 100 sccm. Four ball valves (**BV0-BV3**) are used to release extra pressure for the proper functioning of **MFC4** while the three check valves (**CV1-CV3**) in connection with the dynamic reactors (**DR1-DR3**) are installed to prevent the breakage of optical windows due to back pressure.

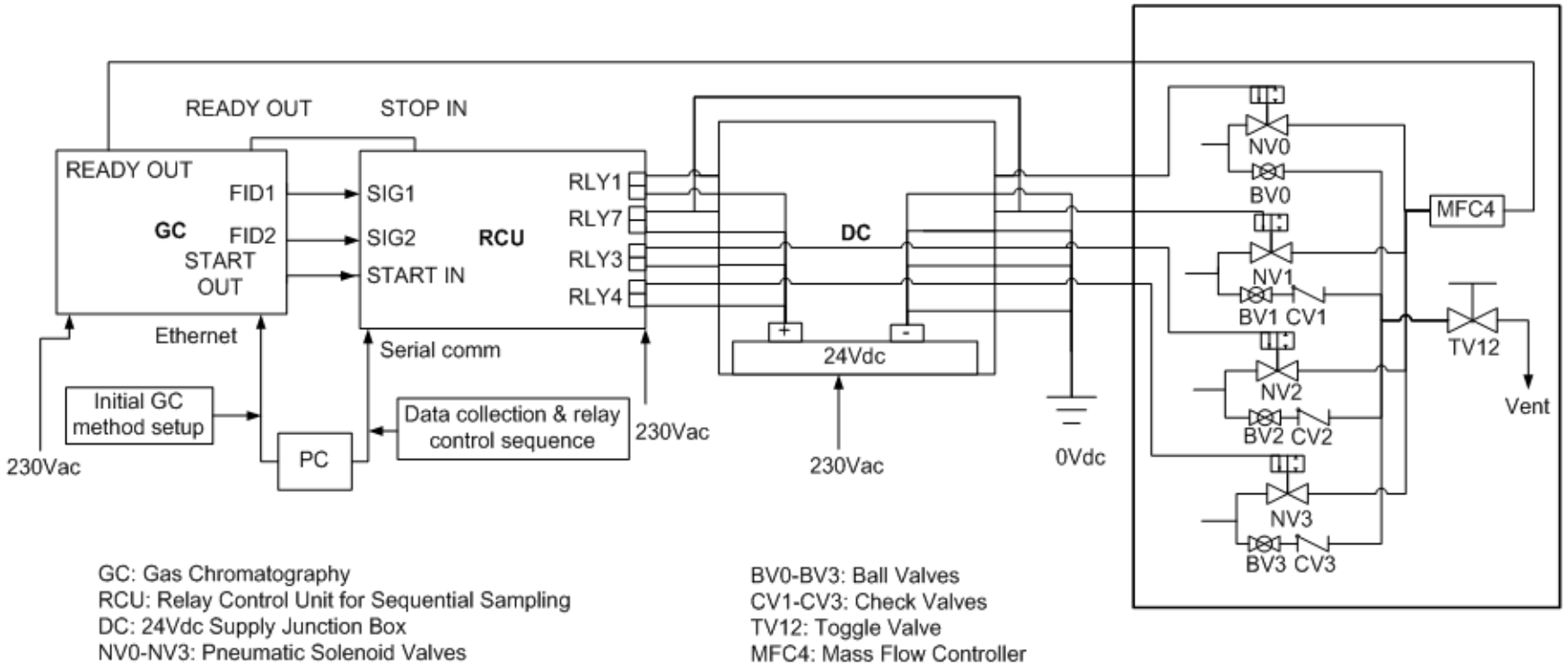

Figure 4-6. Gas sampling configuration into GC system.

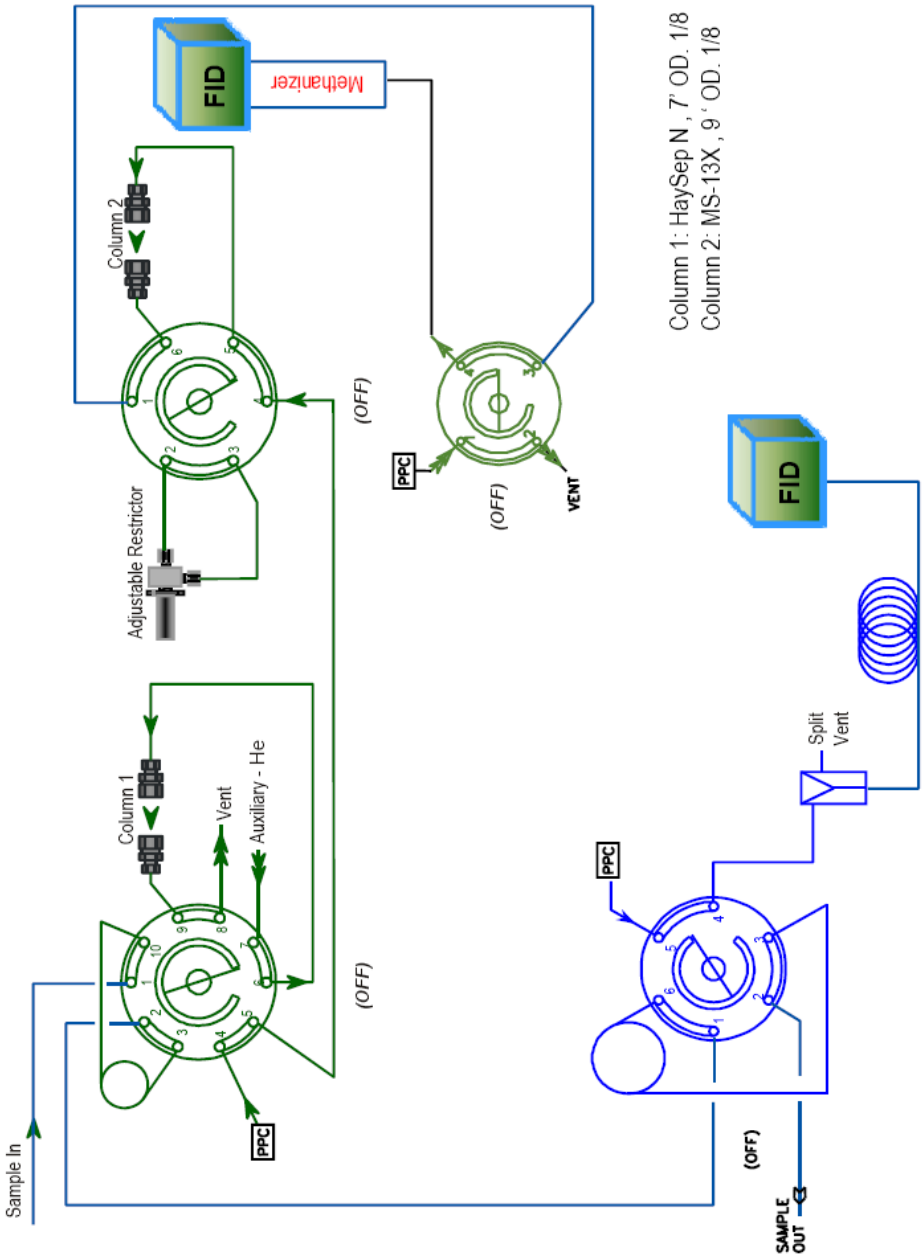

Figure 4-7. Gas quantification configuration in the GC system.

The gas quantification configuration for the customized GC system is depicted in Figure 4-7. The blue path is for measurement of target pollutant concentration. After entering the GC system, the selected gas stream will go through a 6-port sampling valve inside the oven for sample collection into the sampling loop, be diverted to a capillary column (ELITE-5, Perkin Elmer) for components separation of the gas mixture based on their interaction with the column and finally be detected by the FID for quantification purpose. The advantage of the 6-port valve as compared to the conventional sorbent tube for sampling lies in the better sampling volume control, higher collection efficiency as well as the elimination of use of expensive mass flow controller. Helium gas is used as the carrier gas for the capillary column while a hydrogen generator with a capacity of 100 sccm is used to supply the flame gas for the FID.

Besides the measurement of target pollutant concentration, CO_2/CO as the complete/incomplete mineralization products are also monitored using the green path as shown in Figure 4-7. Since FID is only efficient in detecting C-H bonding, a methanizer is used in conjunction with the FID to convert CO/CO_2 into methane (CH_4) for the quantification. The selected gas stream will first go through a 10-port valve for sampling. After the 10-port valve is switched, moisture will be flushed back and the sampled gas will enter Column 1 (HaySep, Perkin Elmer) for separation of CO/O_2 and CO_2. Since the subsequent 6-port valve will bypass the incoming gas stream through the adjustable restrictor once CO/O_2 arrives, CO_2 will emerge from Column 1 first and go through the 4-port valve, then the methanizer + FID for quantification. When the 6-port valve is switched again, the bypassed CO/O_2 stream

is able to go into Column 2 (MS-13X, Perkin Elmer) for separation of CO and O_2. CO will emerge before O_2 and be converted into methane for quantification. The remaining O_2 will be vented. With this configuration, CO_2/CO as the mineralization products can be successfully quantified to correlate with the pollutant degradation.

4.1.1.3 Development of Testing Protocol

The testing protocol for evaluating the air purification performance of the test pieces is established after the system setup. It should be noted that the testing protocol only applies when the adsorption time for the test piece is within 90 min.

Pre-treatment of Test Piece

The test pieces inside the photoreactors are subject to pretreatment before the actual tests. They should be irradiated with the light sources (fluorescent light or LED) under continuous flow of zero air in order to remove the adsorbed organic materials on the test pieces.

Pollutant-Removal Test

The evaluation of the photocatalytic test pieces on fixed volume of gaseous pollutants is carried out in the batch reactors with the following testing protocol:

a) Load the liquid pollutant and water into the 50mL stainless steel syringes and fix the syringes into the system;
b) Switch on the valves: TV0, TV4, TV5, TV9, TV10, TV12, BV0, and BV4;

c) Switch on MFC controllers and set the appropriate flow rates according to Table 4.2 for MFC4-MFC7 and adjust BV5 for MFC5 to function properly;

d) Switch on TV6 to supply zero air to purge the system;

e) Switch on the syringe pumps and set the appropriate infusion rate according to Table 4.2 to inject liquid pollutant and water into the heating chambers HC1 and HC2 respectively;

f) Turn on the wrapped heaters on the heating chambers and set the appropriate temperature (HC1: 60 °C, HC2: 80 °C) to vaporize the liquid pollutant and water and establish the desirable gaseous pollutant concentration and humidity level;

g) Switch off BP0 and switch on BP1-BP6 to let the gaseous pollutants flow through the batch reactors with test samples to establish adsorption-desorption equilibrium;

h) Check the water level and turn on the hydrogen generator to supply hydrogen to gas chromatography (GC) as flame gas;

i) Turn on the GC and switch on the helium gas cylinder to supply helium to the GC column as carrier gas;

j) Turn on the PC and load the pre-set test sequence to GC;

k) Ignite the GC detector from GC control panel and wait for the detector signal to stabilize for about 30 min;

l) Start the GC test sequence and monitor the pollutant concentration in the batch reactor;

m) Once the desirable concentration is reached, switch off BV4, BP4 and BP5 in order to charge the batch reactors BR1 and BR2 with the gaseous pollutants;

n) Once the pressure inside BR1 and BR2 reaches 18 psi on the analog pressure gauge, switch off BP1-BP3, and switch on BV4 to release the pressure inside the mixing chamber (MIX) and pipelines;
o) Switch on the light source to start the photocatalytic test and sample into GC periodically to examine the degradation of gaseous pollutants;
p) Stop the syringe pumps SP1 and SP2 and turn off the heaters on HC1 and HC2;
q) After the test, switch on BP4-BP6, and BV0 to release the pressure inside the batch reactors BR1 and BR2, switch on BP1 and BP3 and switch off BV4 to let the zero air to purge the batch reactors BR1 and BR2 for two hours to clean the photocatalytic test pieces;
r) Release the pressure in hydrogen generator and turn off it;
s) Cool down the detector and oven in GC and switch off GC and helium gas cylinder;
t) Turn off the PC and the light and switch off TV6 and mass flow controllers.

For the test under continuous flow of gaseous pollutants in the dynamic reactors, similar procedure was followed except for the following changes:

g) Switch "ON" TV1, TV2 and TV3 to let the gaseous pollutants flow through the dynamic reactors (DR1-DR3) with test samples to establish adsorption-desorption equilibrium;
l) Start the GC test sequence and monitor the pollutant concentration in the dynamic reactor;

m) Once the desirable concentration is reached, switch on the light on top of DR1-DR3 to start the photocatalytic test and monitor the gas concentration periodically;

n-o) omitted;

q) Purge the system with zero air for two hours.

4.1.2 Photocatalytic Destruction of Gaseous Toluene in Batch Reactors

With the successful setup of the photocatalytic test system, the photocatalytic performance of the synthesized C-TiO_2 was evaluated on the gaseous toluene in the batch reactors to determine its capability for volatile organic compounds removal. The photocatalytic coating was prepared by spraying 20 mL consisting 50 g/L of each photocatalyst in 80 vol% distilled water and 20 vol% colloidal silica (Aldrich, LUDOX AS-40) onto the polyester filters (200 mm × 300 mm) and baked at 60 °C subsequently. The net average powder loading on the polyester filters is approximately 0.65 g.

Control experiment in the absence of any photocatalyst was first carried out under fluorescent light irradiation (10000 lux). As shown in Figure 4-8, upon light irradiation, the toluene concentration was stabilized at ca. 50 ppm within the six hours of experimental duration, demonstrating the good sealing of the batch reactor. Background CO_2 concentration of ca. 2 ppm was detected by the GC-FID without formation of CO or other byproducts, ruling out the involvement of self-photolysis with toluene. With a leak proof reactor, CT-500-2 was used as a probe photocatalyst

to study the effect of light source/intensity, toluene concentration, relative humidity and role of oxygen for experimental condition optimization.

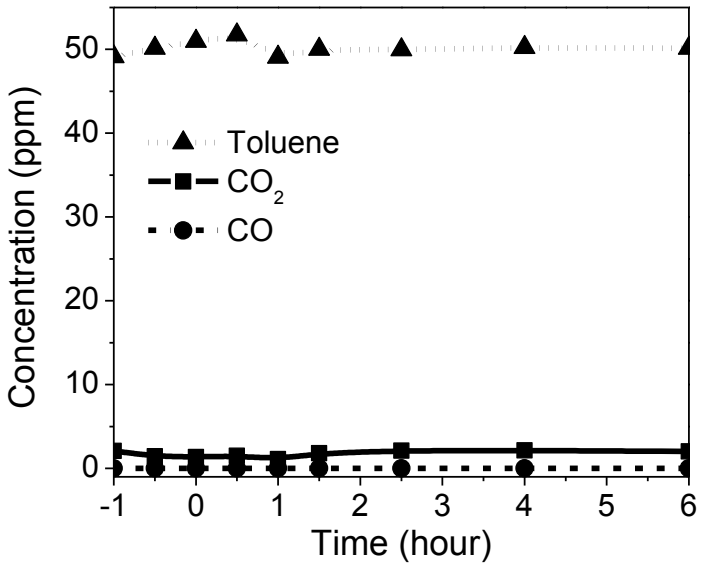

Figure 4-8. Control test in the absence of photocatalyst.

4.1.2.1 Effect of Light Source/Intensity

Cool daylight fluorescent lamp and T4 style LED strip light with emission spectrum shown in Figure 4-5 were used to compare the photocatalytic performance of CT-500-2 under different light irradiation. The toluene concentration and relative humidity were stabilized at ca. 50 ppm and 40% RH respectively for one hour before switching on the light.

As shown in Figure 4-9(a), upon light illumination, no significant change in toluene concentration but obvious CO_2 and minor CO formation were observed in all cases. The concentration of CO as a byproduct of the photocatalytic reaction fell well below

3 ppm, which was much lower than the recommended exposure limit of 35 ppm as an 8-hour TWA by NIOSH and thus would not cause any cardiovascular effects. The concentration of CO_2 as an indicator for complete mineralization increased linearly since the beginning of irradiation attributed the oxidation and abstraction of the methyl groups initially [135].

Under fluorescent light irradiation, CT-500-2 shows mineralization of ca. 18.57 ppm toluene, calculated by carbon balance based on the CO_2 evolution of 129.96 ppm. With GG400 UV-block filter, the mineralization rate was lowered significantly by 55%, with CO_2 evolution of 58.02 ppm, equivalent to 8.29 ppm toluene mineralization, suggesting the important role of the light emission peak at 365 nm despite of its low intensity. By switching the light source to LED lamps with visible light emission only, the toluene mineralization was further reduced by 60% as compared to the case under fluorescent light irradiation with GG400, indicating 400 nm-435 nm near the absorption shoulder of CT-500-2 to be the vital visible light-active region.

The light intensity of the fluorescent lamp was reduced to 5000 lux and 2000 lux by adjusting the height of the light panel. As shown in Figure 4-9(b), no obvious change in toluene concentration was observed either. However, the complete mineralization rate was reduced drastically based on CO_2 formation rate. With 2000 lux irradiation, the mineralization rate was reduced down to 16% of that with 10000 lux irradiation. The CO byproduct was also decreased with a reduced light intensity.

Considering the crucial role of the three emission peaks at 365 nm, 403 nm and 435 nm, the subsequent experiment will be carried out under fluorescent light instead of LED irradiation. GG400 UV-block filter will be used when evaluating the visible light photoactivities. The light panel will be fixed at ca. 15 cm above the reactor to ensure illuminance of 10000 lux reaching at the sample.

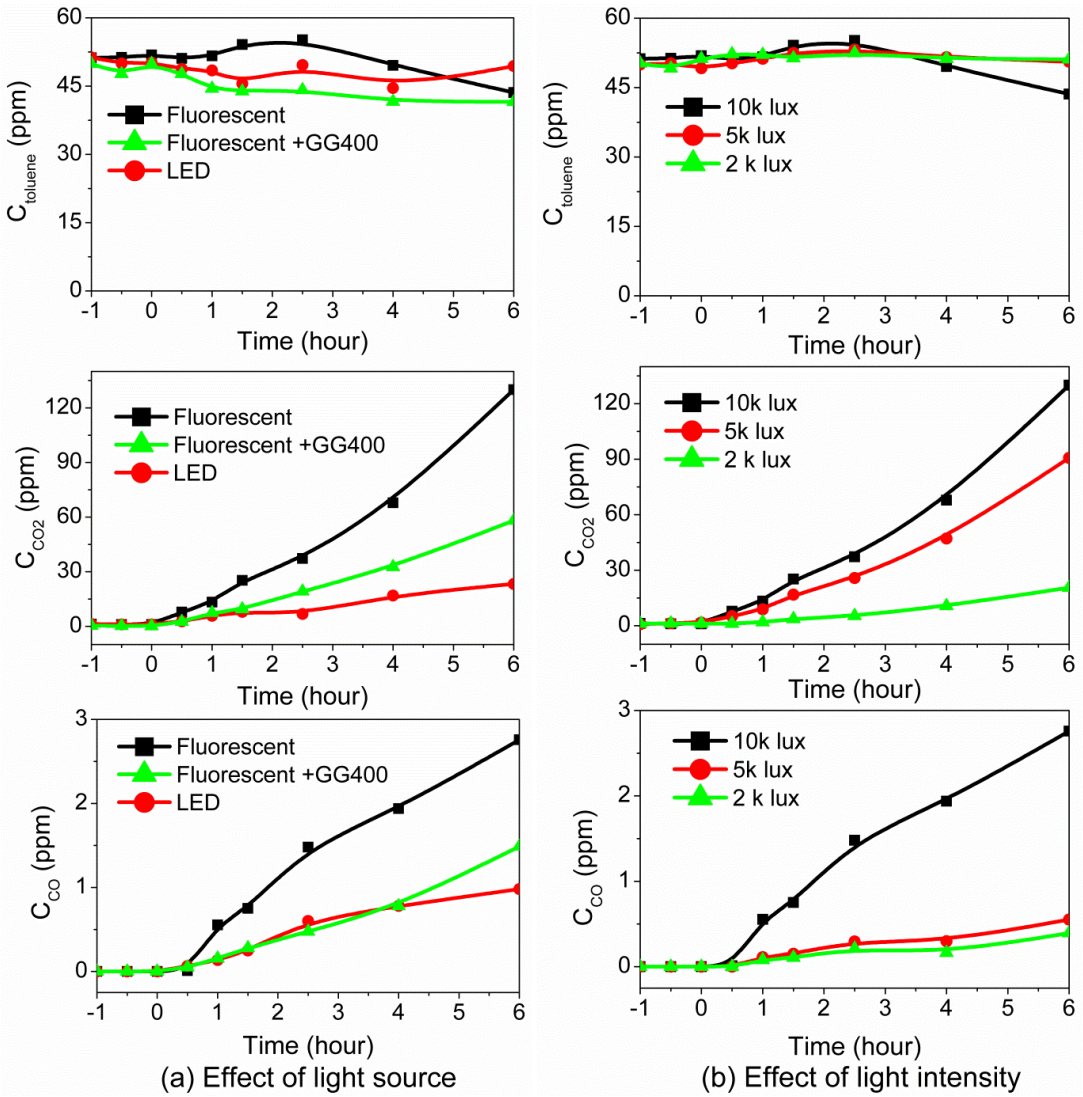

Figure 4-9. Effect of light source/intensity on photocatalytic mineralization of toluene.

4.1.2.2 Effect of Pollutant Concentration

The toluene feed concentration was varied from 20 ppm to 180 ppm. As shown in Figure 4-10(a), toluene does not show faster degradation with higher initial concentration. The CO evolution fell well below 4 ppm. The formation of CO_2 followed similar linear trend within the five hours of experimental duration, regardless of the initial toluene concentration, suggesting that the reaction was limited by the saturation of the surface active sites in this particular reaction system. Thus, the toluene feed concentration was kept at 40 ppm for the subsequent tests.

4.1.2.3 Effect of Relative Humidity

In photocatalytic process, the adsorption of water molecules onto photocatalyst is important for generation of hydroxyl radicals with strong oxidation power to enhance the photocatalytic efficiency [135]. At the same time, the adsorption of pollutants onto photocatalyst is also a critical step to determine the reaction rate. Considering the possible competition for the active sites between water molecules and pollutants, it is necessary to study the effect of relative humidity in the existing system.

As show in Figure 4-10(b), increase in toluene concentration was observed upon shinning of light, due to desorption of the adsorbed toluene from polyester filter induced by light heating. The desorption of toluene was less obvious with higher humidity level as compared to dry condition (0% RH), suggesting that competition for active sites did exist between the water and toluene molecules. Despite the competition for active sites with the pollutants, water molecules did play a vital role

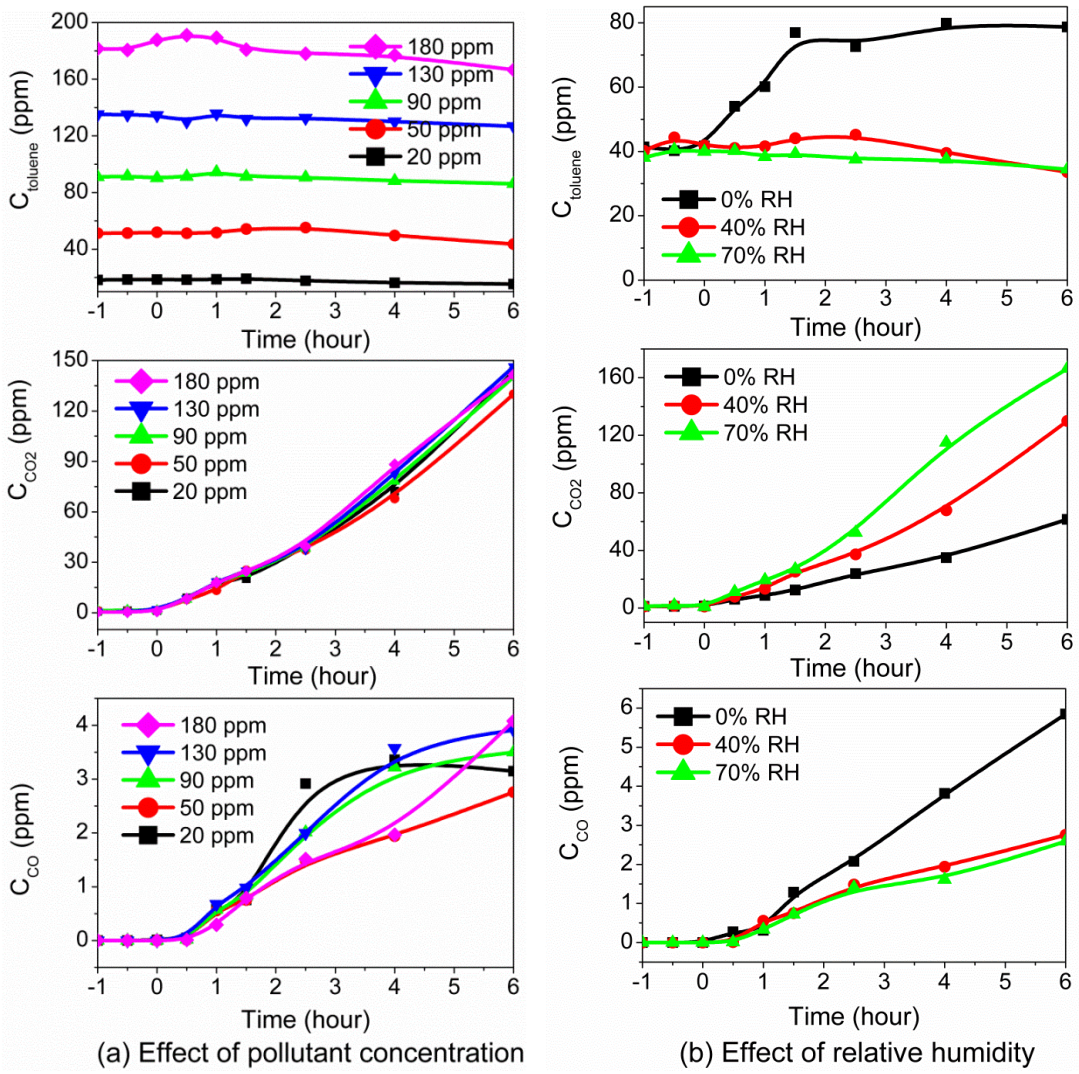

Figure 4-10. Effect of pollutant concentration/relative humidity on photocatalytic mineralization of toluene.

in enhancing the complete mineralization, as evidenced by the improved CO_2 evolution or increased mineralization rate at higher humidity level, which was similarly observed in O. Debono et al.'s work [135]. It is noteworthy that the absence of moisture results in incomplete photocatalytic reaction, as suggested by the higher CO formation of 5.85 ppm at dry condition. Thus, the presence of water molecules not only improves the degradation of toluene but also promotes the

conversion of CO to CO_2. For the subsequent tests, a humidity level of 70% RH will be used.

4.1.2.4 Role of Oxygen

In the photocatalytic reaction, it is generally accepted that the photo-generated electrons will be consumed by the adsorbed oxygen molecules to form super oxide anion $\bullet O^{2-}$, which will subsequently react with the hydroxyl derivatives to form hydroxyl radicals to take part in the degradation of organic pollutants. Thus, oxygen appears as an important electron trapper to prevent the recombination of photo-generated carriers. The zero air as carrier gas was replaced with N_2 to study the photocatalytic degradation of toluene in the absence of O_2.

As shown in Figure 4-11, desorption of toluene upon light shining was less obvious in N_2 than in zero air, suggesting the better absorption of toluene onto photocatalyst in the presence of O_2 in dark condition. The photocatalytic reaction was hindered in the absence of O_2 as evidenced by the reduced formation of CO_2 and CO, due to minimal $\bullet O^{2-}$ production and thus less OH• formation. There is barely any mineralization when the water moisture is absent as well, with only traces of CO generated. Comparing the CO_2 generation in the case of air|0%RH and N_2|70%RH with N_2|0%RH, it is obvious that O_2 plays a more critical role than moisture in promoting the complete mineralization of toluene. Therefore, all the subsequent comparison tests will be carried out with zero air as the diluting and carrier gas to ensure the presence of oxygen for photocatalytic performance enhancement.

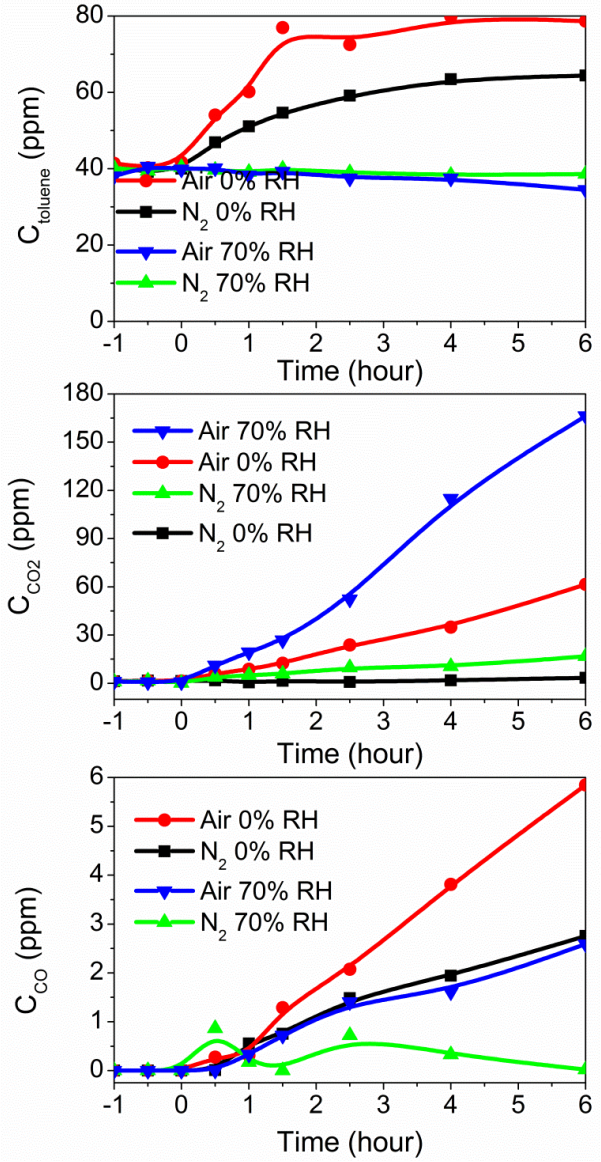

Figure 4-11. Role of O_2 in photocatalytic mineralization of toluene.

4.1.2.5 Comparison among Different Samples

The photocatalytic performance of the synthesized C-TiO_2 was compared with the N-TiO_2 synthesized by similar approach via thermal oxidation of TiN at 450-550 °C for two hours as well as the commercially available TiO_2 (Degussa P25) and C-TiO_2 (Kronos vlp 7000) under fluorescent light irradiation. With fixed light intensity of

10000 lux irradiating on the photocatalytic samples, 40 ppm toluene balanced with zero air at 70% RH was supplied to the batch reactors. The amount of CO_2 evolution was monitored to represent the degree of mineralization as shown in Figure 4-12. All the samples were re-grouped into different series for comparison and their photocatalytic performance ranking was summarized as shown in Table 4-3.

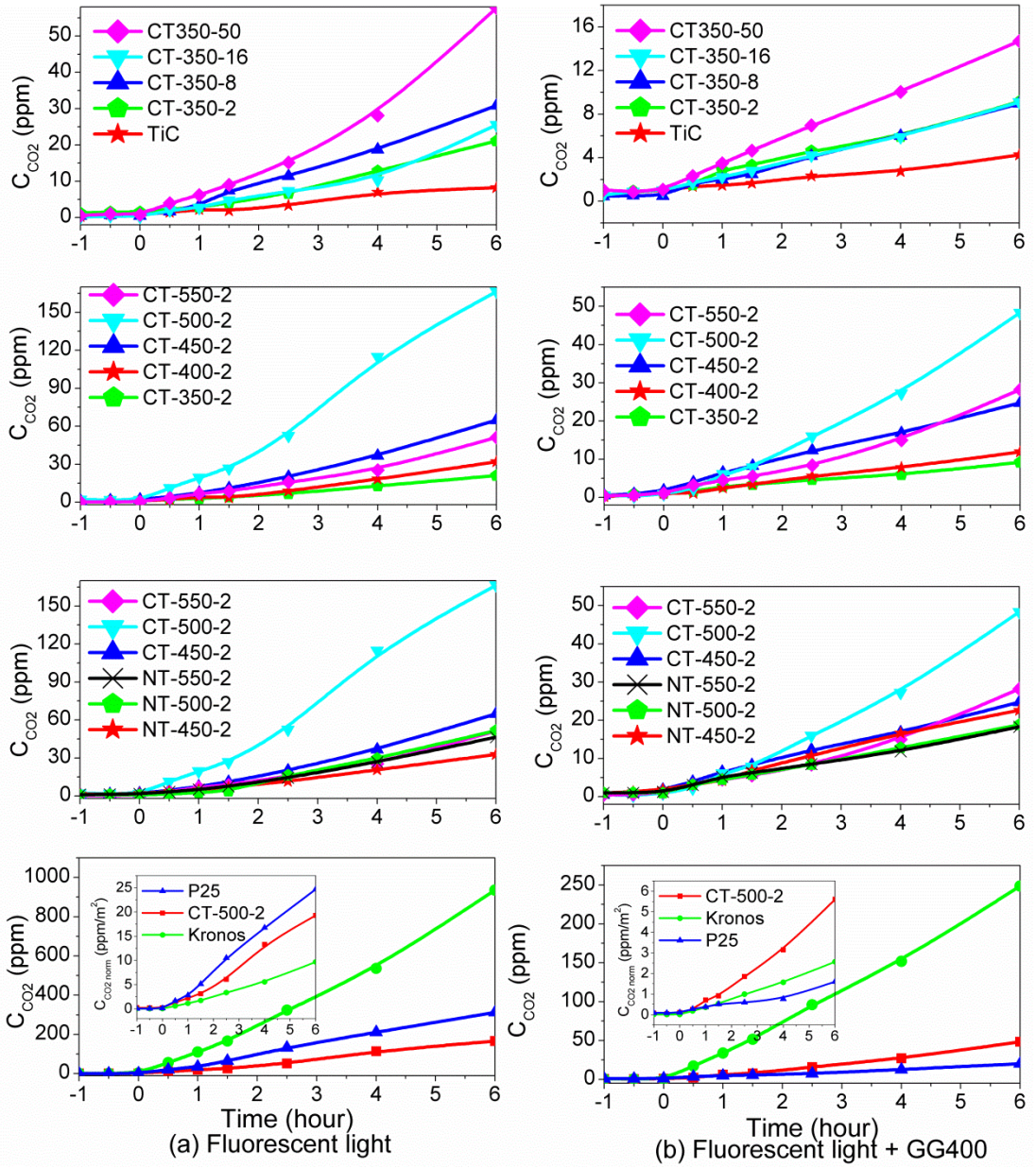

Figure 4-12. Photocatalytic degradation of gaseous toluene in batch reactors (10000 lux, 40 ppm toluene feed concentration, 70% RH, zero air as diluting gas).

Table 4-3. Photocatalytic performance ranking of the synthesized C-TiO_2, N-TiO_2 and commercial photocatalysts under UV-vis and visible light irradiation.

Sample series	Fluorescent light irradiation or UV-visible light irradiation	Fluorescent light irradiation+GG400 or visible light irradiation
350 ºC series	CT-350-50>CT-350-8>CT-350-16 ≥CT-350-2>TiC	CT-350-50>CT-350-8≈CT-350-2 ≈CT-350-16>TiC
Higher T series	CT-500-2>>CT-450-2>CT-550-2 >CT-400-2>CT-350-2	CT-500-2>CT-550-2≥CT-450-2 >CT-400-2>CT-350-2
C-TiO_2 vs N-TiO_2	CT-500-2>>CT-450-2> CT-550-2 ≈NT-500-2≥NT-550-2>NT-450-2	CT-500-2>CT-550-2≥CT-450-2 ≥NT-450-2>NT-500-2≈NT-550-2
CT-500-2 vs commercial photocatalyst	Kronos>>P25>CT-500-2 After normalization to S_{BET}: P25>CT-500-2>Kronos	Kronos>>CT-500-2>P25 After normalization to S_{BET}: CT-500-2>>Kronos >P25

Under fluorescent light irradiation, for C-TiO_2 prepared by mild oxidation of TiC at 350 ºC for 2-50 hours, CT-350-2, CT-350-8 and CT-350-16 have shown quite similar mineralization rate of toluene while the best photocatalytic performance was achieved on CT-350-50 with the longest time of calcination. Further annealing may give rise to even higher mineralization rate, however this is not suitable for mass-production of C-TiO_2 due to the time-consuming and costly process. It was noted that the TiC precursor also exhibited some photocatalytic effect on toluene degradation by evolving ca. 4-10 ppm CO_2 under light irradiation, which could be attributed to

the formation of TiO_2/C-TiO_2 due to surface oxidation of TiC in air, as supported by the XPS and FTIR analysis.

For C-TiO_2 prepared at higher oxidation temperature at 400-550 ºC for 2 hours, the photocatalytic performance was substantially improved as compared to mild oxidation series. The photocatalytic performance was enhanced with higher oxidation temperature up to 500 ºC. The best performance was achieved in the presence of CT-500-2 within the six hours of experimental duration. Based on carbon balance, 23.77 ppm of toluene has been completely mineralized, which is much higher than the 8.24 ppm degradation achieved in the presence of CT-350-50. The good performance with CT-500-2 could be attributed to the best balance among the amount of doped carbon and defects states, surface area, and ratio of antase/rutile phase. With further increase in temperature, CT-550-2 shows deteriorated effect as compared to CT-500-2, possibly due to several reasons: 1) the content of doped-carbon and carbonate-like species serving as photosensitizer has been reduced a lot with high temperature annealing; 2) the BET surface area for CT-550-2 has been decreased significantly to render less powder-pollutants interaction; 3) the content of anatase deemed as the more useful phase [136] has been reduced too much.

Satisfactory performance was achieved on N-TiO_2 synthesized by thermal oxidation of TiN at 450-550 ºC, but much poorer than that achieved in the presence of C-TiO_2 synthesized with a similar recipe. This finding is in good agreement with the conclusion made by Wang and Lewis stating that carbon doping is superior to nitrogen doping due to the production of the largest valence band red shift based on

their theoretical calculation [55], which was also supported by the UV-Vis absorption spectra in Figure 3-18.

In the presence of the commercial available C-TiO_2 Kronos vlp 7000, a very high CO_2 evolution of 936.14 ppm was obtained, equivalent to complete mineralization of 133.73 ppm toluene. Under the same experimental condition, the CO_2 formation in the presence of P25 and CT-500-2 was only 33% and 17% of that obtained with Kronos. The much higher mineralization rate with Kronos is possibly associated with its extremely high BET surface area of ca. 300 m^2/g as compared to 50 m^2/g and 27 m^2/g for P25 and CT-500-2 respectively. Much more hydroxyl group could be bonded to the surface to generate more $OH\cdot$, enhancing the photocatalytic efficiency. More active sites were available for adsorption of toluene as well. The small inset in Figure 4-12(a) shows the result obtained by normalizing the CO_2 formation to the BET surface of the respective samples. P25 active only in UV range has shown the best performance, followed by CT-500-2 and Kronos, which agrees well with the UV-vis absorption characteristics in Figure 3-18.

With GG400 UV-block filters, similar trend was obtained, except that the overall mineralization was reduced substantially by ca. 60% due to the removal of UV irradiation at 365 nm, suggesting that the synthesized photocatalysts are still UV light-driven but active in visible light range. After normalization to the BET surface area, CT-500-2 showed a much higher CO_2 evolution rate as compared to Kronos and P25, again in good agreement with the UV-vis absorption characteristic in Figure 3-18.

4.1.3 Photocatalytic Destruction of Gaseous Toluene in Dynamic Reactor

Besides the static test, the photocatalytic test pieces was also tested on continuous flow gaseous pollutants in dynamic reactors to investigate the feasibility of incorporating the photocatalysts into actual air purification system. The photocatalytic coating was prepared in a similar manner by spraying 50 g/L of each photocatalyst in 80 vol% distilled water and 20 vol% colloidal silica (Aldrich, LUDOX AS-40) onto the polyester filters (50 mm × 100 mm) for six passes and dried at 60 °C subsequently. The net average powder loading on the polyester filters is ca. 0.07 g.

4.1.3.1 Experimental Condition Optimization

The experimental condition was optimized with CT-500-2 as a probe photocatalyst by varying the gas flow rate from 50 sccm to 300 sccm and humidity level in the range of 0-70% RH.

Pollutant gas flow rate is an important parameter affecting the rate of photocatalytic oxidation as it affects the gas phase mass transfer and the transport of pollutants to the catalyst surface where oxidation takes place [137]. The photocatalytic oxidation performance of CT-500-2 was compared under different flow rate of 50 sccm, 100 sccm and 300 sccm, corresponding to a residence time of 26.67 seconds, 13.33 seconds, and 4.44 seconds, respectively. As shown in Figure 4-13, with decreasing toluene gas flow rate into the photoreactors, toluene had longer residence time on the photocatalytic test pieces and the formation of CO_2 was found to increase

significantly, suggesting an enhanced mineralization rate. At a flow rate of 50 sccm, the CO_2 formation reached ca. 9 ppm, corresponding to mineralization of 1.29 ppm toluene. It is expected that the mineralization rate can be further enhanced by reducing the gas flow rate. Unfortunately, considering the gas charging loss in the gas piping from the reactors to the GC for the current dynamic study with continuous gas flow, it is not recommended to reduce the gas flow rate to below 50 sccm unless the current gas sampling time of 4 minutes was prolonged to ensure the minimal gas sample amount of 2 mL into the sampling loop. Thus, the flow rate was fixed at 50 sccm for the comparison among different photocatalytic test pieces in the subsequent tests.

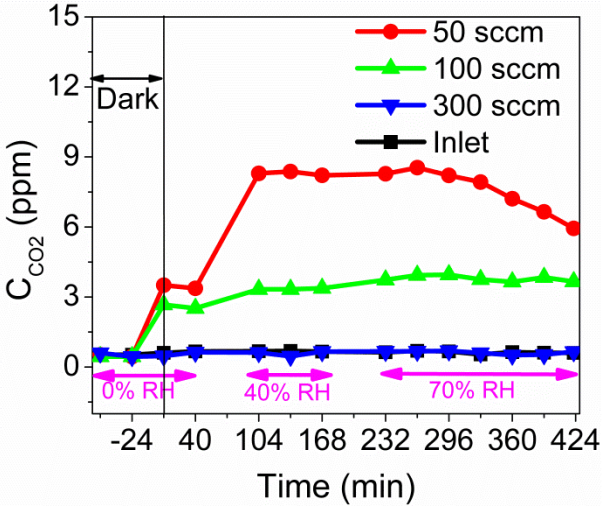

Figure 4-13. Optimization of gas flow rate and relative humidity in dynamic reactors.

The humidity level in the gas stream was varied by changing the infusion rate of the syringe pump SP2 in the range of 0-10 mL/hr. As shown in Figure 4-13, the initial humidity level is set at 0%RH at the beginning of test. Minimal CO_2 evolution was

observed in the dark condition regardless of the gas flow rate. Upon the shinning of light, the CO_2 was generated immediately for up to 3 ppm at a gas flow rate of 50 sccm. The infusion rate was subsequently set to 5.29 mL/hr to achieve a humidity level of 40%RH with 64 minutes stabilizing time. The CO_2 evolution was increased with the increasing humidity level, up to 9 ppm at 50 sccm. This is expected as higher humidity level means a higher chance to generate hydroxyl radical for toluene degradation. However, it should be noted that a higher humidity level also means that there is more competition between the moisture and toluene for active sites on photocatalyst. Further increasing of the humidity level up to 70%RH did not promote the toluene mineralization rate too much, which can be attributed to the saturation of active sites with the continuous flow of toluene gas in the presence of moisture, confirming adsorption as the rate limiting step [138]. The humidity level was thus fixed at 40%RH for the comparison among different photocatalytic test pieces.

Catalyst deactivation with reduced CO_2 evolution rate was observed at 50 sccm, 70%RH after 296 minutes, again attributed to the saturation of active sites. Although no gaseous intermediates were detected in our experiment, it should be noted that analysis of the products recovered from the used photocatalysts by various solvents usually shows the formation of benzyl alcohol, benzaldehyde, benzoic acid and derivatives of these intermediates in literature [75, 107, 135, 137], which were strongly adsorbed to and accumulated on the catalyst surface. Their presence was not verified in our study due to the difficulty in extract intermediates from polyester filters. However, the deactivation of CT-500-2 could be attributed to the surface accumulation of those less active intermediates. It should be noted that the

deactivated test pieces can be gradually regenerated by subjecting to zero air flow under the fluorescent light irradiation for two hours.

4.1.3.2 Comparison among Different Samples

Under continuous flow, the photocatalytic performance of the different photocatalysts followed similar order as in the batch test. As shown in Figure 4-14, minimal CO_2 concentration was detected in the inlet and control sample under all irradiation conditions. Under fluorescent light irradiation, Kronos with the largest surface area again exhibited the best photocatalytic performance by generating 15 ppm CO_2. However, fast deactivation was observed shortly due to blocking of active sites by the intermediates [59]. P25 showed satisfactory performance secondary to Kronos, followed by CT-500-2 and NT-500-2. With GG400 UV block filters, the CO_2 evolution rate was reduced by ca. 80% for P25 while ca. 65% for all the other samples.

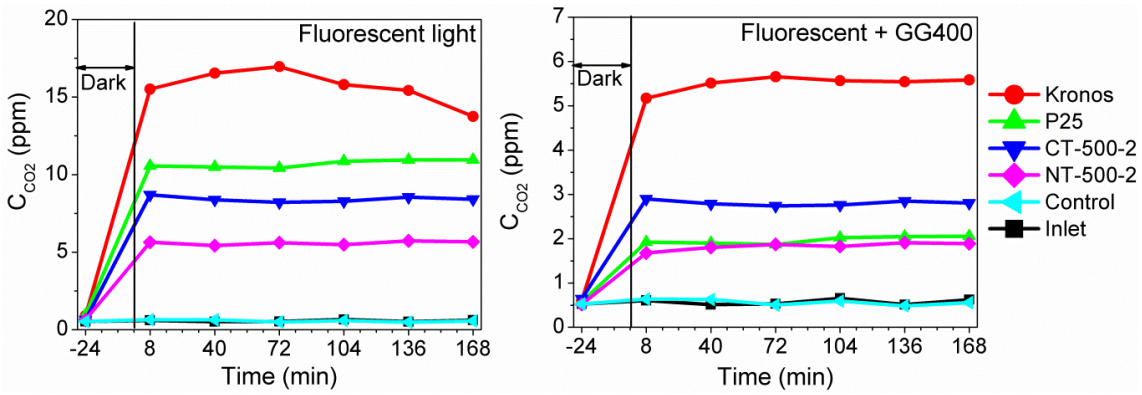

Figure 4-14. Photocatalytic degradation of gaseous toluene in dynamic reactors (10000 lux, 40 ppm toluene feed concentration, 40% RH, 50 sccm gas flow rate, zero air as diluting gas).

For actual air treatment, it is expected that the mineralization rate can be enhanced significantly by dispersing these photocatalyst over large surface area (e.g. direct spraying coat onto the wall) to allow the air bound pollutants to have higher chance to be captured and destroyed by the active components. The cleaning of the air will take action as long as the coated area is illuminated by the normal indoor lighting without additional energy.

4.2 Photocatalytic Disinfection of Microorganisms in Aqueous Suspension

4.2.1 Testing Protocol

4.2.1.1 Culture of Bacteria

Gram negative *E. coli* [139] and *E. faecalis* were used in the antimicrobial tests. The former was modified from the basic *E. coli* strain MG1655 with a chromosomal insertion of $P_{A1/04/03}$-*gfpmut3** (constitutive promoter driving the expression of green fluorescent protein gene) so that the *E. coli* can be observed under fluorescence microscope without addition of exogenous reagents and the latter with strain number ATCC 47077 was obtained commercially.

Single-species planktonic cultures of *E. coli* and *E. faecalis* were inoculated in fresh Luria-Bertani (LB) medium and Brain-Heart Infusion (BHI) medium respectively and incubated at 37 °C with shaking at 250 rpm. All bacteria were cultured in duplicate. Table 4-4 details the preparation recipe for different growth media,

together with the cell density of each species (CFU/mL) under the particular growth condition when the measured optical density (OD) at 600 nm OD_{600} = 1. As the cell densities (CFU/mL) can be correlated to their corresponding OD_{600} values, the starting inocula can be adjusted according to these values.

Table 4-4. Media for bacterial culture.

Bacteria	**Growth media**	**Preparation method**	**CFU/mL@ OD_{600}=1**
E. coli	Luria-Bertani (LB) medium	1% (w/v) bacto-tryptone, 0.5% (w/v) yeast extract, and 1% (w/v) NaCl	5.39×10^8
	Luria-Bertani (LB) agar	LB medium with 1.5% (w/v) bacto-agar	NA
E. faecalis	Brain-Heart Infusion (BHI) medium	From Becton Dickinson, Difco	1.17×10^8
	Brain-Heart Infusion(BHI) agar	BHI medium with 1.5% (w/v) bacto-agar	NA

* All media were sterilised by autoclaving at 121°C for 20 min

4.2.1.2 Quantification of Antimicrobial Effect

The antimicrobial effect of the synthesized C-TiO_2 was evaluated in suspension form with a powder loading of 2 g/L. Control tests involving commercially available C-TiO_2 (Kronos vlp 7000) and N-TiO_2 prepared via thermal oxidation of TiN at 450-550 ºC for 2 hours were evaluated concurrently for comparative study following the same viability assay. All the suspensions were freshly prepared prior to experiments using sterile water.

After overnight cultivation, the bacterial culture was serially diluted with distilled water to reach an initial cell density of ca. 10^7 CFU/mL, when OD_{60} for *E. coli* and *E.*

faecalis was measured to be 0.2 and 0.1 respectively with a BioSpec-Mini spectrometer (Shimadzu). 100 μl of the diluted culture was pipetted into 20 mL continuously stirred photocatalyst suspension to start the test in a custom-built photocatalytic reactor. The initial cell density is thus in the order of 5×10^4 CFU/mL. To prevent the heating effect, all the beakers containing the suspension were immersed in a petri dish with cooling water, which was replaced at each sampling time point.

The bactericidal effect is evaluated by estimating the viable cell density of bacteria at different time points with the standard plate-count technique. Specifically, the irradiated cell suspensions were withdrawn at regular time intervals and undergo a series of 10-fold dilutions by mixing 100 μL cultures with 900 μL sterile double-distilled H_2O. Aliquots of 100 μL of each suitably diluted culture was spread onto the corresponding nutrient agar plates in duplicate and incubated at 37 °C for 18-24 hours. The number of viable cells in terms of colony-forming units was counted and the evaluation was given in terms of survival fractions, S/S_0.

4.2.1.3 Light Source and Irradiation Conditions

The deactivation of microorganisms by C-TiO_2 was evaluated under different illumination conditions with the dark control test to serve as a reference. For the illuminated test, the suspension was irradiated with a Xenon lamp. As shown in Figure 4-15, the xenon lamp emits light mainly in the visible light range. There are only two small emission peaks below 400 nm, which can be completely eliminated with the optical cut-off filters (Melles Griot, GG400 and GG435) for visible light

activity evaluation. The use of GG435 can remove additional two peaks in the range of 400-425 nm. The resultant light intensity onto the continuously stirred *E. coli* suspension is ca. 16000 lux.

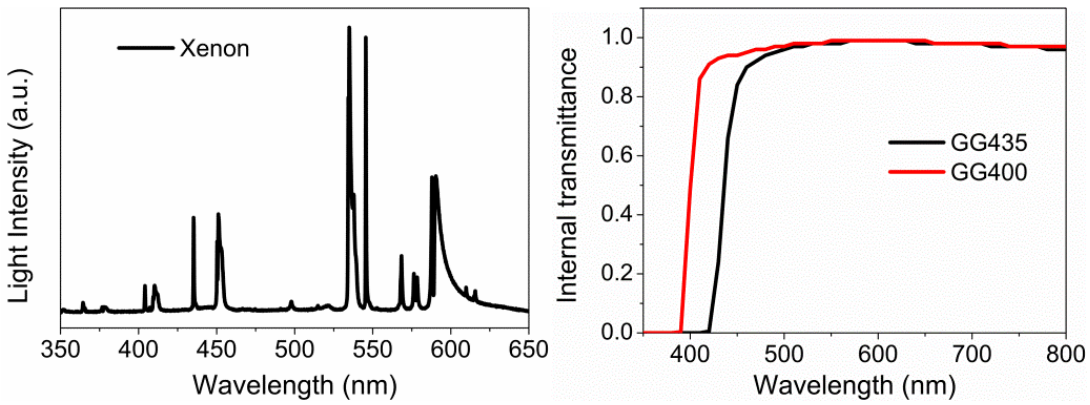

Figure 4-15. Emission spectra of Xenon light and transmission spectra of optical filters.

4.2.2 Photocatalytic Destruction of *Escherichia coli (E. coli)*

Dark condition should not initiate excitation of a photocatalyst to trigger any bacteria inactivation. However, as shown in Figure 4-16(a), the TiC sample and C-TiO_2 synthesized by oxidation of TiC at 350 °C could kill up to 30% of the *E. coli* within five hours in the dark. Similar antimicrobial actions on sputtered TiN film under dark condition was also unveiled in literature without explicit explanation [140]. The bactericidal effect of these samples could be attributed to the charge transfer interactions induced by the oxidation of the residual TiC under continuous stirring in water. This postulation can be supported by the decreased killing efficiency exhibited by C-TiO_2 with reduced TiC content as suggested by the corresponding XRD analysis, viz. C-TiO_2 with prolonged oxidation time at 350 °C and increased

oxidation temperature (400-550 ºC). The reference N-TiO_2 samples prepared by thermal oxidation of TiN at 450-550 °C remained inactive on *E. coli* in the dark, which is expected. The commercial C-TiO_2 Kronos vlp 7000 could kill 43% of the *E. coli*, which could be attributed to its small particle size and large BET surface area. With a small crystallite size in nanometer scale (~5-15 nm), the interactions between the powder and bacteria could be enhanced due to its high surface area and surface reactivity, posing additional physical/mechanical stresses on the cellular structure integrity [141, 142].

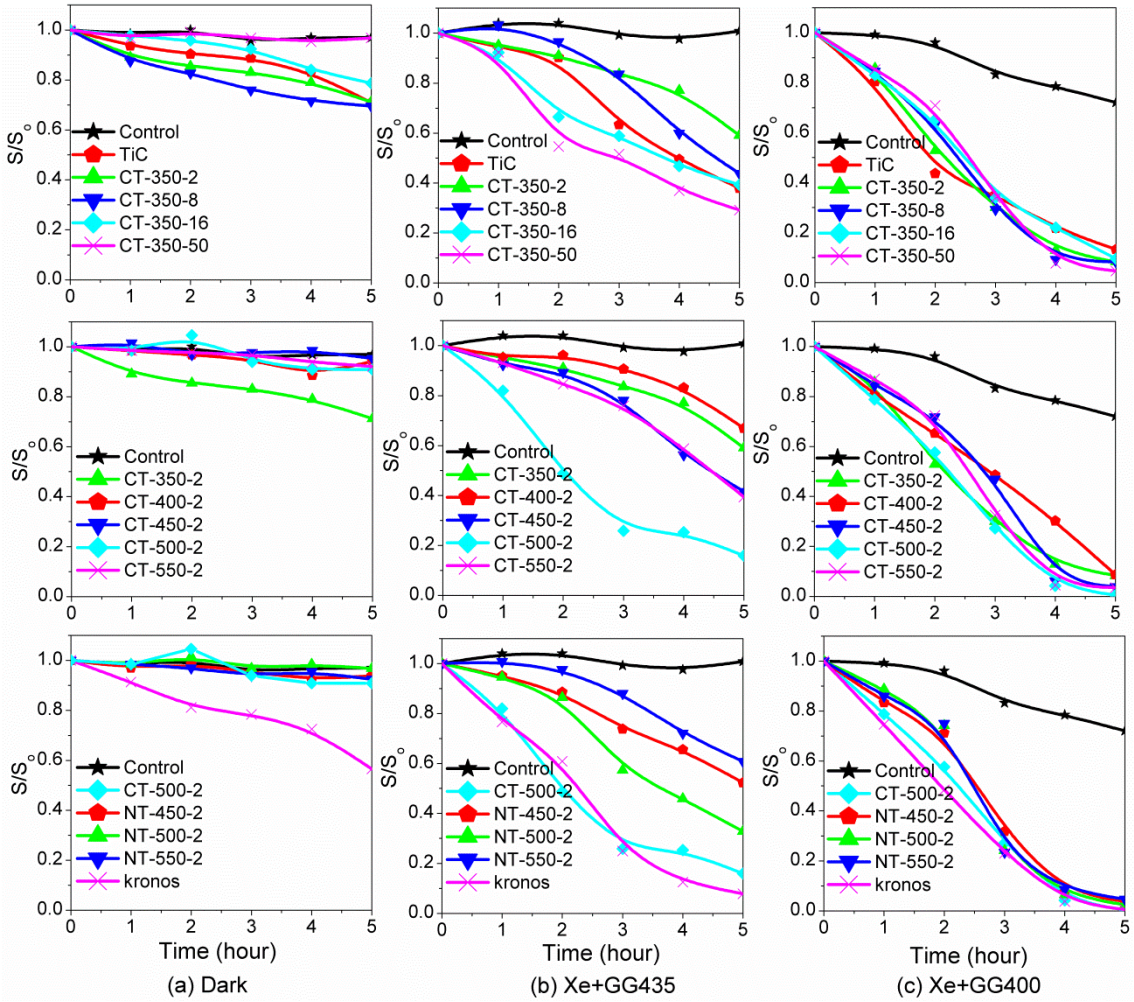

Figure 4-16. Photocatalytic inactivation of *E. coli*.

As shown in Figure 4-16(b) and Figure 4-16(c), under visible light irradiation, the bactericidal effect for all the samples was notably improved with respect to dark condition, suggesting photo-inactivation mechanism. In addition, with the optical filter GG400, the photocatalytic performance has been significantly enhanced as compared to that with GG435, suggesting the strong photo-activity in the range of 400-435 nm although there were only two small emission peaks present in this range of light emission spectrum, which is in good agreement with their visible light absorption behaviors observed in Figure 3-18. The accelerated deactivation of *E. coli* observed on TiC can be understood by the photocatalytic behavior of TiO_2/C-TiO_2, which was formed during the continuous stirring of TiC in ambient environment.

Overall, the photocatalytic efficiency of all the samples followed a similar trend as in the degradation of gaseous toluene. The photocatalytic performance of the C-TiO_2 was enhanced with prolonged oxidation time (350 ºC, 2-50 hours) or higher oxidation temperature (400-550 ºC, 2 hours) up to 500 ºC. With further increase in temperature, CT-550-2 again showed deteriorated effect as compared to CT-500-2 with the same postulation suggested in section 4.2.5 due to the reduced carbon content, decreased surface area and diminished anatase fraction.

In general, C-TiO_2 synthesized at higher oxidation temperature range (400-550 ºC, 2 hours) performed better than those prepared by mild oxidation, especially when the net photo-induced activities was considered by subtracting the bactericidal effect in the dark. CT-500-2 has achieved the best killing efficiency of 84% and 99.5% with GG435 and GG400 respectively, which is comparable to the commercial Kronos or even better with surface area normalization taken into consideration. The N-TiO_2

prepared by thermal oxidation of TiN appeared as a satisfactory disinfectant as well, with NT-500-2 showing 70.0-97.6% bactericidal efficiency under visible light irradiation. Yet, its performance was slightly secondary to C-TiO_2 prepared at a similar condition, which is expected due to its reduced light absorption in the visible light range.

4.2.3 Photocatalytic Destruction of *Enterococcus Faecalis* (*E. faecalis*)

As shown in Figure 4-17, the effectiveness of all the samples on *E. faecalis* again followed the similar trend as in the degradation of gaseous toluene and inactivation of *E. coli*. Under the dark condition, the gram-positive *E. faecalis* survived well in the presence of all the samples except for TiC precursor and Kronos. The detrimental effect of TiC and Kronos on *E. faecalis* can be again attributed to the charge transfer interactions induced by oxidation of the TiC and nano-size effect, respectively.

Under visible light irradiation, the *E. faecalis* appeared to be more resistant to photoinduced stress than *E. coli*. As *E. faecalis* does not produce catalase, its enzymatic self-defence mechanisms should be less efficient as compared to *E. coli* [143]. Therefore, the different survival abilities observed on *E. coli* and *E. faecalis* most probably result from differences in their cell wall structures instead of in catalase production [144]. The thicker cell wall together with the ability to form a protein capsule under stressful conditions renders *E. faecalis* to be more robust against photoinactivation [143]. It is noteworthy that despite of the different photoresponse, similar shape of inactivation curves was observed on *E. coli* and *E. faecalis*, with an initial delay followed by a faster inactivation, suggesting the cell

wall destruction to be the time-consuming and critical step to trigger the complete inactivation.

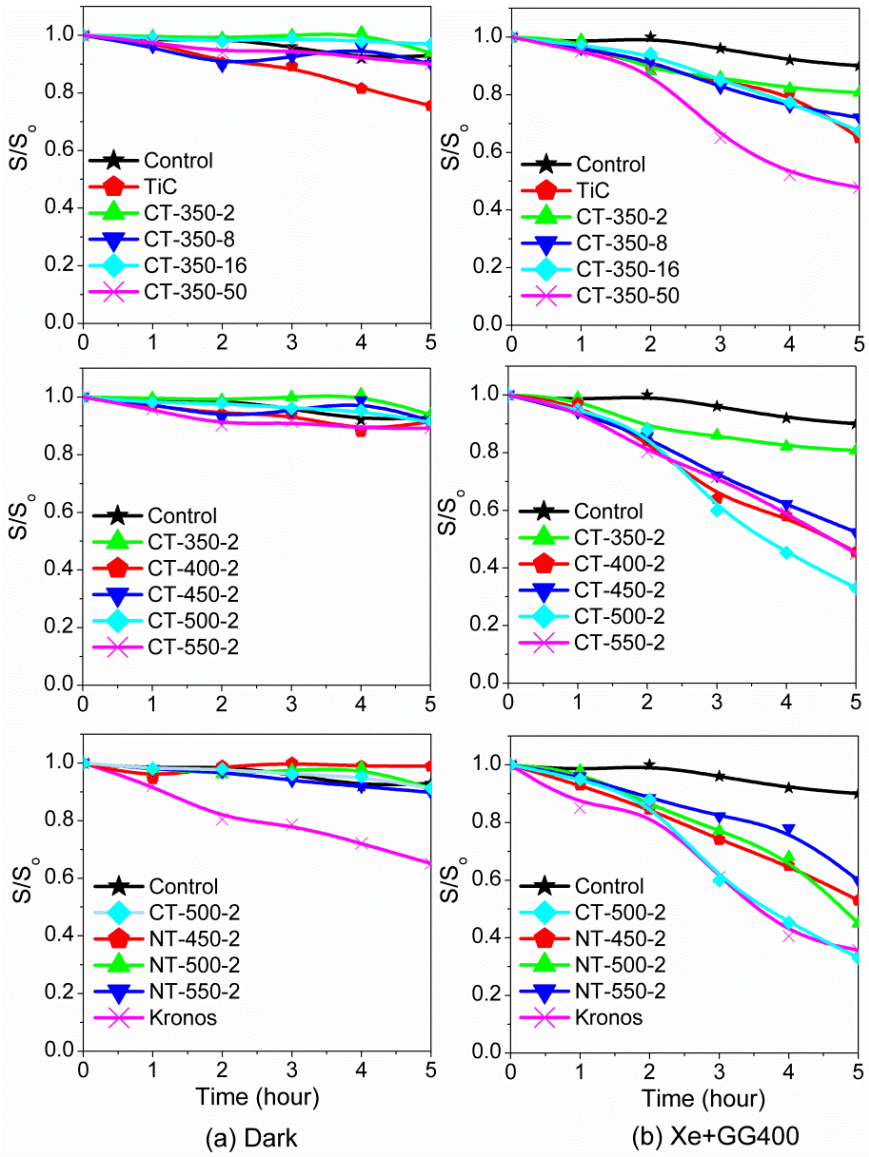

Figure 4-17. Photocatalytic inactivation of *E. faecalis*.

4.3 Chapter Summary

With the custom-built test system for examining degradation of gaseous pollutants, the photocatalytic performance of the synthesized C-TiO_2 nanoparticles in coated form was evaluated on gaseous toluene. The experimental conditions were optimized in the batch reactors with CT-500-2 as a probe photocatalyst with fixed light intensity of 10000 lux irradiating on the photocatalytic samples, 40 ppm toluene feeding gas balanced with zero air at 70% RH. In general, the synthesized C-TiO_2 exhibited photocatalytic performance superior to N-TiO_2 prepared with similar recipe due to the production of larger red shift. C-TiO_2 prepared at higher oxidation temperature of 400-550 ºC with a shorter duration of 2 hours has shown better mineralization efficiency than those prepared by the conventional time-consuming mild oxidation process, providing a facile method for large-scale production of C-TiO_2 suitable for solar applications or indoor applications with higher quantum efficiency. CT-500-2 has demonstrated the best performance by completely mineralizing 23.77 ppm of toluene within six hours, whose efficiency is even higher than the commercial C-TiO_2 Kronos vlp 7000 after normalizing to its surface area. Under continuous flow condition, similar trend was obtained under the irradiation of 10000 lux fluorescent light, 40 ppm toluene feeding gas, 40% RH and 50 sccm flow rate, further adding the feasibility of incorporating the C-TiO_2 photocatalysts in air conditioning system or large indoor surface area for effective air treatment.

The effectiveness of the synthesized C-TiO_2 nanoparticles on disinfection of microorganisms has also been proven on gram-negative *E. coli* and gram-positive *E.*

faecalis with different cell wall structures. All the C-TiO_2 appeared as promising visible light-active photocatalysts by showing significantly enhanced performance under visible light irradiation with respect to the dark condition, increasing the potential of utilizing C-TiO_2 in the actual water/air disinfection process with the use of only natural light. In general, C-TiO_2 synthesized at higher oxidation temperature demonstrated higher bactericidal efficiency than those prepared by mild oxidation process, with performance comparable to the commercially available C-TiO_2 Kronos vlp 7000 and superior to N-TiO_2 produced by similar recipe. Thus, the synthesis process for visible light-active C-TiO_2 can be drastically simplified with a much shorted processing time, suitable for large-scale production.

CHAPTER 5 : TOWARDS FURTHER IMPROVEMENT: PLATINUM / SILVER LOADED CARBON-DOPED TITANIUM DIOXIDE

The visible light photocatalytic potential of the C-TiO_2 synthesized by thermal oxidation of TiC has been successfully demonstrated with the removal of volatile organic compounds and disinfection of microorganisms. However, the photocatalytic efficiency of the C-TiO_2 may not be optimized due to the introduction of charge carrier recombination centers by the dopants to induce fast electron-hole recombination [145]. In this regard, co-modification of TiO_2 with noble metal and carbon appears as a promising solution to tackle this challenge. The carbon doping helps to enhance the visible light absorption. At the same time, the noble metal can effectively enhance the charge carrier separation by forming a Schottky barrier with the TiO_2/C-TiO_2 surface to conduct away the photogenerated electrons irreversibly [35, 36, 146, 147]. In addition, the generation of surface plasmons on the noble metal could help to further enhance the visible light absorption [146]. It was reported that the visible light photocatalytic efficiency has been greatly enhanced with Ag/C-TiO_2 [146], Ag/N-TiO_2 [148, 149], and Pt/N-TiO_2 [150] due to the synergistic effects of noble metal modification and non-metal doping.

Inspired by these interesting studies, a novel synthesis approach was developed to synthesize Pt-loaded C-TiO_2 (Pt/C-TiO_2) and Ag-loaded C-TiO_2 (Ag/C-TiO_2) [37] in this chapter in an attempt to further improve the photocatalytic performance of C-TiO_2, specifically, by thermal oxidation of $H_2PtCl_6 \cdot 6H_2O$ or $AgNO_3$-impregnated TiC precursors for simultaneous TiO_2 formation, C doping and Pt/Ag modification in one single step. Followed by the synthesis, their physicochemical properties were studied via various characterization tools including XRD, Raman, XPS, TEM, UV-Vis diffuse reflectance and PL. The band structure and possible visible light photocatalytic mechanism were proposed with these characterization results. The enhancement of phototocatalytic performance in comparison to C-TiO_2 was finally evaluated for the degradation of gaseous toluene in batch reactors and decomposition of Rhodamine B under visible light irradiation.

5.1 One-Step Synthesis of Pt/C-TiO_2 and Ag/C-TiO_2

The Pt/C-TiO_2 and Ag/C-TiO_2 were synthesized by thermal oxidation of $H_2PtCl_6 \cdot 6H_2O$- and $AgNO_3$-impregnated TiC precursors, respectively. The nano-sized TiC (>99.0%) as a Ti and C source was supplied by Hefei Kaier Nanometer Energy & Technology while the $H_2PtCl_6 \cdot 6H_2O$ (≥37.50% Pt basis) and $AgNO_3$ (≥99.0%) as a Pt or Ag source respectively were obtained from Sigma-Aldrich.

The $H_2PtCl_6 \cdot 6H_2O$ or $AgNO_3$ was mixed with the TiC in 10 mL ethanol via magnetic stirring at 500 rpm, 80 ºC. After the evaporation of ethanol, the dried precursor was further homogenized with hand-milling in mortar and subsequently oxidized in a

muffle furnace (F62700, Barnstead) at 500 ºC for 2 hours in air. The amount of loaded Pt or Ag was controlled at 0.5, 1.0, 2.0 and 5.0wt%. C-TiO_2 as a reference visible light-active photocatalyst was prepared by direct thermal oxidation of TiC in the same furnace at 500 ºC for 2 hours, which is essentially CT-500-2 with the best photocatalytic performance among all the synthesized C-TiO_2 in the previous study.

5.2 Characterization of Pt/C-TiO_2 and Ag/C-TiO_2

5.2.1 Crystallographic Study

The phase structure of the as-prepared Pt/C-TiO_2 and Ag/C-TiO_2 with 0.5-5.0wt% Pt and Ag was studied by XRD and Raman analysis in comparison to C-TiO_2.

5.2.1.1 X-Ray Diffraction Spectra

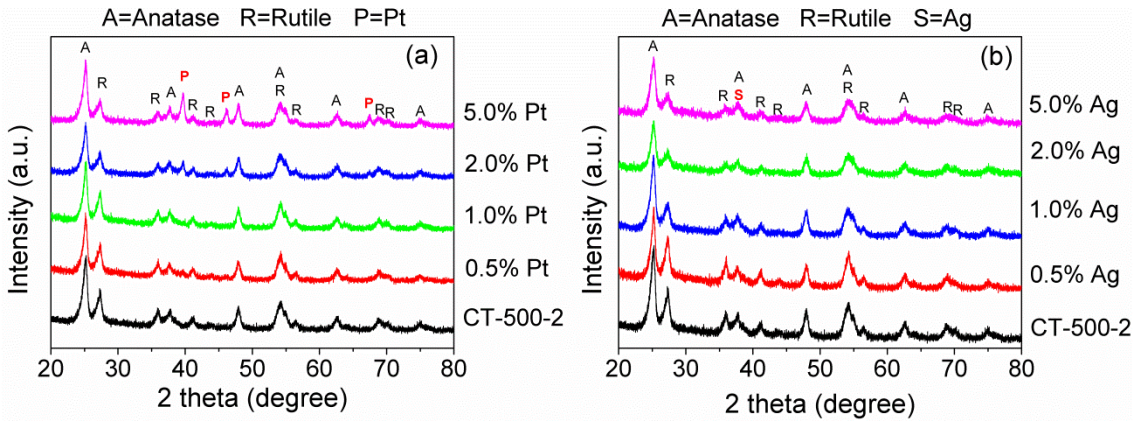

Figure 5-1. XRD patterns of (a) Pt/C-TiO_2 and (b) Ag/C-TiO_2.

The XRD patterns are presented in Figure 5-1. Mixed phase of anatase (JCPDS 21-1272) and rutile (JCPDS 65-1119) TiO_2 was observed in all the samples with the

rutile content remaining virtually the same at ca. 30%, which resembles the phase structure of the P25 TiO_2 powder, similar to C-TiO_2 or CT-500-2. For the Pt/C-TiO_2, there are three peaks at ca. 39.7º, 46.2º, and 67.5º appearing for C-TiO_2 with Pt content above 1.0%wt as shown in Figure 5-1(a), which could be indexed to (111), (200) and (220) planes of Pt (JCPDS 65-2868), suggesting the presence of metallic Pt. For the Ag/C-TiO_2, the overall peak intensity was reduced with the increased Ag concentration as shown in Figure 5-1(b), except at ca. 2θ = 38.6 º, where the most intense characteristic peak of metallic Ag at (111) plane (JCPDS74-1828) almost overlaps with the characteristic peak of anatase TiO_2 peak at (112) plane, suggesting the presence and increasing amount of metallic Ag. It is also noticed that the incorporation of Pt or Ag has a depression effect on the anatase/rutile grain growth, as indicated by the increased FWHM with increasing Pt or Ag content. Furthermore, no shifts in the peak positions were observed, indicating the deposition of Pt or Ag on the C-TiO_2 surface instead of into the lattice, which could be supported by the TEM observation.

5.2.1.2 Raman Spectra

Figure 5-2 presents the Raman spectra in the range of 900-100 cm^{-1}. Similar to C-TiO_2, anatase was revealed as the main phase in Pt/C-TiO_2 and Ag/C-TiO_2 with the observation of predominant peaks at ca. 638 cm^{-1}, 516 cm^{-1}, 396 cm^{-1}, 200 cm^{-1}, and 146 cm^{-1} [151]. Close inspection of the strongest characteristic peak at ca. 146 cm^{-1} revealed a blue shift towards higher wavenumber with increasing Pt or Ag concentration, possibly due to compressive strain introduced by the dopants [152].

The weakening and broadening of the spectra could be attributed to the aggregation of the dispersed Pt or Ag particles.

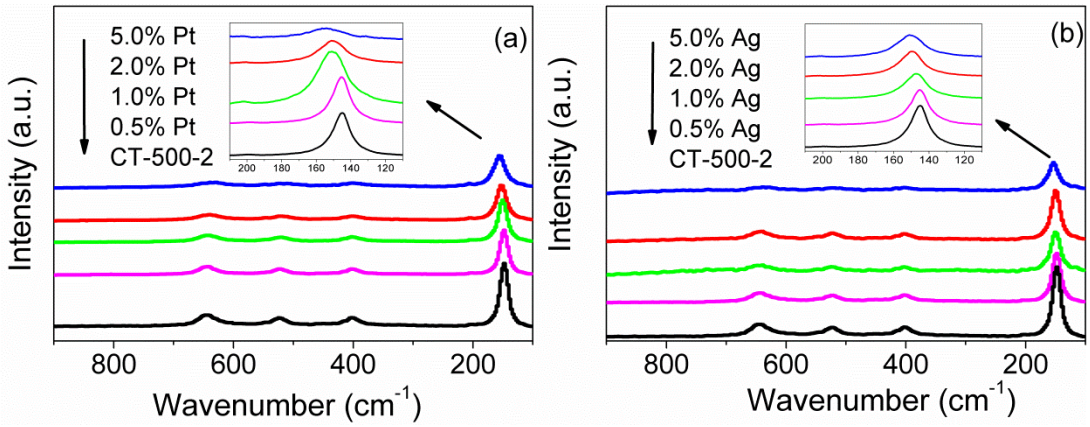

Figure 5-2. Raman spectra of (a) Pt/C-TiO_2 and (b) Ag/C-TiO_2 with the inset showing expanded part of the spectra in the range of 210-110 cm^{-1}.

5.2.2 Surface Morphology

Figure 5-3(a) shows the SEM image of the Pt/C-TiO_2 with 5.0wt% Pt (Pt/C-TiO_2-5.0%). The nanoparticles aggregated at some level with diameter in the range of 40-100 nm. From the TEM image (Figure 5-3(b)), the Pt nanoparticles in deep black color were uniformly distributed on the C-TiO_2 after the thermal treatment at 500 ºC. The HRTEM image in Figure 5-3(c) and (d) revealed polycrystalline SAED pattern and lattice atomic images of 0.352 nm and 0.324 nm, matching well with the d-spacing of anatase (101) planes and rutile(110) planes respectively, which is in good agreement with the XRD analysis. Pt nanoclusters in 5-20 nm were clearly observed due to their high electron density and good dispersion over the TiO_2, which could

form nano-composites with the TiO_2 to conduct away the photogenerated electrons for better charge carrier separation.

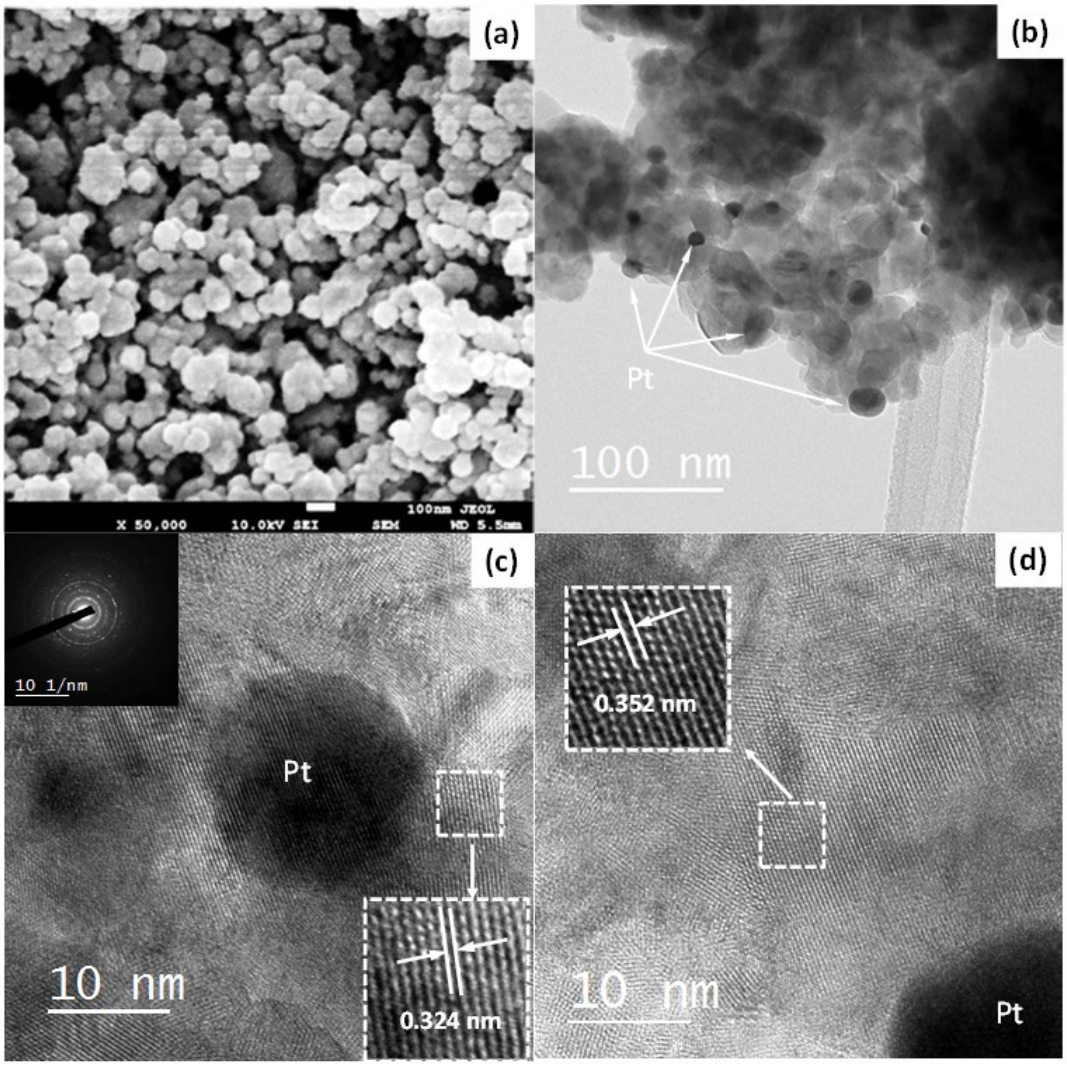

Figure 5-3. SEM (a) and TEM (b-d) of Pt/C-TiO_2-5.0% with inset in (c) showing the SAED image depicting the polycrystalline nature.

Ag/C-TiO_2-5.0% has exhibited similar morphology as shown in Figure 5-4. With the dark field scanning TEM (STEM) in the inset of Figure 5-4(b), a better compositional contrast was obtained for clear identification of Ag nanoparticles in

the agglomerated primary particles. In Figure 5-4(d), besides the identification of rutile (101) plane and anatase (101) plane with lattice atomic images of 0.249 nm and 0.352 nm, the Ag nanoparticles with an average diameter of 2-10 nm were seen strongly anchored onto TiO_2, which is much smaller in size than the Pt/C-TiO_2.

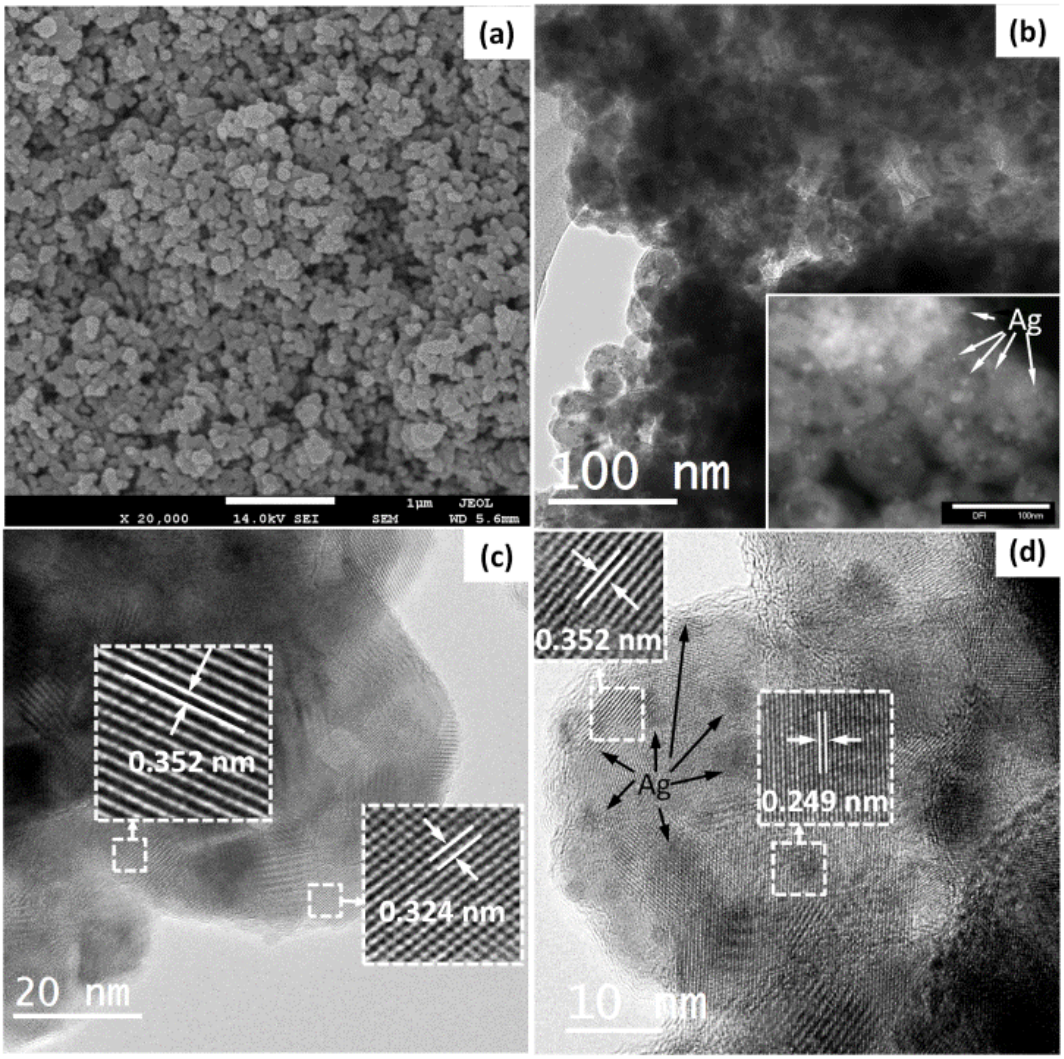

Figure 5-4. SEM (a) and TEM (b-d) of Ag/C-TiO_2-5.0% with inset in (b) showing the dark field image depicting Ag particles with better contrast.

5.2.3 Surface Chemical Analysis

The chemical state of the elements and total density of states (DOS) for the valence band (VB) of the Pt/C-TiO_2-5.0% and Ag/C-TiO_2-5.0% were investigated by XPS analysis with Ar^+ sputtering at 4 kV for 6 minutes.

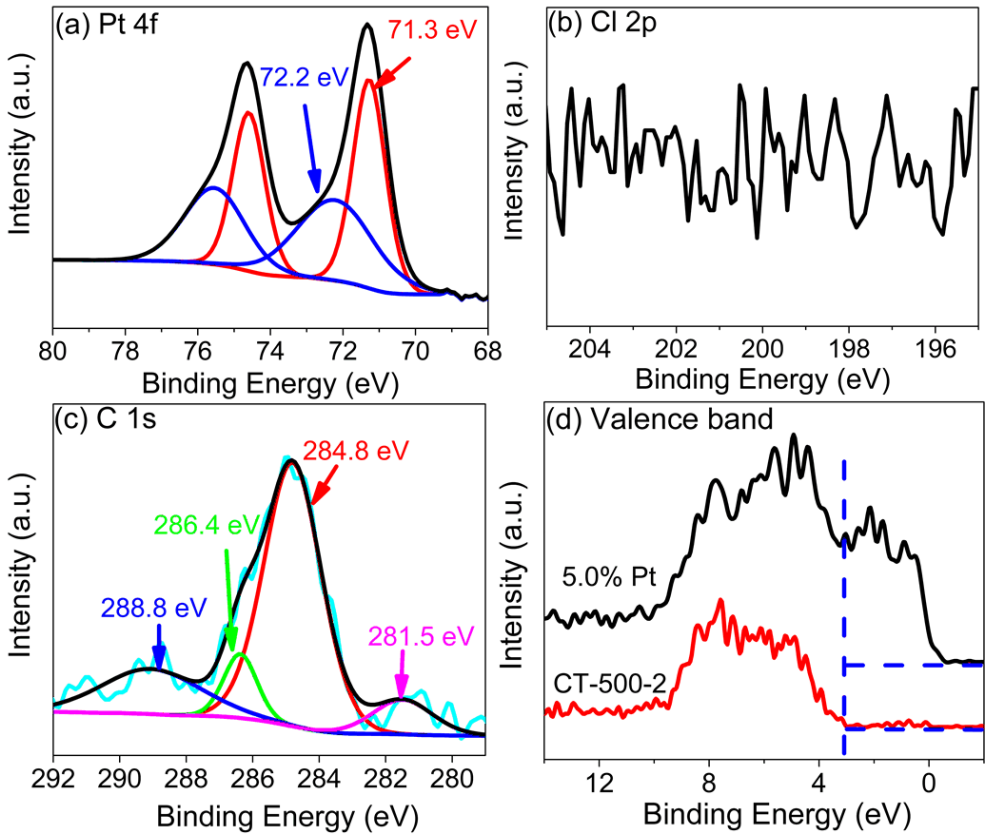

Figure 5-5. XPS spectra of (a) Pt 4d, (b) Cl 2p and (c) C1s of Pt/C-TiO_2-5.0% and (d) valence band of C-TiO_2 and Pt/C-TiO_2-5.0%.

As shown in Figure 5-5(a), two pairs of spin-orbital doublet was observed in Pt/C-TiO_2-5.0%, with the $4f_{7/2}$ peaks at 71.3 eV and 72.2 eV corresponding to the characteristic peaks for Pt(0) [153] and Pt(II) [150], respectively. The metallic Pt particles Pt(0) was produced due to the calcination of Pt chloride precursor at a high

temperature [153], consistent with the XRD analysis. The Pt(II) was also observed by Zhao et al. in their impregnated-prepared Pt-modified TiO_2 samples [154]. Due to the absence of obvious Cl^- peak as shown in Figure 5-5(b), the Pt(II) was most probably produced during the work-up of the XPS sample or due to the formation of Pt with adsorbed oxygen (PtO_{ads}) [155].

The spectra for core-level C 1s with four main peaks is shown in Figure 5-5(c), similar to that for C-TiO_2. The major peak at 284.8 eV was mainly attributed to adventitious hydrocarbon contaminations and might overlap with the graphitic-like C-C bonding (285.0 eV) [146]. The peaks at ca. 286.7 eV and 288.9 eV were ascribed to C-O and C=O bonds, respectively [64], whose concurrent presence indicates the formation of carbonate-like species due to interstitial carbon in TiO_2 lattice [147], which has also been confirmed by the peak identification at 1382 cm^{-1} and 2339 cm^{-1} in the FTIR spectra (not shown). The small peak at ca. 282.3 eV can be ascribed to O-Ti-C bond due to the substitutional carbon at oxygen sites in TiO_2 [156]. For the VB scan as shown in Figure 5-5(d), an increase of the DOS below 3.0 eV above the TiO_2 valence band edge was observed for both C-TiO_2 and Pt/C-TiO_2. For Pt/C-TiO_2, the modification of the TiO_2 valence was more obvious with more dispersed states, possibly due to the synergistic modification with carbon and platinum.

Figure 5-6(a) shows the Ag 3d XPS spectra of the Ag/C-TiO_2-5.0%. Only one pair of asymmetric spin-orbital doublet was observed at 368.0 eV and 374.0 eV, tailing slightly towards higher binding energy, which can be ascribed to Ag^0 in zero oxidation state [157], further confirming the XRD analysis. The absence of N 1s

peak in Figure 5-6(b) further confirmed the complete decomposition of $AgNO_3$ at 500 ºC to produce elemental Ag, NO_2 and O_2 [158]. The spectra for core-level C 1s was similar to that for Pt/C-TiO_2-5.0% and C-TiO_2. For Ag/C-TiO_2, the modification of the TiO_2 valence was more obvious with more dispersed states above 2.0 eV than C-TiO_2, again attributed to the synergistic modification with carbon and silver or that the incorporation of Ag could retain more carbon content to produce more continuous C 2p orbitals [146].

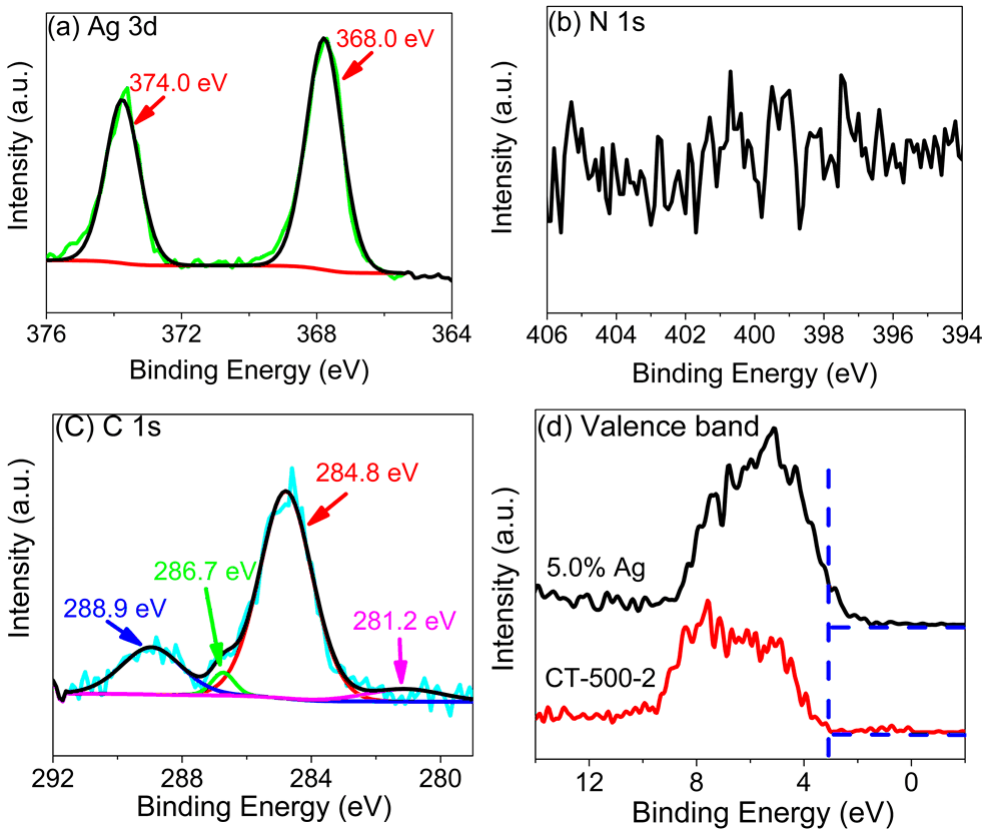

Figure 5-6. XPS spectra of (a) Ag 3d, (b) N 1s and (c) C1s of Ag/C-TiO_2-5.0% and (d) valence band of C-TiO_2 and Ag/C-TiO_2-5.0%.

5.2.4 Optical Study

5.2.4.1 UV-Vis Absorption Spectra

The UV-vis absorption spectra of the Pt/C-TiO_2 and Ag/C-TiO_2 are presented in Figure 5-7 in comparison to C-TiO_2. For C-TiO_2, the overall visible light absorbance was significantly increased as compared to pure TiO_2 with an absorption tail extending up to 800 nm, again attributed to the presence of graphite-like carbon and the coexistence of substitutional and interstitial carbon in the TiO_2. With Pt or Ag modification, the visible light absorption was further enhanced due to the surface plasmon resonance of Pt or Ag nanoparticles at ca. 450 nm [159, 160], together with the retaining of more carbonaceous species [146]. Thus, the absorbance intensity was gradually enhanced with increasing Pt or Ag content in the range of 400-800 nm. With the introduction of Pt, the enhancement of visible light absorption was more pronounced as compared to modification with Ag.

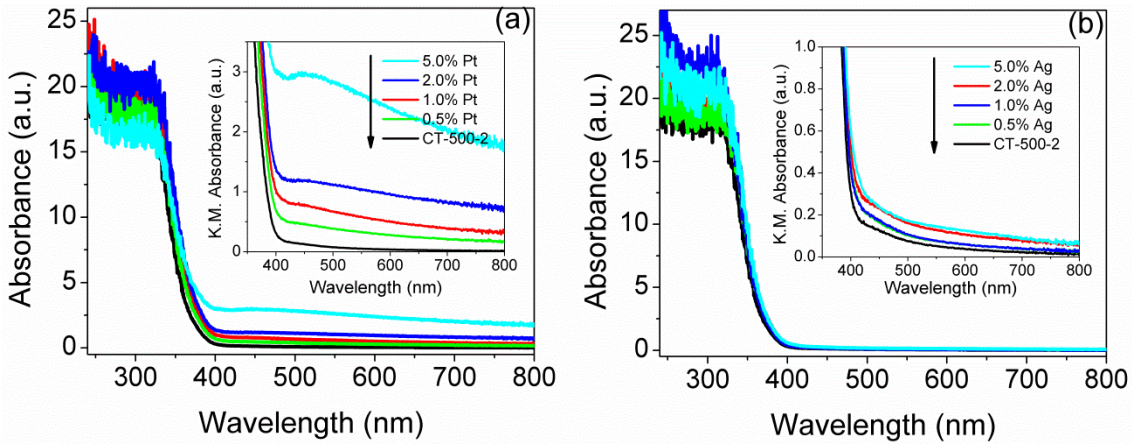

Figure 5-7. Optical absorption spectra with zoom in-view in the inset for (a) Pt/C-TiO_2 and (b) Ag/C-TiO_2.

5.2.4.2 Photoluminescence

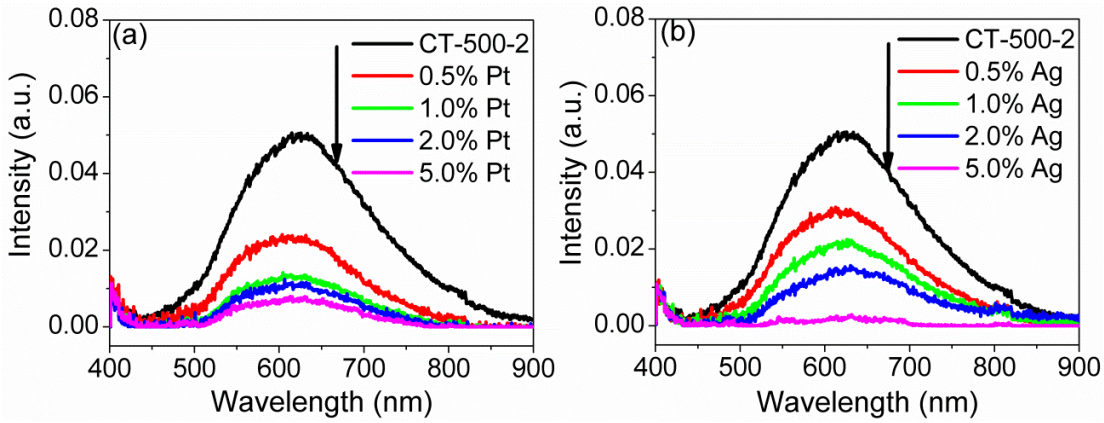

Figure 5-8. PL spectra of (a) Pt/C-TiO_2 and (b) Ag/C-TiO_2.

PL emission spectra were recorded in Figure 5-8 to investigate the efficiency of charge carrier trapping, migration, and transfer. With increasing Pt or Ag content, despite the enhanced visible light absorption, the PL emission intensity was significantly weakened as compared to the C-TiO_2, suggesting a lower recombination rate. The lower PL intensity could be attributed to the formation of Schottky barrier between the Pt or Ag nanoparticles and the TiO_2 particles to facilitate electron trapping by Pt or Ag nanoparticles. Hence, the modification of Pt or Ag indeed enhances the charge carrier separation, which could reasonably lead to higher photocatalytic efficiency.

5.3 Proposed Band Structure and Visible Light Photocatalytic Mechanism of Pt/C-TiO_2 and Ag/C-TiO_2

Based on the characterization results, the simplified band structure and photocatalytic oxidation mechanism under visible light irradiation of the Pt/C-TiO_2 and Ag/C-TiO_2 can be proposed as shown in Figure 5-9.

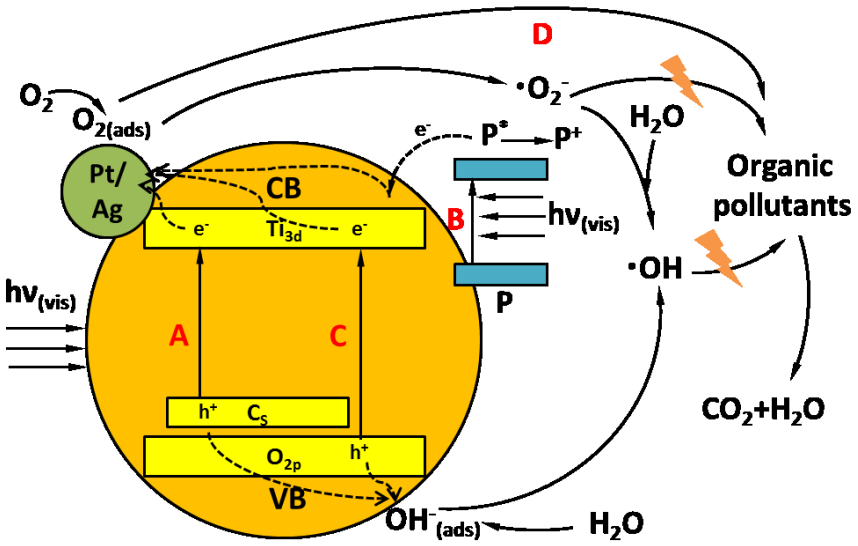

Figure 5-9. Proposed band structure of Pt/C-TiO_2 or Ag/C-TiO_2 and visible light photocatalytic process.

Pathway A Similar to C-TiO_2 (Figure 3-20), The bandgap of TiO_2 is first effectively narrowed by mixing C 2p orbitals with O 2p orbitals due to substitutional carbon (C_s) at oxygen sites [120], enabling visible light photocatalytic activation. The difference lies in that upon light irradiation, the photo-generated electrons were quickly scavenged by the Pt or Ag nanoparticles dispersed on the C-TiO_2 surface to allow efficient separation photogenerated electron and holes. The trapped electrons by Pt or

Ag nanoparticles and the VB holes will subsequently react with the adsorbed oxygen molecule ($O_{2(abs)}$) and water molecule ($OH^-_{(abs)}$) to produce reactive oxygen species (ROS) including $\cdot O_2^-$ and $\cdot OH$. Upon organic pollutants-photocatalyst contact, these reactive oxygen species could attack the pollutants to mineralize them into CO_2 and H_2O for a complete reaction.

Pathway B and *Pathway C* shares the similar mechanism with C-TiO_2 as detailed in Section 3.3, with the carbonate species on the surface of TiO_2 serving as photosensitizer (P) to absorb visible light and inject electrons into conduction band of TiO_2 [94, 161] or utilizing the visible light photocatalytic activities of rutile TiO_2 in the range of 400-420 nm.

Pathway D The Pt or Ag nanoparticles dispersed on the C-TiO_2 surface once come into contact with the organic pollutants may initiate the catalysis even in the dark condition [156, 162-164]. Formic acid, oxalic acid and 1,2,3- trihydroxybenzene were reported to be mineralized by Pt/TiO_2 under dark condition potentially via dehydrogenation, oxidative dehydrogenation or hydrolysis by the Pt deposits [162].

Excellent photocatalytic performance is thus expected with Pt/C-TiO_2 or Ag/C-TiO_2 nanoparticles due to the synergistic effect of carbon doping and platinum/silver modification.

5.4 Visible Light Photocatalytic Activities

The photocatalytic performance of the synthesized Pt/C-TiO_2 and Ag/C-TiO_2 was evaluated for the destruction of gaseous toluene in air and decomposition of Rhodamine B in aqueous suspension in comparison to the CT-500-2 under fluorescent light irradiation with GG400 UV-block filters to cut off the UV light portion.

5.4.1 Photocatalytic Destruction of Gaseous Toluene in Batch Reactor

With fixed light intensity of 10000 lux irradiating on the photocatalytic samples, 40 ppm toluene balanced with zero air at 70% RH was supplied to the batch reactors. The amount of CO_2 evolution was monitored to represent the degree of mineralization as shown in Figure 5-10.

Minimal CO_2 was generated in the dark in the presence of all the samples. Upon switching on of the light, the photocatalytic mineralization of toluene started immediately, as indicated by the evolution of CO_2. The mineralization efficiency was first increased with the concentration of Pt up to 2.0wt%, with CO_2 evolution of ca. 90 ppm, and subsequently reduced with 5.0wt% Pt as shown in Figure 5-10(a), similar to the reported work [164]. In the presence of Ag/C-TiO_2, the mineralization rate was enhanced continuously with Ag content up to 5.0wt% with CO_2 generation of ca. 70 ppm, which was slightly inferior to that with Pt/C-TiO_2. The performance enhancement in comparison to CT-500-2 was most probably due to the enhanced

visible light absorption and better charge carrier separation with introduction of Pt or Ag nanoparticles.

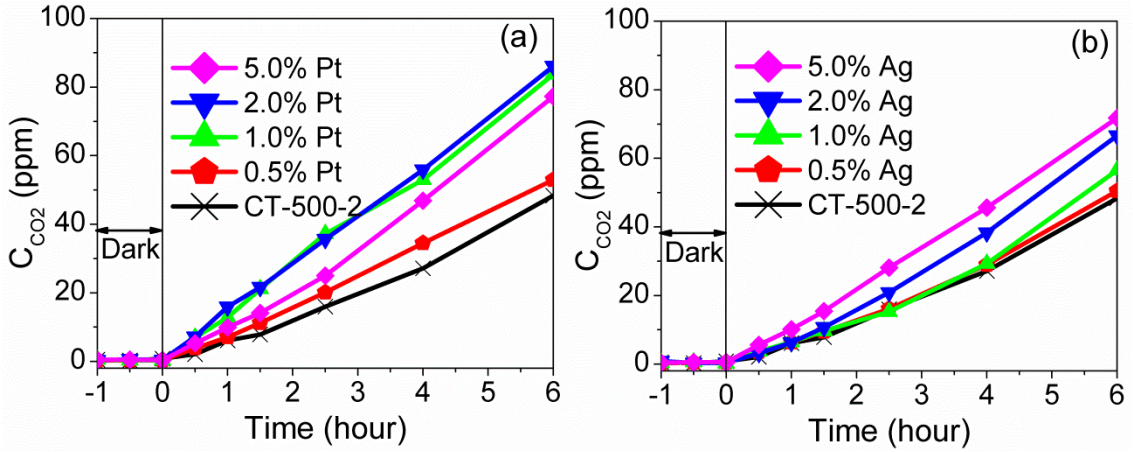

Figure 5-10. Photocatalytic degradation of gaseous toluene in batch reactors in the presence of (a) Pt/C-TiO_2 and (b) Ag/C-TiO_2 (fluorescent light + GG400, 10000 lux, 40 ppm toluene feed concentration, 70% RH, zero air as diluting gas).

5.4.2 Photocatalytic Decomposition of Rhodamine B in Aqueous Suspension

Rhodamine B (RhB) as one of the most common xanthene dyes has also been selected as a model pollutant due to its ease of encountering in water effluents and good stability as dye laser materials [165]. The photocatalytic experiment was conducted in the custom-built photocatalytic reactor equipped with office fluorescent light with fixed light intensity of 3000 lux irradiating on the photocatalytic samples. Optical cut-off filters (Melles Griot, GG400) were used to cut off the UV-light portion < 400 nm. Each sample was prepared with 15 μM RhB and 2 g/L photocatalyst in 50 mL flasks and transferred to 200 mL beakers. Before the

photocatalytic experiment was carried out, the suspension was maintained under stirring for two hours in dark condition to establish the reactant adsorption equilibrium. At different time points, 2 mL of the suspension was extracted and centrifuged to separate the photocatalysts from the solution. 1 mL of the centrifuged clear solution was sent for UV-Vis spectrum analysis (Ocean Optics, USB2000) to determine the degradation of RhB over time. After analysis, the solution was returned to the suspension to maintain the reactant volume.

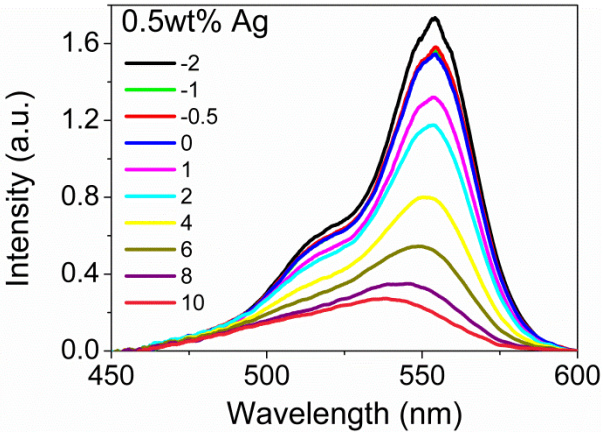

Figure 5-11. Absorption spectra for RhB in the presence of Ag/C-TiO_2-0.5%.

Figure 5-11 shows the typical absorption spectra for RhB solution obtained in the range of 450-600 nm in the presence of Ag/C-TiO_2-0.5%. The main peak at ca. 554 nm was due to the conjugated π-system [166] and its disappearance was monitored to indicate the degree of decomposition. Under visible light irradiation, the absorption maximum exhibited a gradual hypsochromic shift by shifting from 554 nm to 539 nm with the increased illumination time. This could be due to the formation of N,N,N′-Triethyl-rhodamine, which is the partial *N-deethylation* product of RhB [167]. Further illumination may cause a further shift towards 498 nm to

produce Rhodamine with four methyl groups being removed. It was also noted that the color of the suspension faded gradually during the test, indicating the simultaneous destruction of the chromosphere ring structure [168].

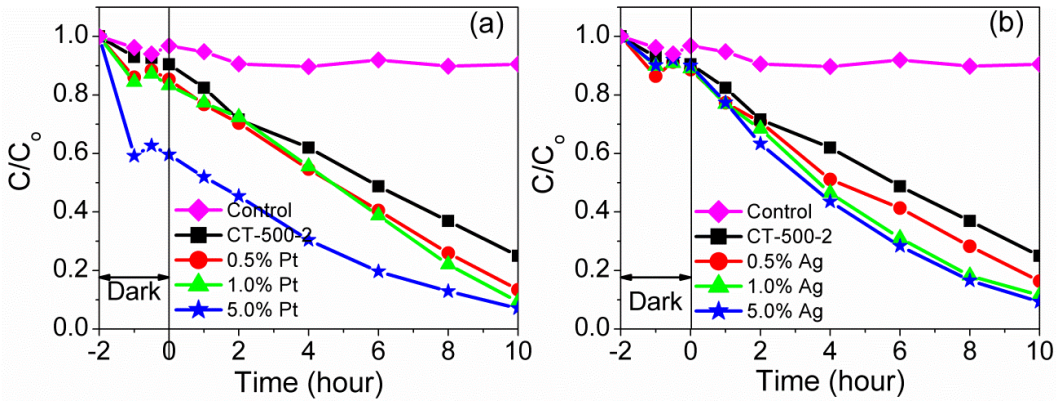

Figure 5-12. Photocatalytic decomposition of RhB in aqueous suspension in the presence of (a) Pt/C-TiO_2 and (b) Ag/C-TiO_2.

The normalized concentration of RhB in the presence of Pt/C-TiO_2 or Ag/C-TiO_2 was plotted against time as shown in Figure 5-12. Under the dark condition, adsorption equilibrium was established within 30 minutes for all the samples. It was noted that the adsorption of RhB on the Pt/C-TiO_2 appeared dependent on the Pt loading, which is similar to the observation by Kryukova et. al on the dark adsorption of acid orange 7 by Pt/TiO_2 [163]. Almost 40% of RhB has been adsorbed by the Pt/C-TiO_2-5.0% in the dark, which could be due to the Pt deposits as an electron sink to extract electrons from C-TiO_2 and subsequently transfer to adsorbed oxygen to induce the dark adsorption [163]. The dark adsorption with Ag/C-TiO_2 was not as obvious, possibly attributed to the relative smaller work function of Ag in comparison to Pt and thus less efficient photogenerated electrons trapping in the dark

[168]. Upon light irradiation, similar order was followed for the photocatalytic performance of Pt/C-TiO_2 and Ag/C-TiO_2 as in the case of toluene destruction, which is superior to the C-TiO_2 without co-doping of noble metals, demonstrating the potential of utilizing Pt/C-TiO_2 and Ag/C-TiO_2 in both air and water purification for organic pollutants removal.

5.5 Chapter Summary

Pt/C-TiO_2 and Ag/C-TiO_2 nanoparticles with 0.5-5.0wt% Pt or Ag were successfully synthesized by thermal oxidation of $H_2PtCl_6 \cdot 6H_2O$ and $AgNO_3$-impregnated TiC precursor at 500 ºC for 2 hours in air. The synthesized nanoparticles have 70% anatase and 30% rutile, resembling the phase structure of CT-500-2 with highest photoactivity among all the synthesized C-TiO_2 in previous study. With the increasing Pt or Ag content, the anatase/rutile grain growth was retarded, possibly due to the compressive strain introduced by Pt or Ag. The self-doped carbon mainly exists as graphite-like carbon or interstitial carbon in the form of carbonate species or substitutional carbon at oxygen sites to either serve as photosensitizers or effectively narrow the band gap of TiO_2, collectively enhancing the visible light photocatalytic absorption. The loaded Pt or Ag nanoparticles in their metallic states further enhanced the visible light absorption and charge carrier separation by serving as electron scavengers. The enhanced photocatalytic performance in comparison to C-TiO_2 was successfully demonstrated with the destruction of gaseous toluene in air and decomposition of Rhodamine B in aqueous suspension under visible light irradiation, which could be attributed to the synergistic effect of carbon doping and

platinum or silver modification, increasing its potential of being utilized in both air and water purification for organic pollutants removal.

CHAPTER 6 : CONCLUSION AND RECOMMENDATIONS

6.1 Conclusions

In this thesis, a simple and cost-effective process was developed for mass-production of visible light-active carbon-doped titanium dioxide (C-TiO_2) photocatalyst, specifically, by mild oxidation of TiC precursor at 350 ºC for 2-50 hours and more aggressive oxidation at higher temperature of 400-600 ºC for 2 hours in air. Based on XRD and TEM study, the synthesized C-TiO_2 nanoparticles comprised mixed anatase/rutile phases. With prolonged oxidation time or increase in oxidation temperature, the rutile content remained virtually the same at ca. 30% with prolonged oxidation at 350 ºC for up to 50 hours or increased oxidation temperature up to 500 ºC for 2 hours, resembling the phase structure of the P25 TiO_2 powder with high photoactivity. Initial decrease in crystallite size and increase in specific surface area were unveiled due to cracking of TiC grains, renucleation of TiO_2 and diffusion of carbon atoms. Once recovery and recrystallisation were completed, grain growth was observed again to further reduce the internal energy.

The states of carbon in the TiO_2 lattice upon thermal oxidation of TiC were explicitly elucidated via Raman, FTIR and XPS measurements. The doped carbon in the TiO_2 matrix was found to exist as graphite-like carbon, interstitial carbon in the form of carbonate species and substitutional carbon in the oxygen sites. The former two carbon states may serve as photosensitizers while the substitutional carbon introduces additional electronic states just above the valence band of TiO_2, directly responsible for the red shift of the absorption edge observed in the UV-vis absorption spectra. Three possible pathways for enhanced photocatalytic oxidation processes in C-TiO_2 nanoparticles were elucidated according to the proposed band structures.

Subsequently, the potential of utilizing the synthesized C-TiO_2 nanoparticles for photocatalytic environmental remediation was demonstrated by the removal of volatile organic compound (VOC) and disinfection of microorganisms. With the custom-built test system for photocatalytic evaluation on gaseous pollutants, the photocatalytic performance of C-TiO_2 in spray coated form was tested on gaseous toluene. The experimental conditions were optimized in the batch reactors with CT-500-2 as a probe photocatalyst with fixed light intensity of 10000 lux irradiating on the photocatalytic samples, 40 ppm toluene feeding gas balanced with zero air at 70% RH. C-TiO_2 synthesized at higher oxidation temperature of 400-550 ºC with shorter duration of 2 hours exhibited higher mineralization efficiency than those prepared by the conventional mild oxidation process at 350 ºC, providing a facile fabrication method for large-scale production of C-TiO_2. Among all, CT-500-2 has demonstrated the best performance by completely mineralizing 23.77 ppm of toluene within six hours, whose efficiency is even higher than the commercial C-TiO_2 Kronos vlp 7000

after normalizing to its surface area, which can be attributed to the moderate amount of doped carbon and defects states, suitable surface area, and appropriate ratio of antase/rutile phase. The performance of C-TiO_2 was also found superior to N-TiO_2 prepared with similar recipe due to production of larger red shift. Under continuous flow condition, similar trend was obtained under the irradiation of 10000 lux fluorescent light, 40 ppm toluene feeding gas, 40% RH and 50 sccm flow rate, further adding the feasibility of incorporating the C-TiO_2 photocatalysts in air conditioning system or large indoor surface area for effective air treatment. The effectiveness of C-TiO_2 was also demonstrated with the disinfection of gram-negative *E. coli* and gram-positive *E. faecalis* with different cell wall structures following the similar trend as in the case of toluene degradation, increasing the potential of utilizing C-TiO_2 in the actual water/air disinfection process with the use of only natural light.

After the optimization of the oxidation condition at 500 ºC for 2 hours, further improvement of the synthesized C-TiO_2 was achieved by co-modification with novel metals including Pt and Ag to further enhance the visible light absorption and the charge carrier separation by serving as electron scavengers. Pt/C-TiO_2 and Ag/C-TiO_2 were successfully prepared by thermal oxidation of $H_2PtCl_6 \cdot 6H_2O$ or $AgNO_3$-impregnated TiC precursor at 500 ºC for 2 hours in air for simultaneous TiO_2 formation, C doping and Pt/Ag modification in a single step. The synthesized nanopartciles consisted of 70% anatase and 30% rutile, resembling the phase structure of P25 TiO_2 and CT-500-2 with high photoactivities. The visible light photocatalytic oxidation mechanism with four pathways was proposed and the

enhanced photocatalytic performance with respect to C-TiO_2 was successfully demonstrated with the destruction of gaseous toluene in batch reactors and decomposition of Rhodamine B in aqueous suspension, which could be attributed to the synergistic effect of C doping and Pt/Ag modification, indicating its potential usage in both air and water purification with higher photocatalytic efficiency.

6.2 Recommendations

We have successfully obtained C-TiO_2 nanoparticles by thermal oxidation of TiC nanoparticles, which was proven to be an effective and facile fabrication method suitable for mass production of C-TiO_2 photocatalyst. Further improvement was also achieved by modification of C-TiO_2 with Pt/Ag to enhance the visible light absorption and charge carrier separation. Promising visible light photocatalytic performance of C-TiO_2 and Pt/Ag-C-TiO_2 was demonstrated with the mineralization of gaseous toluene in air, disinfection of microorganisms and degradation of Rhodamine B in aqueous suspension, indicating their potential usages in air/water purification/disinfection for environmental remediation. There are still many works that can be done for the further improvement of materials and integration into real applications. Some specific examples will be discussed in the following sections.

6.2.1 Material Aspect

6.2.1.1 Reducing the Particle Size of C-TiO_2

The BET surface area of the synthesized C-TiO_2 in the range of 15-45 m^2/g is far from satisfactory as compared to the 297 m^2/g measured on commercial C-TiO_2 Kronos vlp 7000. It is desirable to further increase the surface area of the synthesized C-TiO_2 to provide more active sites for adsorption of pollutants.

Pertaining to the high oxidation temperature at 500 ºC for 2 hours for the optimized synthesis of C-TiO_2 which will promote the particle size growth, it is more feasible to increase the surface area of the TiC precursor before the oxidation process. One recommended solution is by reducing the particle size of the commercial TiC precursor with high energy ball milling process [169]. Several parameters have to be optimized for the ball milling process, including the milling speed/time/cycles, type of milling bowl/balls, the weight ratio of powder to balls in the bowl, dry/wet milling conditions and gas flow condition to prevent the oxidation of TiC in ambient environment. Higher specific surface area for pollutants adsorption would be expected in the formed C-TiO_2 with smaller size TiC precursor, resulting in higher photocatalytic efficiency.

6.2.1.2 Synthesis of Pt/Ag Loaded C-TiO_2 by Photochemical Impregnation

In the present work, the Pt/Ag loaded C-TiO_2 was prepared by thermal oxidation of $H_2PtCl_6 \cdot 6H_2O$ or $AgNO_3$-impregnated TiC precursor for TiO_2 formation, C doping and Pt/Ag modification in a single step. Based on TEM observation, the Pt and Ag

nanoparticles were seen strongly anchored onto TiO_2 with an average diameter of 5-20 nm and 2-10 nm, respectively due to the high temperature oxidation at 500 ºC. It is desirable to further reduce the Pt/Ag particle size in the sub-5 nm regime at relatively high Pt/Ag loading to facilitate better charge carrier separation for more useful applications [170].

Preparation of Ag-loaded TiO_2 has been reported via photochemical impregnation method by photoreducing the $AgNO_3$-adsorbed TiO_2 surface under UV light irradiation and subsequently removing the residual ions and finally dried in vacuum oven [151]. Likewise, the Ag/Pt loaded C-TiO_2 can be synthesized by photoreducing the $H_2PtCl_6 \cdot 6H_2O$ or $AgNO_3$-impregnated C-TiO_2 under visible light irradiation. Thus, it will become a two-step procedure requiring the C-TiO_2 to be synthesized first by thermal oxidation of TiC precursor at 500 ºC for 2 hours, which may introduce process complexity yet may achieve coincidental high Pt/Ag loading, controlled size and good dispersion of the nanoparticles with higher photocatalytic efficiency.

6.2.2 Application Aspect

6.2.2.1 C-TiO_2-Coated Ceramic Tiles for Indoor Air Quality Control

Indoor air quality has become an emerging environmental issue. According to USEPA study, people spend up to 90% of their time indoors [1]. Poor indoor air quality may trigger adverse health effects including sick building syndrome, allergens and asthma [2-8]. However, increased building tightness, growing use of

synthetic materials and office equipment, and reduced ventilation for energy conservation have resulted in growth of contaminants including CO, CO_2, O_3, VOCs, air-bound particles, and microorganisms in sealed space. Therefore, improving indoor air quality is imperative, especially for Singapore with air-conditioned buildings all year round.

With the synthesized C-TiO_2 demonstrated to be effective on photocatalytic mineralization of gaseous toluene under fluorescent light irradiation, it has high potential to be utilized in indoor air quality control. One immediate product is C-TiO_2 coated ceramic tile which only requires the indoor light or natural daylight to mineralize a broad range of indoor pollutants. In the photocatalytic test on toluene, the C-TiO_2 nanoparticle suspension was spray coated onto polyester with silica as binder. To enable coating onto smoother surfaces such as ceramic tiles, it is necessary to increase the viscosity of C-TiO_2 suspension to speed up the drying process to ensure good adhesion. It should also be noted that simultaneous firing of the tiles and oxidation of TiC precursor can be in fact achieved in one single step. For the preliminary study, the spraying dispersion was prepared with 25 g/L TiC in 20 vol% colloidal silica, 20 vol% distilled water and 60 vol% Polyurethane (PU) with increased viscosity and spray coated onto a 30 cm × 30 cm ceramic tile. Figure 6-1 shows that a uniform and smooth coating black in color can be obtained after the spraying of the TiC suspension. After the firing at 500 °C in air for 2 hours, the black TiC coating turned into transparent pale yellow due to the formation of C-TiO_2 (CT-500-2), which is aesthetic-acceptable.

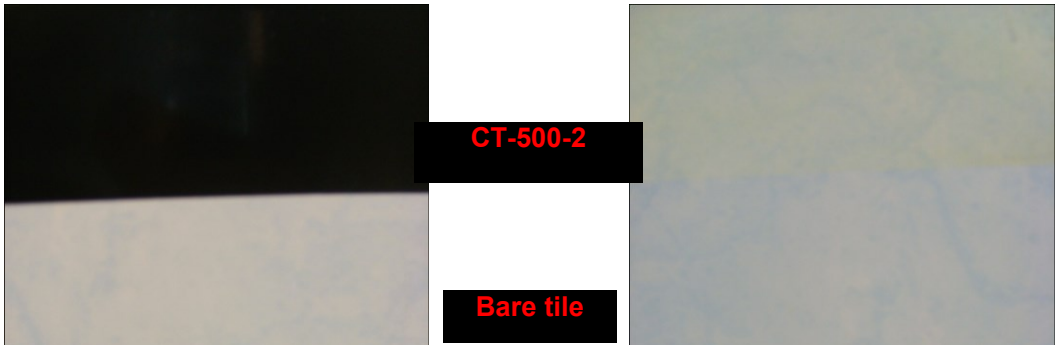

Figure 6-1. Spray coated TiC coating before (left) an after (right) thermal oxidation at 500 ºC for 2 hours.

The further improvement of the spraying dispersion can promote the successful development of the visible light-active photocatalytic tiles with antimicrobial, deodorizing, anti-pollution and possibly self-cleaning functions. The tile appears as an appropriate choice for applications in areas susceptible to higher levels of pollution such as hospitals, kitchens, and urban buildings and is anticipated to contribute to the improvement in indoor living and working environment without additional energy use.

6.2.2.2 Testing on More Pollutants

In this thesis work, the photocatalytic performance of C-TiO_2 and Pt/Ag loaded C-TiO_2 was evaluated on limited pollutants including gaseous toluene, *E. coli*, *E. faecalis*, and Rhodamine B. They should be further evaluated towards remediation of regulated and emerging contaminants of concern to prove their effectiveness on a variety of pollutants.

For air pollutants, NO_x and SO_x exhausted from automobiles have become a serious source of air pollution in urban areas. They can be converted to more environmentally benign forms, i.e., NO_3^- and SO_4^{2-} with photocatalytic technology [59]. For VOCs, besides gaseous toluene, other important pollutants including isopropanol, benzene, and formaldehyde commonly emitted from interior furnishings and construction materials are also of great concerns. Preliminary study has been carried out on comparison of mineralization of isopropanol and toluene with CT-500-2 as a probe photocatalyst in batch reactor under the same condition. As shown in Figure 6-2, upon shining of fluorescent light, the CO_2 generation in the presence of CT-500-2 is 106.0 ppm and 166.0 ppm with isopropanol and toluene as feed pollutants, respectively. Considering the carbon balance that 1 ppm of isopropanol and toluene can generate 3 ppm and 7 ppm CO_2 respectively, it is obvious that the mineralization efficiency of isopropanol is almost 50% higher than that of toluene, possibly due to the relatively robust benzene ring in toluene. Gaseous formaldehyde will be the next target pollutant with the testing protocol established on TiO_2 coated polyester filter recently [171].

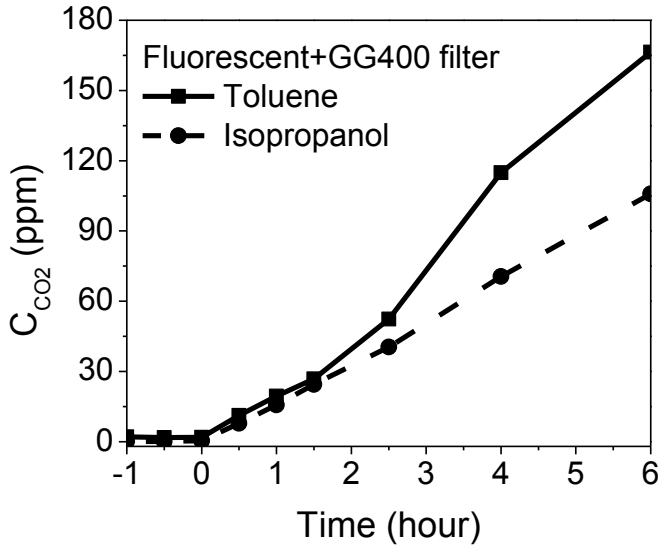

Figure 6-2. Evolution of CO_2 in the presence of CT-500-2 with toluene and 2-propanol as the feed pollutants under fluorescent light irradiation (10000 lux, 40 ppm feed concentration, 70% RH, zero air as diluting gas).

For water treatment, one interesting application is to remove endocrine disruptor chemicals (EDC) including natural hormones, dioxins, biphenol-A, etc. in the aqueous environment [59], which will be tested in School of Civil & Environmental Engineering [118]. For microorganism disinfection, collaboration with the research lab in School of Biological Sciences has been sought to further test on fungi with higher robustness than bacteria cells.

Author's Publications

Journal Papers:

1. **Li Zhang**, Man Siu Tse, Yu Xi Wang, Mandi Han, and Ooi Kiang Tan, "Facile fabrication and characterization of multi-type carbon-doped TiO_2 for visible light-activated photocatalytic mineralization of gaseous toluene", *Journal of Materials chemistry A*, vol. 1, pp. 4497 – 4507, 2013.
2. **Li Zhang**, Mandi Han, Ooi Kiang Tan, Man Siu Tse, Yu Xi Wang, and Chun Chau Sze, "Facile fabrication of Ag/C-TiO_2 nanoparticles with enhanced visible light photocatalytic activities for disinfection of *Escherichia coli* and *Enterococcus faecalis*", *Journal of Materials chemistry B*, vol. 1, pp. 564-570, 2013.
3. **Li Zhang,** Ooi Kiang Tan, Man Siu Tse, and Mandi Han "One-Step Facile Fabrication of Room-Light Active Pt/C-TiO_2 Nanoparticles with Enhanced Photocatalytic Activity" (Manuscript in preparation).
4. Zhenan Han, Victor W.C. Chang, **Li Zhang**, Man Siu Tse, Ooi Kiang Tan, and Lynn M. Hildemann, "Preparation of TiO_2-coated polyester fiber filter by spray-coating and its photocatalytic degradation of gaseous formaldehyde", *Aerosol and Air Quality Research*, vol. 12, pp. 1327-1335, 2012.

5. Zhenan Han, Victor W.C. Chang, **Li Zhang**, Man Siu Tse, Ooi Kiang Tan, and Lynn M. Hildemann, "Indoor Air Purification using TiO_2-coated polyester fiber", *Aerosol and Air Quality Research* (under review).

International Conferences:

1. **Li Zhang**, Pei Yun Tan, Tan ooi Kiang, and Tse Man Siu, "Visible light photocatalytic decontamination of gas-phase toluene with spray-coated $TiO_{2-x}N_x$", 15th International Congress on Catalysis 2012 (ICC-2012), Munich, Germany, 1-6 July 2012 [Oral].
2. **Li Zhang**, Ooi Kiang Tan, and Man Siu Tse, "C-doped TiO_2 by thermal oxidation of TiC: synthesis, characterization and photocatalytic evaluation on gaseous toluene under fluorescent light irradiation", International Conference on Young Researchers on Advanced Materials (ICRAM-2012), Singapore, 1-6 Jul 2012.
3. **Li Zhang**, Man Siu Tse, Pei Yun Tan, and Ooi Kiang Tan, "Visible light photocatalytic oxidation of gas-phase 2-propanol with spray-coated N-TiO_2 on polyester filters", 5th MRS-S Conference on Advanced Materials, Singapore, 20-22 Mar 2012.
4. **Li Zhang**, Pei Yun Tan, Ooi Kiang Tan, Chun Chau Sze, and, Man Siu Tse, "Anti-microbial activities of $Sr(Ti_{1-x}Fe_x)O_{3-\delta}$: a case study on *Escherichia coli* as a probe bacterium" 17th International Conference on. Advanced Oxidation Technologies for Treatment of Water, Air and Soil (AOTs-17), San Diego, USA, 7-10 Nov 2011 [Oral].

5. Pei Yun Tan, Qiong Luo, Ooi Kiang Tan, Man Siu Tse, Xiaoqin Fang, **Li Zhang**, Mohammad Ghaffari, "Nitrogen-doped TiO_2 for visible-light photocatalytic applications prepared by oxidation of titanium nitride", 16th International Conference on TiO_2 Photocatalysis: Fundamentals and Applications (TiO_2-16**),** San Diego, USA, 7-10 Nov 2011.
6. **Li Zhang**, Man Siu Tse, and Ooi Kiang Tan, "Visible light photocatalytic oxidation of gas-phase toluene with spray-coated C-doped TiO_2 on polyester filters", International Union of Materials Research Societies and International Conference in Asia (IUMRS-ICA), Taipei, Taiwan, 19-22 Sep 2011.
7. **Li Zhang**, Ying Hu, Ooi Kiang Tan, and Pei Yun Tan, "Novel nano-structured material for indoor air quality control", Singapore, 3rd MRS-S Conference on Advanced Materials, 25-27 Feb 2008.

Bibliography

[1] A. Fujishima and K. Honda, "Electrochemical Photolysis of Water at a Semiconductor Electrode," *Nature,* vol. 238, pp. 37-38, 1972.

[2] T. Bak, J. Nowotny, M. Rekas, and C. C. Sorrell, "Photo-electrochemical hydrogen generation from water using solar energy. Materials-related aspects," *International Journal of Hydrogen Energy,* vol. 27, pp. 991-1022, 2002.

[3] O. Carp, C. L. Huisman, and A. Reller, "Photoinduced reactivity of titanium dioxide," *Progress in Solid State Chemistry,* vol. 32, pp. 33-177, 2004.

[4] M. Gagliardi, "Photocatalysts: Technologies and Global Markets," BCC Research (AVM069A) 2010.

[5] Y. Zhang, *Indoor Air Quality Engineering*: CRC Press, 2004.

[6] N. de Nevers, *Air Pollution Control Engineering*, Second ed.: McGraw Hill, 2000.

[7] R. H. D. a. D. W. Andrew Mills, "Water purification by semiconductor photocatalysis," *Chemical Society Review,* vol. 22, p. 417, 1993.

[8] J. Mo, Y. Zhang, Q. Xu, J. J. Lamson, and R. Zhao, "Photocatalytic purification of volatile organic compounds in indoor air: A literature review," *Atmospheric Environment,* vol. 43, pp. 2229-2246, 2009.

[9] D. Chatterjee and A. Mahata, "Photoassisted detoxification of organic pollutants on the surface modified TiO_2 semiconductor particulate system," *Catalysis Communications,* vol. 2, pp. 1-3, 2001.

[10] J. Moon, C. Y. Yun, K. W. Chung, M. S. Kang, and J. Yi, "Photocatalytic activation of TiO_2 under visible light using Acid Red 44," *Catalysis Today,* vol. 87, pp. 77-86, 2003.

[11] D. Chatterjee and A. Mahata, "Visible light induced photodegradation of organic pollutants on dye adsorbed TiO_2 surface," *Journal of Photochemistry and Photobiology A: Chemistry,* vol. 153, pp. 199-204, 2002.

[12] L. Song, R. Qiu, Y. Mo, D. Zhang, H. Wei, and Y. Xiong, "Photodegradation of phenol in a polymer-modified TiO_2 semiconductor particulate system under the irradiation of visible light," *Catalysis Communications,* vol. 8, pp. 429-433, 2007.

[13] R. Qiu, D. Zhang, Y. Mo, L. Song, E. Brewer, X. Huang, and Y. Xiong, "Photocatalytic activity of polymer-modified ZnO under visible light irradiation," *Journal of Hazardous Materials,* vol. 156, pp. 80-85, 2008.

[14] L. Wu, J. C. Yu, and X. Fu, "Characterization and photocatalytic mechanism of nanosized CdS coupled TiO_2 nanocrystals under visible light irradiation," *Journal of Molecular Catalysis A: Chemical,* vol. 244, pp. 25-32, 2006.

[15] J. Liu, R. Yang, and S. Li, "Preparation and characterization of the TiO_2-V_2O_5 photocatalyst with visible-light activity," *Rare Metals,* vol. 25, pp. 636-642, 2006.

[16] Y. Bessekhouad, D. Robert, and J. V. Weber, "Bi_2S_3/TiO_2 and CdS/TiO_2 heterojunctions as an available configuration for photocatalytic degradation of organic pollutant," *Journal of Photochemistry and Photobiology A: Chemistry,* vol. 163, pp. 569-580, 2004.

[17] W. Ho and J. C. Yu, "Sonochemical synthesis and visible light photocatalytic behavior of CdSe and $CdSe/TiO_2$ nanoparticles," *Journal of Molecular Catalysis A: Chemical,* vol. 247, pp. 268-274, 2006.

[18] I. Nakamura, N. Negishi, S. Kutsuna, T. Ihara, S. Sugihara, and K. Takeuchi, "Role of oxygen vacancy in the plasma-treated TiO_2 photocatalyst with visible light activity for NO removal," *Journal of Molecular Catalysis A: Chemical,* vol. 161, pp. 205-212, 2000.

[19] T. Ihara, M. Miyoshi, Y. Iriyama, O. Matsumoto, and S. Sugihara, "Visible-light-active titanium oxide photocatalyst realized by an oxygen-deficient structure and by nitrogen doping," *Applied Catalysis B: Environmental,* vol. 42, pp. 403-409, 2003.

[20] P. Bouras, E. Stathatos, and P. Lianos, "Pure versus metal-ion-doped nanocrystalline titania for photocatalysis," *Applied Catalysis B: Environmental,* vol. 73, pp. 51-59, 2007.

[21] Herrmann, Jean-Marie, J. Disdier, and P. Pichat, "Effect of chromium doping on the electrical and catalytic properties of powder titania under UV and visible illumination," *Chemical Physics Letters,* vol. 108, pp. 618-622, 1984.

[22] K. Sunada, T. Watanabe, and K. Hashimoto, "Bactericidal Activity of Copper-Deposited TiO_2 Thin Film under Weak UV Light Illumination," *Environmental Science & Technology,* vol. 37, pp. 4785-4789, 2003.

[23] H. Yamashita, Y. Ichihashi, M. Takeuchi, S. Kishiguchi, and M. Anpo, "Characterization of metal ion-implanted titanium oxide photocatalysts operating under visible light irradiation," *Journal of Synchrotron Radiation,* vol. 6, pp. 451-452, 1999.

[24] R. Asahi, T. Morikawa, T. Ohwaki, K. Aoki, and Y. Taga, "Visible-light photocatalysis in nitrogen-doped titanium oxides," *Science,* vol. 293, pp. 269-271, 2001.

[25] Yoshio Nosaka, Masami Matsushita, Junichi Nishino, and Atsuko Y. Nosaka, "Nitrogen-doped titanium dioxide photocatalysts for visible response prepared by using organic compounds," *Science and Technology of Advanced Materials,* vol. 6, pp. 143-148, 2005.

[26] J. C. Yu, W. Ho, J. Yu, H. Yip, P. K. Wong, and J. Zhao, "Efficient Visible-Light-Induced Photocatalytic Disinfection on Sulfur-Doped Nanocrystalline Titania," *Environmental Science & Technology,* vol. 39, pp. 1175-1179, 2005.

[27] H. Irie, S. Washizuka, and K. Hashimoto, "Hydrophilicity on carbon-doped TiO_2 thin films under visible light," *Thin Solid Films,* vol. 510, pp. 21-25, 2006.

[28] H. Wang and J. P. Lewis, "Second-generation photocatalytic materials: anion-doped TiO_2," *Journal of Physics: Condensed Matter,* vol. 18, p. 421, 2006.

[29] Z. Lei, W. You, M. Liu, G. Zhou, T. Takata, M. Hara, K. Domen, and C. Li, "Photocatalytic water reduction under visible light on a novel $ZnIn_2S_4$ catalyst synthesized by hydrothermal method," *Chemical Communications,* pp. 2142-2143, 2003.

[30] I. M. Szilágyi, B. Fórizs, O. Rosseler, Á. Szegedi, P. Németh, P. Király, G. Tárkányi, B. Vajna, K. Varga-Josepovits, K. László, A. L. Tóth, P. Baranyai, and M. Leskelä, "WO_3 photocatalysts: Influence of structure and composition," *Journal of Catalysis,* vol. 294, pp. 119-127, 2012.

[31] D. Jing and L. Guo, "A Novel Method for the Preparation of a Highly Stable and Active CdS Photocatalyst with a Special Surface Nanostructure," *The Journal of Physical Chemistry B,* vol. 110, pp. 11139-11145, 2006.

[32] J. S. Jang, J. Lee, H. Ye, F.-R. F. Fan, and A. J. Bard, "Rapid Screening of Effective Dopants for Fe_2O_3 Photocatalysts with Scanning Electrochemical Microscopy and Investigation of Their Photoelectrochemical Properties," *The Journal of Physical Chemistry C,* vol. 113, pp. 6719-6724, 2009.

[33] L. Ge, "Novel visible-light-driven Pt/$BiVO_4$ photocatalyst for efficient degradation of methyl orange," *Journal of Molecular Catalysis A: Chemical,* vol. 282, pp. 62-66, 2008.

[34] M. Pelaez, N. T. Nolan, S. C. Pillai, M. K. Seery, P. Falaras, A. G. Kontos, P. S. M. Dunlop, J. W. J. Hamilton, J. A. Byrne, K. O'Shea, M. H. Entezari, and D. D. Dionysiou, "A review on the visible light active titanium dioxide photocatalysts for environmental applications," *Applied Catalysis B: Environmental,* vol. 125, pp. 331-349, 2012.

[35] D. Wang, Z.-H. Zhou, H. Yang, K.-B. Shen, Y. Huang, and S. Shen, "Preparation of TiO_2 loaded with crystalline nano Ag by a one-step low-temperature hydrothermal method," *Journal of Materials Chemistry,* vol. 22, pp. 16306-16311, 2012.

[36] H. Zhang and G. Chen, "Potent Antibacterial Activities of Ag/TiO_2 Nanocomposite Powders Synthesized by a One-Pot Sol−Gel Method," *Environmental Science & Technology,* vol. 43, pp. 2905-2910, 2009.

[37] L. Zhang, M. Han, O. K. Tan, M. S. Tse, Y. X. Wang, and C. C. Sze, "Facile fabrication of Ag/C-TiO_2 nanoparticles with enhanced visible light photocatalytic activity for disinfection of *Escherichia coli* and *Enterococcus faecalis*," *Journal of Materials Chemistry B,* vol. 1, pp. 564-570, 2013.

[38] John H. Carey, John Lawrence, and H. M. Tosine, "Photodechlorination of PCB's in the presence of titanium dioxide in aqueous suspensions," *Bulletin of Environmental Contamination and Toxicology,* vol. 16, pp. 697-701, 1976.

[39] S. N. Frank and A. J. Bard, "Heterogeneous photocatalytic oxidation of cyanide ion in aqueous solutions at titanium dioxide powder," *Journal of the American Chemical Society,* vol. 99, pp. 303-304, 1977.

[40] S. N. Frank and A. J. Bard, "Heterogeneous photocatalytic oxidation of cyanide and sulfite in aqueous solutions at semiconductor powders," *The Journal of Physical Chemistry,* vol. 81, pp. 1484-1488, 1977.

[41] M. A. Fox and M. T. Dulay, "Heterogeneous photocatalysis," *Chemical Reviews,* vol. 93, pp. 341-357, 1993.

[42] M. R. Hoffmann, S. T. Martin, W. Choi, and D. W. Bahnemann, "Environmental Applications of Semiconductor Photocatalysis," *Chemical Reviews,* vol. 95, pp. 69-96, 1995.

[43] H. A.-E. D. F. Ollis, Ed., *Photocatalytic Purification and Treatment of Water and Air*: Amsterdam: Elsevier, 1993.

[44] M. Hara, G. Hitoki, T. Takata, J. N. Kondo, H. Kobayashi, and K. Domen, "TaON and Ta3N5 as new visible light driven photocatalysts," *Catalysis Today,* vol. 78, pp. 555-560, 2003.

[45] S. E. Braslavsky, "Glossary of terms used in photochemistry, 3rd edition," *Pure and Applied Chemistry,* vol. 79, pp. 293-465, 2007.

[46] A. Mills and S. Le Hunte, "An overview of semiconductor photocatalysis," *Journal of Photochemistry and Photobiology A: Chemistry,* vol. 108, pp. 1-35, 1997.

[47] A. J. Hoffman, E. R. Carraway, and M. R. Hoffmann, "Photocatalytic Production of H_2O_2 and Organic Peroxides on Quantum-Sized Semiconductor Colloids," *Environmental Science & Technology,* vol. 28, pp. 776-785, 1994.

[48] U. I. Gaya and A. H. Abdullah, "Heterogeneous photocatalytic degradation of organic contaminants over titanium dioxide: A review of fundamentals, progress and problems," *Journal of Photochemistry and Photobiology C: Photochemistry Reviews,* vol. 9, pp. 1-12, 2008.

[49] U. Diebold, "The surface science of titanium dioxide," *Surface Science Reports,* vol. 48, pp. 53-229, 2003.

[50] Y. Hu, H. L. Tsai, and C. L. Huang, "Effect of brookite phase on the anatase–rutile transition in titania nanoparticles," *Journal of the European Ceramic Society,* vol. 23, pp. 691-696, 2003.

[51] N. Serpone, "Is the Band Gap of Pristine TiO_2 Narrowed by Anion- and Cation-Doping of Titanium Dioxide in Second-Generation Photocatalysts?," *The Journal of Physical Chemistry B,* vol. 110, pp. 24287-24293, 2006.

[52] R. Qiu, D. Zhang, Y. Mo, L. Song, E. Brewer, X. Huang, and Y. Xiong, "Photocatalytic activity of polymer-modified ZnO under visible light irradiation," *Journal of Hazardous Materials,* vol. 156, pp. 80-85, 2008.

[53] R. Abe, K. Hara, K. Sayama, K. Domen, and H. Arakawa, "Steady hydrogen evolution from water on Eosin Y-fixed TiO_2 photocatalyst using a silane-coupling reagent under visible light irradiation," *Journal of Photochemistry and Photobiology A: Chemistry,* vol. 137, pp. 63-69, 2000.

[54] K. Vinodgopal, X. Hua, R. L. Dahlgren, A. G. Lappin, L. K. Patterson, and P. V. Kamat, "Photochemistry of $Ru(bpy)_2(dcbpy)^{2+}$ on Al_2O_3 and TiO_2 Surfaces. An Insight into the

Mechanism of Photosensitization," *The Journal of Physical Chemistry,* vol. 99, pp. 10883-10889, 1995.

[55] W. Zhongbiao, D. Fan, Z. Weirong, W. Haiqiang, L. Yue, and G. Baohong, "The fabrication and characterization of novel carbon doped TiO_2 nanotubes, nanowires and nanorods with high visible light photocatalytic activity," *Nanotechnology,* vol. 20, p. 235701, 2009.

[56] S. Sato, "Photocatalytic activity of NO_x-doped TiO_2 in the visible light region," *Chemical Physics Letters,* vol. 123, p. 126, 1986.

[57] Z. Lin, A. Orlov, R. M. Lambert, and M. C. Payne, "New Insights into the Origin of Visible Light Photocatalytic Activity of Nitrogen-Doped and Oxygen-Deficient Anatase TiO_2," *The Journal of Physical Chemistry B,* vol. 109, pp. 20948-20952, 2005.

[58] T. Tachikawa, S. Tojo, K. Kawai, M. Endo, M. Fujitsuka, T. Ohno, K. Nishijima, Z. Miyamoto, and T. Majima, "Photocatalytic Oxidation Reactivity of Holes in the Sulfur- and Carbon-Doped TiO_2 Powders Studied by Time-Resolved Diffuse Reflectance Spectroscopy," *The Journal of Physical Chemistry B,* vol. 108, pp. 19299-19306, 2004.

[59] A. Fujishima, X. Zhang, and D. A. Tryk, "TiO_2 photocatalysis and related surface phenomena," *Surface Science Reports,* vol. 63, pp. 515-582, 2008.

[60] H. K. Jürgen Orth-Gerber, "Titanium dioxide photocatalyst containing carbon and method for its production," 2009.

[61] P. Zabek, J. Eberl, and H. Kisch, "On the origin of visible light activity in carbon-modified titania," *Photochemical & Photobiological Sciences,* vol. 8, pp. 264-269, 2009.

[62] X. Wang, S. Meng, X. Zhang, H. Wang, W. Zhong, and Q. Du, "Multi-type carbon doping of TiO_2 photocatalyst," *Chemical Physics Letters,* vol. 444, pp. 292-296, 2007.

[63] S. U. M. Khan, M. Al-Shahry, and W. B. Ingler, "Efficient Photochemical Water Splitting by a Chemically Modified n-TiO_2," *Science,* vol. 297, pp. 2243-2245, 2002.

[64] J. H. Park, S. Kim, and A. J. Bard, "Novel Carbon-Doped TiO_2 Nanotube Arrays with High Aspect Ratios for Efficient Solar Water Splitting," *Nano Letters,* vol. 6, pp. 24-28, 2006.

[65] H. Irie, Y. Watanabe, and K. Hashimoto, "Carbon-doped Anatase TiO_2 Powders as a Visible-light Sensitive Photocatalyst," *Chemistry Letters,* vol. 32, pp. 772-773, 2003.

[66] Y. Choi, T. Umebayashi, S. Yamamoto, and S. Tanaka, "Fabrication of TiO_2 photocatalysts by oxidative annealing of TiC," *Journal of Materials Science Letters,* vol. 22, pp. 1209-1211, 2003.

[67] Y. Choi, T. Umebayashi, and M. Yoshikawa, "Fabrication and characterization of C-doped anatase TiO_2 photocatalysts," *Journal of Materials Science,* vol. 39, pp. 1837-1839, 2004.

[68] M. Shen, Z. Wu, H. Huang, Y. Du, Z. Zou, and P. Yang, "Carbon-doped anatase TiO_2 obtained from TiC for photocatalysis under visible light irradiation," *Materials Letters,* vol. 60, pp. 693-697, 2006.

[69] H. Liu, A. Imanishi, and Y. Nakato, "Mechanisms for Photooxidation Reactions of Water and Organic Compounds on Carbon-Doped Titanium Dioxide, as Studied by Photocurrent Measurements," *The Journal of Physical Chemistry C,* vol. 111, pp. 8603-8610, 2007.

[70] H. He, C. Liu, K. D. Dubois, T. Jin, M. E. Louis, and G. Li, "Enhanced Charge Separation in Nanostructured TiO_2 Materials for Photocatalytic and Photovoltaic Applications," *Industrial & Engineering Chemistry Research,* vol. 51, pp. 11841-11849, 2012.

[71] K. Hess-Kosa, *Indoor Air Quality: Sampling Methodologies*: CRC Press, 2001.

[72] H. Liu, Z. Lian, X. Ye, and W. Shangguan, "Kinetic analysis of photocatalytic oxidation of gas-phase formaldehyde over titanium dioxide," *Chemosphere,* vol. 60, pp. 630-635, 2005.

[73] C. H. Ao, S. C. Lee, J. Z. Yu, and J. H. Xu, "Photodegradation of formaldehyde by photocatalyst TiO2: effects on the presences of NO, SO_2 and VOCs," *Applied Catalysis B: Environmental,* vol. 54, pp. 41-50, 2004.

[74] X. Ye, D. Chen, J. Gossage, and K. Li, "Photocatalytic oxidation of aldehydes: Byproduct identification and reaction pathway," *Journal of Photochemistry and Photobiology A: Chemistry,* vol. 183, pp. 35-40, 2006.

[75] O. d'Hennezel, P. Pichat, and D. F. Ollis, "Benzene and toluene gas-phase photocatalytic degradation over H_2O and HCL pretreated TiO_2: by-products and mechanisms," *Journal of Photochemistry and Photobiology A: Chemistry,* vol. 118, pp. 197-204, 1998.

[76] S. A. Larson, J. A. Widegren, and J. L. Falconer, "Transient Studies of 2-Propanol Photocatalytic Oxidation on Titania," *Journal of Catalysis,* vol. 157, pp. 611-625, 1995.

[77] H. V. Raillard C, Le Cloirec P, and Legrand J., "Photocatalytic oxidation of methyl ethyl ketone over sol-gel and commercial TiO_2 for the improvement of indoor air," *Water Science and Technology,* vol. 53, pp. 107-115, 2006.

[78] G. Vincent, P. M. Marquaire, and O. Zahraa, "Abatement of volatile organic compounds using an annular photocatalytic reactor: Study of gaseous acetone," *Journal of Photochemistry and Photobiology A: Chemistry,* vol. 197, pp. 177-189, 2008.

[79] F. Chen, X. Yang, H. K. C. Mak, and D. W. T. Chan, "Photocatalytic oxidation for antimicrobial control in built environment: A brief literature overview," *Building and Environment,* vol. 45, pp. 1747-1754, 2010.

[80] T. Matsunaga, R. Tomada, T. Nakajima, and H. Wake, "Photoelectrochemical sterilization of microbial cells by semiconductor powders," *FEMS Microbiology Letters,* vol. 29, pp. 211-214, 1985.

[81] W. A. Jacoby, P. C. Maness, E. J. Wolfrum, D. M. Blake, and J. A. Fennell, "Mineralization of bacterial cell mass on a photocatalytic surface in air," *Environmental Science & Technology,* vol. 32, pp. 2650-2653, 1998.

[82] K. Sunada, Y. Kikuchi, K. Hashimoto, and A. Fujishima, "Bactericidal and detoxification effects of TiO_2 thin film photocatalysts," *Environmental Science & Technology,* vol. 32, pp. 726-728, 1998.

[83] R. J. Watts, S. Kong, M. P. Orr, G. C. Miller, and B. E. Henry, "Photocatalytic inactivation of coliform bacteria and viruses in secondary wastewater effluent," *Water Research,* vol. 29, pp. 95-100, 1995.

[84] B. J. P. A. Cornish, L. A. Lawton, and P. K. J. Robertson, "Hydrogen peroxide enhanced photocatalytic oxidation of microcystin-LR using titanium dioxide," *Applied Catalysis B: Environmental,* vol. 25, pp. 59-67, 2000.

[85] C. Sichel, J. Tello, M. de Cara, and P. Fernández-Ibáñez, "Effect of UV solar intensity and dose on the photocatalytic disinfection of bacteria and fungi," *Catalysis Today,* vol. 129, pp. 152-160, 2007.

[86] A. H. Sakai, R. X. Cai, T. Yoshioka, Y. Kubota, K. Hashimoto, and A. Fujishima, "Intracellular Ca^{2+} concentration change of T24 cell under irradiation in the presence of TiO_2 ultrafine particles," *Biochimica et Biophysica Acta (BBA) - General Subjects,* vol. 1201, pp. 259-265, 1994.

[87] N. G. Park, J. van de Lagemaat, and A. J. Frank, "Comparison of Dye-Sensitized Rutile- and Anatase-Based TiO_2 Solar Cells," *The Journal of Physical Chemistry B,* vol. 104, pp. 8989-8994, 2000.

[88] P. C. M. Zheng Huang, Daniel M. Blake, Edward J. Wolfrum, and Sharon L. Smolinski, "Bactericidal Mode of Titanium Dioxide Photocatalysis," *Journal of Photochemistry and Photobiology A: Chemistry,* vol. 130, pp. 163-170, 2000.

[89] T. Saito, T. Iwase, J. Horie, and T. Morioka, "Mode of photocatalytic bactericidal action of powdered semiconductor TiO_2 on mutans streptococci," *Journal of Photochemistry and Photobiology B: Biology,* vol. 14, pp. 369-379, 1992.

[90] K. Sunada, T. Watanabe, and K. Hashimoto, "Studies on photokilling of bacteria on TiO2 thin film," *Journal of Photochemistry and Photobiology A: Chemistry,* vol. 156, pp. 227-233, 2003.

[91] S. Shimada, "A thermoanalytical study of oxidation of TiC by simultaneous TGA-DTA-MS analysis," *Journal of Materials Science,* vol. 31, pp. 673-677, 1996.

[92] K. K. Bando, K. Sayama, H. Kusama, K. Okabe, and H. Arakawa, "In-situ FT-IR study on CO_2 hydrogenation over Cu catalysts supported on SiO_2, Al_2O_3, and TiO_2," *Applied Catalysis A: General,* vol. 165, pp. 391-409, 1997.

[93] L. Zhang and R. V. Koka, "A study on the oxidation and carbon diffusion of TiC in alumina–titanium carbide ceramics using XPS and Raman spectroscopy," *Materials Chemistry and Physics,* vol. 57, pp. 23-32, 1998.

[94] D. C. Hurum, A. G. Agrios, K. A. Gray, T. Rajh, and M. C. Thurnauer, "Explaining the Enhanced Photocatalytic Activity of Degussa P25 Mixed-Phase TiO_2 Using EPR," *The Journal of Physical Chemistry B,* vol. 107, pp. 4545-4549, 2003.

[95] I. L. Shabalin, D. L. Roach, and L. I. Shabalin, "Oxidation of titanium carbide–graphite hetero-modulus ceramics with low carbon content: II. Physico-chemical interpretation of the ridge effect," *Journal of the European Ceramic Society,* vol. 28, pp. 3177-3188, 2008.

[96] T. Ohsaka, F. Izumi, and Y. Fujiki, "Raman spectrum of anatase, TiO_2," *Journal of Raman Spectroscopy,* vol. 7, pp. 321-324, 1978.

[97] X. Xue, W. Ji, Z. Mao, H. Mao, Y. Wang, X. Wang, W. Ruan, B. Zhao, and J. R. Lombardi, "Raman Investigation of Nanosized TiO_2: Effect of Crystallite Size and Quantum Confinement," *The Journal of Physical Chemistry C,* vol. 116, pp. 8792-8797, 2012.

[98] A. C. Ferrari and J. Robertson, "Interpretation of Raman spectra of disordered and amorphous carbon," *Phys. Rev. B,* vol. 61, pp. 14095-14107, 2000.

[99] C. Chen, M. Long, H. Zeng, W. Cai, B. Zhou, J. Zhang, Y. Wu, D. Ding, and D. Wu, "Preparation, characterization and visible-light activity of carbon modified TiO_2 with two kinds of carbonaceous species," *Journal of Molecular Catalysis A: Chemical,* vol. 314, pp. 35-41, 2009.

[100] K. Keis, E. Magnusson, H. Lindström, S.-E. Lindquist, and A. Hagfeldt, "A 5% efficient photoelectrochemical solar cell based on nanostructured ZnO electrodes," *Solar Energy Materials and Solar Cells,* vol. 73, pp. 51-58, 2002.

[101] L.-W. Zhang, H.-B. Fu, and Y.-F. Zhu, "Efficient TiO_2 Photocatalysts from Surface Hybridization of TiO_2 Particles with Graphite-like Carbon," *Advanced Functional Materials,* vol. 18, pp. 2180-2189, 2008.

[102] S. Wang, H. M. Ang, and M. O. Tade, "Volatile organic compounds in indoor environment and photocatalytic oxidation: State of the art," *Environment International,* vol. 33, pp. 694-705, 2007.

[103] S.-B. Li, W.-H. Xiang, H.-X. Zhai, and Y. Zhou, "Formation of TiC hexagonal platelets and their growth mechanism," *Powder Technology,* vol. 185, pp. 49-53, 2008.

[104] F. J. M. Rietmeijer, "Mixed layering in disordered Sri Lanka graphite," *Carbon,* vol. 29, pp. 669-675, 1991.

[105] A. J. Maira, J. M. Coronado, V. Augugliaro, K. L. Yeung, J. C. Conesa, and J. Soria, "Fourier Transform Infrared Study of the Performance of Nanostructured TiO_2 Particles for the Photocatalytic Oxidation of Gaseous Toluene," *Journal of Catalysis,* vol. 202, pp. 413-420, 2001.

[106] C. Morterra, "An infrared spectroscopic study of anatase properties. Part 6.-Surface hydration and strong Lewis acidity of pure and sulphate-doped preparations," *Journal of the Chemical Society, Faraday Transactions 1: Physical Chemistry in Condensed Phases,* vol. 84, pp. 1617-1637, 1988.

[107] Y. Irokawa, T. Morikawa, K. Aoki, S. Kosaka, T. Ohwaki, and Y. Taga, "Photodegradation of toluene over $TiO_{2-x}N_x$ under visible light irradiation," *Phys. Chem. Chem. Phys.,* vol. 8, pp. 1116-1121, 2006.

[108] P. Xu, T. Xu, J. Lu, S. Gao, N. S. Hosmane, B. Huang, Y. Dai, and Y. Wang, "Visible-light-driven photocatalytic S- and C- codoped meso/nanoporous TiO_2," *Energy & Environmental Science,* vol. 3, pp. 1128-1134, 2010.

[109] Y. Zhang and C. Pan, "TiO_2/graphene composite from thermal reaction of graphene oxide and its photocatalytic activity in visible light," *Journal of Materials Science,* vol. 46, pp. 2622-2626, 2011.

[110] R. Sui, A. S. Rizkalla, and P. A. Charpentier, "FTIR Study on the Formation of TiO2 Nanostructures in Supercritical CO2," *The Journal of Physical Chemistry B,* vol. 110, pp. 16212-16218, 2006.

[111] S. Doeuff, M. Henry, C. Sanchez, and J. Livage, "Hydrolysis of titanium alkoxides: Modification of the molecular precursor by acetic acid," *Journal of Non-Crystalline Solids,* vol. 89, pp. 206-216, 1987.

[112] G. Ramis, G. Busca, and V. Lorenzelli, "Low-temperature CO_2 adsorption on metal oxides: spectroscopic characterization of some weakly adsorbed species," *Mater. Chem. Phys. ,* vol. 29, pp. 425-435, 1991.

[113] I.-C. Kang, Q. Zhang, S. Yin, T. Sato, and F. Saito, "Preparation of a visible sensitive carbon doped TiO_2 photo-catalyst by grinding TiO_2 with ethanol and heating treatment," *Appl. Catal., B* vol. 80, pp. 81-87, 2008.

[114] E. McCafferty and J. P. Wightman, "An X-ray photoelectron spectroscopy sputter profile study of the native air-formed oxide film on titanium," *Applied Surface Science,* vol. 143, pp. 92-100, 1999.

[115] J. Shi, J. Chen, Z. Feng, T. Chen, Y. Lian, X. Wang, and C. Li, "Photoluminescence Characteristics of TiO_2 and Their Relationship to the Photoassisted Reaction of Water/Methanol Mixture," *The Journal of Physical Chemistry C,* vol. 111, pp. 693-699, 2006.

[116] C. Di Valentin, G. Pacchioni, and A. Selloni, "Theory of Carbon Doping of Titanium Dioxide," *Chem. Mater.,* vol. 17, pp. 6656-6665, 2005.

[117] A. Fujishima, T. N. Rao, and D. A. Tryk, "Titanium dioxide photocatalysis," *Journal of Photochemistry and Photobiology C,* vol. 1, pp. 1-21, 2000.

[118] X. Wang, Y. Tang, M.-Y. Leiw, and T.-T. Lim, "Solvothermal synthesis of Fe–C codoped TiO_2 nanoparticles for visible-light photocatalytic removal of emerging organic contaminants in water," *Applied Catalysis A: General,* vol. 409–410, pp. 257-266, 2011.

[119] D. Fan, Z. Weirong, and W. Zhongbiao, "Characterization and photocatalytic activities of C, N and S co-doped TiO 2 with 1D nanostructure prepared by the nano-confinement effect," *Nanotechnology,* vol. 19, p. 365607, 2008.

[120] C. Di Valentin, G. Pacchioni, and A. Selloni, "Theory of Carbon Doping of Titanium Dioxide," *Chemistry of Materials,* vol. 17, pp. 6656-6665, 2005.

[121] P. N. Hathaway GJ, Hughes JP, and Fischman ML, *Proctor and Hughes' chemical hazards of the workplace*, 5th ed. New York: John Wiley & Sons 2004.

[122] X. Fu, W. A. Zeltner, and M. A. Anderson, "The gas-phase photocatalytic mineralization of benzene on porous titania-based catalysts," *Applied Catalysis B: Environmental,* vol. 6, pp. 209-224, 1995.

[123] X. Fu, X. Wang, Z. Ding, D. Y. C. Leung, Z. Zhang, J. Long, W. Zhang, Z. Li, and X. Fu, "Hydroxide $ZnSn(OH)_6$: A promising new photocatalyst for benzene degradation," *Applied Catalysis B: Environmental,* vol. 91, pp. 67-72, 2009.

[124] W. Wang, L.-W. Chiang, and Y. Ku, "Decomposition of benzene in air streams by UV/TiO_2 process," *Journal of Hazardous Materials,* vol. 101, pp. 133-146, 2003.

[125] F. B. Li, X. Z. Li, C. H. Ao, S. C. Lee, and M. F. Hou, "Enhanced photocatalytic degradation of VOCs using Ln^{3+}-TiO_2 catalysts for indoor air purification," *Chemosphere,* vol. 59, pp. 787-800, 2005.

[126] L. Sun, G. Li, S. Wan, and T. An, "Mechanistic study and mutagenicity assessment of intermediates in photocatalytic degradation of gaseous toluene," *Chemosphere,* vol. 78, pp. 313-318, 2010.

[127] A. J. Maira, K. L. Yeung, J. Soria, J. M. Coronado, C. Belver, C. Y. Lee, and V. Augugliaro, "Gas-phase photo-oxidation of toluene using nanometer-size TiO2 catalysts," *Applied Catalysis B: Environmental,* vol. 29, pp. 327-336, 2001.

[128] F. Bosc, D. Edwards, N. Keller, V. Keller, and A. Ayral, "Mesoporous TiO2-based photocatalysts for UV and visible light gas-phase toluene degradation," *Thin Solid Films,* vol. 495, pp. 272-279, 2006.

[129] M. Keshmiri, T. Troczynski, and M. Mohseni, "Oxidation of gas phase trichloroethylene and toluene using composite sol-gel TiO2 photocatalytic coatings," *Journal of Hazardous Materials,* vol. 128, pp. 130-137, 2006.

[130] ATSDR, "Toxicological Profile for Toluene," ed. Atlanta: U.S. Public Health Service, U.S. Department of Health and Human Services, 2000.

[131] NIOSH, "NIOSH Pocket Guide to Chemical Hazards (Publication No. 2005-149)," 2nd ed. Atlanta, 2005.

[132] "Fine ceramics (advanced ceramics, advanced technical ceramics)-Test method for air-purfication performacne of semiconducting photocatalytic materials-Part 1: Removal of nitric oxide," ed. Switzerland: ISO, 2007.

[133] "Fine Ceramics (advanced ceramics, advanced technical ceramics)-Test method for air purification performance of photocatalytic materials-Part 2:Removal of acetaldehyde," ed: Japanese Standards Association, 2008.

[134] "Fine Ceramics (advanced ceramics, advanced technical ceramics)-Test method for air purification performance of photocatalytic materials-Part 3:Removal of toluene," ed: Japanese Standards Association, 2009.

[135] O. Debono, F. Thevenet, P. Gravejat, V. Hequet, C. Raillard, L. Lecoq, and N. Locoge, "Toluene photocatalytic oxidation at ppbv levels: Kinetic investigation and carbon balance determination," *Appl. Catal., B,* vol. 106, pp. 600-608, 2011.

[136] A. Sclafani and J. M. Herrmann, "Comparison of the Photoelectronic and Photocatalytic Activities of Various Anatase and Rutile Forms of Titania in Pure Liquid Organic Phases and in Aqueous Solutions," *The Journal of Physical Chemistry,* vol. 100, pp. 13655-13661, 1996.

[137] M. Sleiman, P. Conchon, C. Ferronato, and J.-M. Chovelon, "Photocatalytic oxidation of toluene at indoor air levels (ppbv): Towards a better assessment of conversion, reaction intermediates and mineralization," *Applied Catalysis B: Environmental,* vol. 86, pp. 159-165, 2009.

[138] C. Raillard, V. Héquet, P. Le Cloirec, and J. Legrand, "Kinetic study of ketones photocatalytic oxidation in gas phase using TiO2-containing paper: effect of water vapor," *Journal of Photochemistry and Photobiology A: Chemistry,* vol. 163, pp. 425-431, 2004.

[139] H. Miao, S. Ratnasingam, C. S. Pu, M. M. Desai, and C. C. Sze, "Dual fluorescence system for flow cytometric analysis of Escherichia coli transcriptional response in multi-species context," *Journal of Microbiological Methods,* vol. 76, pp. 109-119, 2009.

[140] S. Rtimi, O. Baghriche, R. Sanjines, C. Pulgarin, M. Ben-Simon, J. C. Lavanchy, A. Houas, and J. Kiwi, "Photocatalysis/catalysis by innovative TiN and TiN-Ag surfaces inactivate bacteria under visible light," *Applied Catalysis B: Environmental,* vol. 123–124, pp. 306-315, 2012.

[141] Z. P. Wang, Y. H. Lee, B. Wu, A. Horst, Y. S. Kang, Y. J. Tang, and D. R. Chen, "Anti-microbial activities of aerosolized transition metal oxide nanoparticles," *Chemosphere,* vol. 80, pp. 525-529, 2010.

[142] H. Yang, C. Liu, D. Yang, H. Zhang, and Z. Xi, "Comparative study of cytotoxicity, oxidative stress and genotoxicity induced by four typical nanomaterials: the role of particle size, shape and composition," *Journal of Applied Toxicology,* vol. 29, pp. 69-78, 2009.

[143] R. van Grieken, J. Marugán, C. Pablos, L. Furones, and A. López, "Comparison between the photocatalytic inactivation of Gram-positive *E. faecalis* and Gram-negative *E. coli* faecal contamination indicator microorganisms," *Applied Catalysis B: Environmental,* vol. 100, pp. 212-220, 2010.

[144] D. Mitoraj, A. Janczyk, M. Strus, H. Kisch, G. Stochel, P. B. Heczko, and W. Macyk, "Visible light inactivation of bacteria and fungi by modified titanium dioxide," *Photochemical & Photobiological Sciences,* vol. 6, pp. 642-648, 2007.

[145] Y. Gai, J. Li, S.-S. Li, J.-B. Xia, and S.-H. Wei, "Design of Narrow-Gap TiO_2: A Passivated Codoping Approach for Enhanced Photoelectrochemical Activity," *Physical Review Letters,* vol. 102, p. 036402, 2009.

[146] P. Zhang, C. Shao, Z. Zhang, M. Zhang, J. Mu, Z. Guo, Y. Sun, and Y. Liu, "Core/shell nanofibers of TiO_2@carbon embedded by Ag nanoparticles with enhanced visible photocatalytic activity," *Journal of Materials Chemistry,* vol. 21, pp. 17746-17753, 2011.

[147] S. Kim, S.-J. Hwang, and W. Choi, "Visible Light Active Platinum-Ion-Doped TiO_2 Photocatalyst," *The Journal of Physical Chemistry B,* vol. 109, pp. 24260-24267, 2005.

[148] M. Wu, B. Yang, Y. Lv, Z. Fu, J. Xu, T. Guo, and Y. Zhao, "Efficient one-pot synthesis of Ag nanoparticles loaded on N-doped multiphase TiO_2 hollow nanorod arrays with enhanced photocatalytic activity," *Applied Surface Science,* vol. 256, pp. 7125-7130, 2010.

[149] S. Zhang, F. Peng, H. Wang, H. Yu, S. Zhang, J. Yang, and H. Zhao, "Electrodeposition preparation of Ag loaded N-doped TiO_2 nanotube arrays with enhanced visible light photocatalytic performance," *Catalysis Communications,* vol. 12, pp. 689-693, 2011.

[150] H. Sun, R. Ullah, S. Chong, H. M. Ang, M. O. Tadé, and S. Wang, "Room-light-induced indoor air purification using an efficient Pt/N-TiO_2 photocatalyst," *Applied Catalysis B: Environmental,* vol. 108–109, pp. 127-133, 2011.

[151] S. X. Liu, Z. P. Qu, X. W. Han, and C. L. Sun, "A mechanism for enhanced photocatalytic activity of silver-loaded titanium dioxide," *Catalysis Today,* vol. 93–95, pp. 877-884, 2004.

[152] C. Y. Xu, P. X. Zhang, and L. Yan, "Blue shift of Raman peak from coated TiO_2 nanoparticles," *Journal of Raman Spectroscopy,* vol. 32, pp. 862-865, 2001.

[153] C.-H. Lin, J.-H. Chao, C.-H. Liu, J.-C. Chang, and F.-C. Wang, "Effect of Calcination Temperature on the Structure of a Pt/TiO_2 (B) Nanofiber and Its Photocatalytic Activity in Generating H_2," *Langmuir,* vol. 24, pp. 9907-9915, 2008.

[154] W. Zhao, C. Chen, W. Ma, J. Zhao, D. Wang, H. Hidaka, and N. Serpone, "Efficient Photoinduced Conversion of an Azo Dye on Hexachloroplatinate(IV)-Modified TiO_2 Surfaces under Visible Light Irradiation—A Photosensitization Pathway," *Chemistry – A European Journal,* vol. 9, pp. 3292-3299, 2003.

[155] B. Ohtani, K. Iwai, S.-i. Nishimoto, and S. Sato, "Role of Platinum Deposits on Titanium(IV) Oxide Particles: Structural and Kinetic Analyses of Photocatalytic Reaction in Aqueous Alcohol and Amino Acid Solutions," *The Journal of Physical Chemistry B,* vol. 101, pp. 3349-3359, 1997.

[156] M. Jose Ruben, E. Jose Luis, C. Alejandra, H. Katherine, B. K. Juan, R. Jose Tapia, and Y. Miguel Jose, "The bactericidal effect of silver nanoparticles," *Nanotechnology,* vol. 16, p. 2346, 2005.

[157] D. Guin, S. V. Manorama, J. N. L. Latha, and S. Singh, "Photoreduction of Silver on Bare and Colloidal TiO_2 Nanoparticles/Nanotubes: Synthesis, Characterization, and Tested for Antibacterial Outcome," *The Journal of Physical Chemistry C,* vol. 111, pp. 13393-13397, 2007.

[158] Z. Liu, Y. Su, and K. Varahramyan, "Inkjet-printed silver conductors using silver nitrate ink and their electrical contacts with conducting polymers," *Thin Solid Films,* vol. 478, pp. 275-279, 2005.

[159] Z. Zheng, B. Huang, X. Qin, X. Zhang, Y. Dai, and M.-H. Whangbo, "Facile in situ synthesis of visible-light plasmonic photocatalysts $M@TiO_2$ (M = Au, Pt, Ag) and evaluation of their photocatalytic oxidation of benzene to phenol," *Journal of Materials Chemistry,* vol. 21, pp. 9079-9087, 2011.

[160] S. Eustis and M. A. El-Sayed, "Why gold nanoparticles are more precious than pretty gold: Noble metal surface plasmon resonance and its enhancement of the radiative and nonradiative properties of nanocrystals of different shapes," *Chemical Society Reviews,* vol. 35, pp. 209-217, 2006.

[161] A. Dauscher, L. Hilaire, F. Le Normand, W. Müller, G. Maire, and A. Vasquez, "Characterization by XPS and XAS of supported Pt/TiO2 CeO2 catalysts," *Surface and Interface Analysis,* vol. 16, pp. 341-346, 1990.

[162] F. Denny, J. Scott, K. Chiang, W. Y. Teoh, and R. Amal, "Insight towards the role of platinum in the photocatalytic mineralisation of organic compounds," *Journal of Molecular Catalysis A: Chemical,* vol. 263, pp. 93-102, 2007.

[163] G. N. Kryukova, G. A. Zenkovets, A. A. Shutilov, M. Wilde, K. Günther, D. Fassler, and K. Richter, "Structural peculiarities of TiO_2 and Pt/TiO_2 catalysts for the photocatalytic oxidation of aqueous solution of Acid Orange 7 Dye upon ultraviolet light," *Applied Catalysis B: Environmental,* vol. 71, pp. 169-176, 2007.

[164] M. Huang, C. Xu, Z. Wu, Y. Huang, J. Lin, and J. Wu, "Photocatalytic discolorization of methyl orange solution by Pt modified TiO2 loaded on natural zeolite," *Dyes and Pigments,* vol. 77, pp. 327-334, 2008.

[165] M. Asiltürk, F. Sayılkan, S. Erdemoğlu, M. Akarsu, H. Sayılkan, M. Erdemoğlu, and E. Arpaç, "Characterization of the hydrothermally synthesized nano-TiO_2 crystallite and the photocatalytic degradation of Rhodamine B," *Journal of Hazardous Materials,* vol. 129, pp. 164-170, 2006.

[166] P. Qu, J. Zhao, T. Shen, and H. Hidaka, "TiO_2-assisted photodegradation of dyes: A study of two competitive primary processes in the degradation of RB in an aqueous TiO_2 colloidal solution," *Journal of Molecular Catalysis A: Chemical,* vol. 129, pp. 257-268, 1998.

[167] T. Watanabe, T. Takizawa, and K. Honda, "Photocatalysis through excitation of adsorbates. 1. Highly efficient N-deethylation of rhodamine B adsorbed to cadmium sulfide," *The Journal of Physical Chemistry,* vol. 81, pp. 1845-1851, 1977.

[168] Y.-F. Li, D. Xu, J. I. Oh, W. Shen, X. Li, and Y. Yu, "Mechanistic Study of Codoped Titania with Nonmetal and Metal Ions: A Case of C + Mo Codoped TiO_2," *ACS Catalysis,* vol. 2, pp. 391-398, 2012/03/02 2012.

[169] T. P. Yadav and O. N. Srivastava, "Synthesis of nanocrystalline cerium oxide by high energy ball milling," *Ceramics International,* vol. 38, pp. 5783-5789, 2012.

[170] H. Zhang, X. Li, and G. Chen, "Ionic liquid-facilitated synthesis and catalytic activity of highly dispersed Ag nanoclusters supported on TiO_2," *Journal of Materials Chemistry,* vol. 19, pp. 8223-8231, 2009.

[171] Zhenan Han, Victor W.C. Chang, Li Zhang, Man Siu Tse, Ooi Kiang Tan, and L. M. Hildemann, "Preparation of TiO_2-Coated Polyester Fiber Filter by Spray-Coating and Its Photocatalytic Degradation of Gaseous Formaldehyde," *Aerosol and Air Quality Research,* vol. 12, pp. 1327-1335, 2012.

Appendix A: Specifications of the Custom-Built Photocatalytic Test System for Gaseous Pollutants

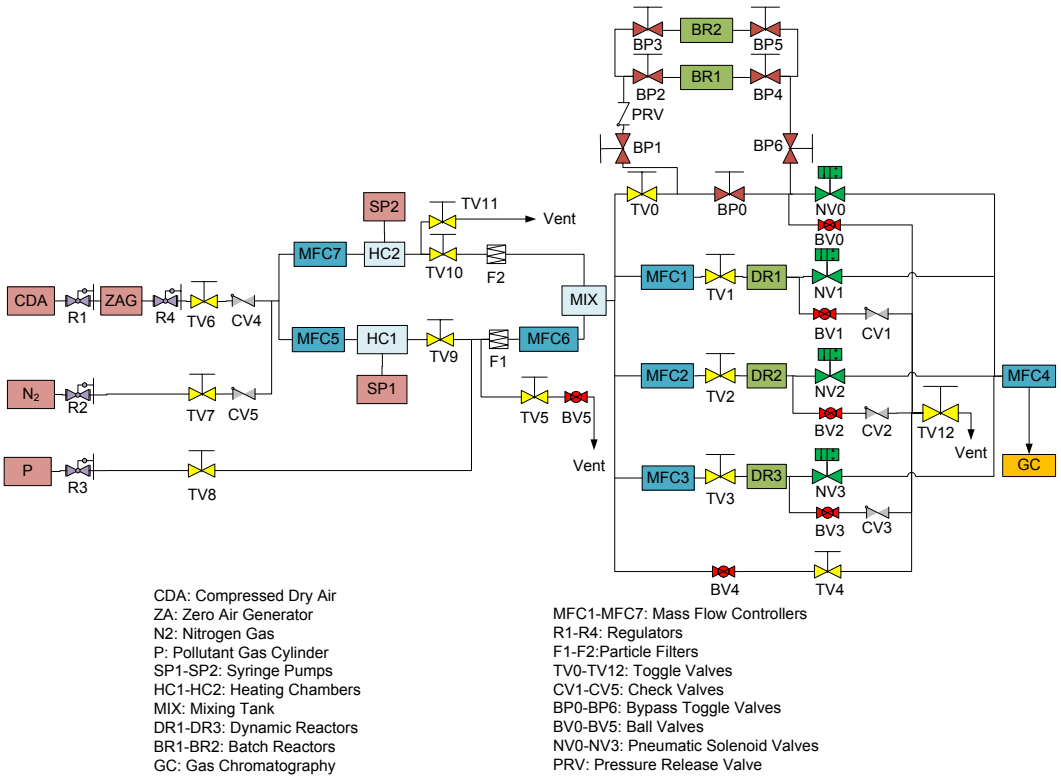

Description
Custom-built photocatalytic test system to supply pollutant gases with predetermined concentration into photoreactors (**PR1-PR3** or **BR1-BR2**) as well as gas chromatography system (**GC**)
Specifications
a) Zero air generator (ZAG, ZA300, Peak Scientific Instrument)
– Meant for producing a constant flow of Zero Grade Air to serve as both diluting and carrier gas for the gaseous pollutants – Hydrocarbon content (as Methane) of less than 0.1ppm
b) Syringe pumps (SP1-SP2, Nexus 3000, Chemyx)
– Meant for injecting the pollutant in liquid form or water into the system – Can accommodate up to 10 syringes concurrently with volume of 0.5 µl to 140 ml – Rate: 0.001 pico/min – 500 ml/min – Accuracy/Reproducibility: ± < 1%, ± 0.1% – 50 ml reusable stainless steel syringes (#780809, KD Scientific) with Swagelok 1/8 inch end fittings are used to fill the liquid
c) Heating chambers (HC1-HC2, custom-built)
– **HC1** is used to generate target pollutant in gas form (IPA, benzene, and toluene) via pollutant liquid

infusion and evaporation

- A heater was wrapped around **HC1** to vaporize the infused liquid at around 50 °C or above
- The internal dimension of the cylindrical **HC1** is around 200 mm × 50 mm × 50mm (L×R×R)
- Six 1/16 inch stainless steel tubing with VCR fittings are included as shown below for connection to syringe needles while two 1/4 inch stainless steel VCR fittings are made at the sides of **HC1** for connection to **MFC7** and **MIX**
- The distance in between the tubing for connection to syringes is ca. 28 mm and the distance from all the fitting to the bottom of **HC1** is ca. 160 mm.

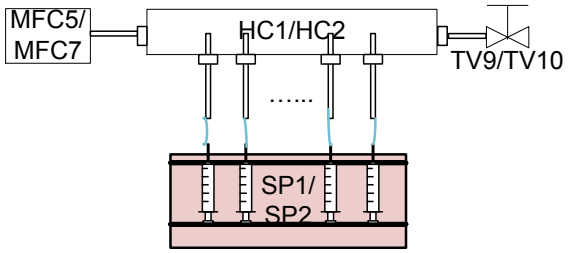

- **HC2** is used to humidify the zero air by water infusion through **SP2**
- A heater is wrapped around it to vaporize the infused water at around 50 °C
- The internal dimension of **HC2** is around 200 mm × 50 mm × 50 mm (L×R×R)
- Six 1/16 inch stainless steel tubing with VCR fittings are included for connection to syringe fittings while two 1/4 inch stainless steel VCR fittings are made at the sides of **HC2** to connect to **MFC7** and **TV10**
- The distance in between the tubing for connection to syringes is ca. 28 mm and the distance from the fitting to the bottom of **HC2** is ca.160 mm

d) Mixing tank (MIX, custom-built)

- Meant for homogenizing gaseous target pollutant with humidified zero air
- Sealed cylindrical TIG welding stainless steel chamber
- The internal diameter of the tank is 100 mm while the internal length is 500 mm
- Besides the two inlets in connection with **F2** and **MFC6** and one outlet connecting to **MFC1-MFC3**, a humidity/temperature probe (HXP86, Omega) with 3/4 inch NPT fitting is mounted for conditioning purpose

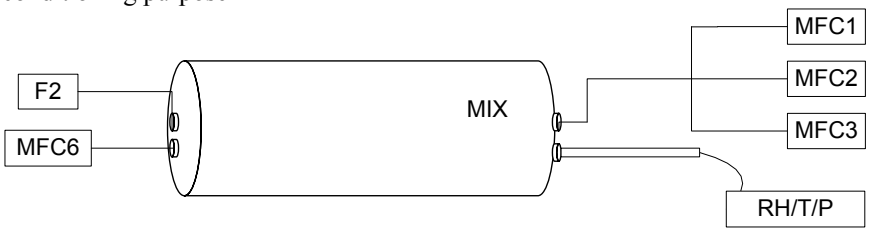

e) Dynamic reactors (DR1-DR3, custom-built) and batch reactors (BR1-BR2, custom-built)

- Meant for testing the photocatalytic performance under both dynamic and static conditions
- Refer to Section 4.1.1.2 for detailed description on the reactor design

g) Gas chromatography (GC, Clarus 600, Perkin Elmer, custom-modified)

- Meant for analyzing the concentration of gas pollutants and CO_2/CO byproducts
- GC system with built-in oven, gas purifier for carrier gas line, two six-port sampling valve and 2 mL sampling loop, one capillary column (ELITE-5 -30M-1.5µM-.53MM), two packed columns (HayeSep N 7' OD 1/8 and MS-13X 9' OD 1/8) and flame ionization detector

h) Mass flow controllers (MFC1-MFC7, CS200, Sevenstar)

- Meant for controlling the flow rates of gases inside the system
- D-type mass flow controller

– Full range: 200 sccm × 1, 2 slm × 4, 10 slm × 1, 20 slm × 1 – Accuracy: ±1% S.P. (≥35%F.S.) ±0.35% F.S. (<35%F.S.) – Repeatability: ±0.2% F.S. – Response time: ≤0.8 sec – Valve rest position: normally closed – Differential pressure: 0.1-0.35 MPa – Material: 316L stainless steel with metal seals – Fitting: 1/4" VCR – Operating temperature: 5-45 ºC
i) Toggle valves (TV0-TV12 and BP0-BP6)
– Meant for switching on and off the gas flow path inside the system or bypassing the gas flow – Manually controlled normally-close (NC) toggle valves – Valve and stem material: stainless steel
j) Check valves (CV1-CV5)
– Meant for preventing contamination from pollutant gas to the compressed dry air (**CDA**) and N_2 gas source (**N_2**) – Unidirectional flow control – Valve material: stainless steel
k) Ball valves (BV0-BV5)
– Meant for establishing positive pressure to ensure proper function of MFCs – Manually controlled normally-close (NC) bypass ball valves – Valve and ball material: stainless steel
l) Pneumatic solenoid valves (NV0-NV3)
– Meant for sequential gas sampling – Come with the ***solenoid valves*** so that the signals (24VDC) from the **GC** program can be tapped for sequential sampling of gas streams from inlet or **PR1-PR3** – Connected to **MFC4** with 1/4 inch Swagelok fitting
m) Pressure release valve (PRV)
– Meant for safety control – Normally off unless pressure inside the batch reactors exceed 30 psi – Valve material: stainless steel
n) All necessary piping and fittings
– Material for all the piping and fittings should be stainless steel – All piping must be orbital welded and the piping size is 1/4 inch unless otherwise stated – The fittings for photoreactors should be 1/4 inch VCR-NPT

Appendix B: System Flow Rates Calculation

Isopropanol (IPA), benzene, and toluene are selected as the target pollutants to evaluate the photocatalytic performance of C-TiO_2 coating on VOC removal for indoor air purification. The system design is as shown in Figure 4.2. Taking toluene as an example, the flow rate for all the MFCs (**MFC1-MFC7**) and SPs (**SP1-SP2**) can be calculated to achieve a final concentration of 200 ppm in the photoreactors.

The flow rate from **MFC1-MFC3** and **MFC4** has been set to 50-300 sccm and 100 sccm, respectively.

The desirable concentration for first stage dilution is 2000 ppm in **HC1**. If the total flow of pure toluene and zero air from **HC1** is 5 slm, the flow rate of toluene and zero air would be 4.99 slm and 10 sccm in gas form, respectively. The flow rate set by **MFC5** is thus 4.99 slm.

Assuming at 20 ºC (293K) and 1 atm, one mole of ideal gas will have the volume of 24.04 L according to ideal gas law:

$$V = \frac{nRT}{p} = \frac{1mol \times 8.314472J/(K \cdot mol) \times 293K}{101325Pa} = 0.02404m^3 = 24.04L$$

The mole flow rate of toluene in gas form should be:

$$\frac{10\ sccm}{24.04\ L/mol} = 4.16 \times 10^{-4} mol/min$$

Since the molecular weight of toluene equals to 92.14g/mol, the flow rate in terms of g/min will be:

$$4.16 \times 10^{-4}\ mol/min \times 92.14 g/mol = 0.0383\ \text{g/min}$$

The density of toluene in liquid form is 0.8669 g/ml. Thus, the infusion rate set by **SP1** should be:

$$\frac{0.0383\ g/min}{0.8669\ g/ml} = 0.0442\ ml/min = 2.65ml/hr$$

For the second stage dilution, assuming the desirable relative humidity is 50%RH at 20 °C, the water content should be 7.31 $g/kg_{(air)}$ from the relative humidity chart. The molecular weight of air in average is 29 g/mol and the molar volume is 24.04 L/mol. Thus, the water content in terms of $g/L_{(air)}$ is:

$$\frac{7.31g}{\frac{1kg_{(air)}}{29g/mol} \times 24.04L/mol} = 8.818 \times 10^{-3} g/L_{(air)}$$

Assuming a total flow of 10 slm comes out from **MIX**, the infusion rate of water set by **SP2** should be:

$$8.818 \times 10^{-3} g/L_{(air)} \times 10\ slm = 0.08818\ g/min = 5.29g/hr = 5.29ml/hr$$

To achieve a toluene final concentration of 200 ppm, the flow rate set by **MFC6** and **MFC7** should be 1 slm and 9 slm, respectively.

The flow rates for the all the MFCs and SPs can be calculated in a similar manner for IPA and benzene as specified in Table B-1.

Table B-1. Common surface modification techniques.

Pollutant	**Physical Property**		**Flow Rate**							**Final Conc.**
	MW	Density g/ml	SP1 ml/hr	SP2 ml/hr	MFC1-MFC3 slm	MFC4 sccm	MFC5 slm	MFC6 slm	MFC7 slm	ppm
IPA	60.1	0.786	1.91	5.29	50-300	100	4.99	2.5	7.5	500
Benzene	78.11	0.8765	2.22	5.29	50-300	100	4.99	0.05	9.95	10
Toluene	92.14	0.8669	2.65	5.29	50-300	100	4.99	1	9	200